A Search for TeV Emission from Active Galaxies using the Milagro Observatory

by

Elizabeth A. Hays

Dissertation submitted to the Faculty of the Graduate School of the
University of Maryland, College Park in partial fulfillment
of the requirements for the degree of
Doctor of Philosophy
2004

Advisory Committee:

Professor Gregory W. Sullivan, Chairman/Advisor
Professor Jordan A. Goodman
Professor Rabindra N. Mohapatra
Professor Sarah C. Eno
Professor Sylvain Veilleux

ABSTRACT

Title of Dissertation: A Search for TeV Emission from Active Galaxies using the Milagro Observatory

Elizabeth A. Hays, Doctor of Philosophy, 2004

Dissertation directed by: Professor Gregory W. Sullivan
Department of Physics

Milagro is a unique instrument that observes very high energy gamma rays (100 GeV to 100 TeV) using the water-Čerenkov technique. The instrument has a large field of view, which covers the entire overhead sky ($\sim$ 2 sr). Located in northern New Mexico, Milagro observes most of the Northern Hemisphere over the course of a day. The high duty cycle (>90%) permits searches for TeV sources over a variety of time exposures.

This thesis presents the results of two separate searches of the Milagro data for TeV emission. A real-time search of the entire field of view has been running since 2002. The real-time search provides early notification of significant transient behavior for time integrations from two hours to one month. No new gamma-ray sources have been found although two known sources are detected at significant levels. A longer and more refined search is conducted of archived data to monitor a set of active galaxies selected as TeV candidates. Active galaxies have been observed to be highly variable at TeV energies. To test for episodic emission, a data set is constructed using observations taken from December 2000 through September 2003 and divided into six sets of shorter time integrations. No significant emission is detected, and upper limits are set on the maximum time-averaged flux from each object for each time integration. The flux limits are also calculated to include the effects of absorption of TeV gamma rays by extragalactic background light. Predictions for the spectrum are used to set flux limits that can be compared to predictions for the flux from each source. The Milagro flux limits constrain some predictions for the TeV emission from the sources. The amount of absorption expected for two of the selected sources does not explain the discrepancy between the predictions and the flux upper limits. The implications of the constraints are discussed.

Dedicated to Ben,

whose quality of character, creativity of spirit, and depth of insight have impacted this work and continue to color my perception of everything.

ACKNOWLEDGEMENTS

I would like to thank my Milagro collaborators who have each contributed to my understanding of the experiment and astrophysics in their own unique way. It has been my great fortune to be part of such an intelligent, persistent, and supportive group of people. Milagro has been a great experience for me, and I wish you all the best in the future.

The Particle Astro group has provided a stimulating environment and I have loved being a part of it. Thanks to Greg for giving me free rein and providing a neutrino conscience to balance my gamma-ray leanings. Thanks to Jordan for making Maryland a great place to be a student and for sharing his wisdom on many topics both in and out of physics. I am in eternal debt to Andy, who taught me everything I know, and to Julie, who required me to understand it. They also deserve credit for proofreading some of the nastier chapters. I am indebted to Erik and Ty for assisting in much-needed stress-relieving espresso breaks in the face of imminent deadlines. My officemates at UMD have provided an endless source of advice, assistance, and entertainment. Thanks for putting up with me on the rough days!

Thanks to Gus for much guidance and many useful critiques. I want to thank Brenda for helpful comments and for going out of her way to help with my job search. I must also thank Scott for being an invaluable source of practical knowledge and good places to hike. To the Milagro grad students past and present, thanks for various useful discussions, handed-down knowledge, and trick pool shots.

I have to give David N. special recognition as a great sport and an excellent cook. Some may complain about life in Los Alamos, but I have good memories of hanging in LA with Dave and the UMD undergrads. Late night stargazing up at the site, BBQs at the Maryland house, driving to Santa Fe to catch all the Sunday football games, searching for

the best green chile, hiking in Bandelier that time I almost stepped on a rattlesnake - it's been fun and I'll miss you.

Special thanks to David F., Violeta, Matt, Tim, Dan, Sahra, and Chen who have been there through Quantum, the qual, and everything after.

My parents are the source of my better qualities and deserve all the credit for my interest in science and my desire to achieve. Thanks to all of my family for their support during the writing process. Drew has been especially sympathetic to the pains of completing a degree and the guilt for neglecting everything else. Eric, of course, has taken the brunt of everything and proved time and again that he is a much more patient, caring, and generally wonderful human being than I can ever hope to be.

I would also like to acknowledge those folks back in Waverly who never doubted that going off to some school nobody knew to study something nobody understood was a worthy pursuit.

The last five years have contained a full spectrum of experiences. I would like to take this opportunity to thank those who have been there with me through the good and the bad, and to recognize anyone who has read this far as undoubtedly being someone who provided a glimmer of light on some dark day. I do not know what the future may hold, but I do not have any regrets for making this stop along the way.

TABLE OF CONTENTS

LIST OF TABLES

LIST OF FIGURES

Chapter 1

The Search for Cosmic Gamma-Ray Emission

Milagro is a unique telescope for observing very high energy gamma-rays (100 GeV - 100 TeV). The instrument observes the overhead sky (~ 2 sr) throughout the day and night with a duty cycle exceeding 90%. Milagro is located in northern New Mexico and searches a significant portion of the Northern Hemisphere over a variety of time exposures. The energy range, large field of view, and high duty cycle allow searches for both steady and episodic gamma-ray emission from sources such as gamma-ray bursts, supernova remnants, and active galaxies.

Since January 2000, with the help of the Milagro collaboration, I have contributed to the construction and daily operation of Milagro in addition to data analysis. Some of the projects I have been involved with include tracking time errors in the data, developing background reduction cuts to be applied in the trigger, improving and running the timing calibration analysis, assisting with developing and maintaining a web interface to databases of detector conditions and data statistics, developing and maintaining a real-time search of incoming data for transient sources, and evaluating the sensitivity of the detector to extragalactic sources. The episodic search techniques used in the real-time transient search are applied to a set of X-ray-selected active galactic nuclei (AGN) in order to test for flaring behavior above the sensitivity of Milagro. In the absence of detections, the flux upper limits are calculated for a typical photon spectrum. Conversion factors are included to allow flux limits to be found in the case of different assumptions for the spectrum, which include redshift dependent absorption effects. The flux limits for the full duration of the data set are also calculated using two published predictions for the spectra from Costamante & Ghisellini (2002).

This thesis presents the results of a two-year real-time search for TeV emission throughout the entire Milagro field of view. No new gamma-ray sources are detected. A larger data set is also constructed for Milagro data from December 2000 through September 2003 and is divided into six shorter time scales. All seven time scales, from eight days to the full extent of the data set, are searched for emission from a set of active galaxies selected as likely TeV emitters. No significant emission is detected and upper limits are set on the maximum time-averaged flux for each time scale. The limits are also evaluated considering the effects of absorption of gamma rays by extragalactic background light. In several cases, the Milagro flux limits constrain predictions for the TeV emission from the sources. The implications of

these constraints are discussed.

To place the search results in context, the current status of gamma-ray telescopes are summarized, and the theory and observations of active galaxies are discussed. The Milagro detector configuration and data analysis techniques are described later along with a detailed description of the mechanism and method used for the timing calibration of the detector. The sensitivity of Milagro to extragalactic sources is derived in some detail to enable interpretation and discussion of the results.

The initial detection of gamma rays of cosmic origin prompted the search for gamma-ray sources and the development of particle acceleration models to explain the high energy emission observed. The continuing discovery of sources of emission by increasingly more sensitive gamma-ray detectors has driven the understanding of where and how gamma-rays are produced. Although galactic and extragalactic sources have now been discovered throughout the gamma-ray energy band ($\sim$ 100 keV - 100 TeV), many questions remain. Many of the detected sources cannot be identified with known objects in other wavebands. Meanwhile, the emission of the identified objects is not yet well understood. Some very productive studies have been conducted using simultaneous multiwavelength emission from gamma-ray sources. The resulting observations have guided the development of basic emission models. The gamma-ray observations are still reaching the sensitivities needed to distinguish between differentiate emission models. Often they have raised additional questions and not conclusively resolved fundamental questions about the sources. The number of observed sources is still small. It is not yet clear that all the existing source classes of the highest energy gamma-ray emission have been observed. This leaves a broad range of questions to be addressed by TeV observations. Some of them may best be answered using the temporal and spatial survey capabilities of gamma-ray detectors like Milagro.

1.1 A Brief History of Gamma-Ray Observations

The first observations of cosmic gamma-ray emission came from the Vela satellites. They were part of a US military program to monitor emissions from nuclear testing. The program began launching satellites in 1963, and by 1969 had instruments capable of determining directions for observed events. In 1973, a study of signals unrelated to nuclear activity was performed. At that time sixteen events were found with durations from less than 0.1 s to about 30 s in the energy range 0.2 to 1.5 MeV, the first observed gamma-ray bursts (Klebesadel et al., 1973). The directions of these events excluded the Sun and Earth as sources suggesting the bursts were cosmic in origin.

Later satellites found evidence for emission from pulsars at MeV and GeV energies. The COS-B satellite was launched in 1975 to look for gamma-ray bursts at energies from 0.1 to 1 MeV and longer duration emission from 20 MeV to 10 GeV. It was designed to observe with better angular and time resolutions than the Vela satellites. A major improvement was made by the use of the first anti-coincidence shielding to reject background events caused by charged particles passing through the

detector. This method of spurious event rejection has become standard in gamma-ray satellites. By 1981 the COS-B satellite had produced a source catalog for energies above 100 MeV that included 25 detections (Swanenburg et al., 1981). Only four of these were identified with known objects. Two objects previously observed by the SAS2 mission, the Crab and Vela pulsars, were positively identified using timing profiles. The other two objects were identified by position coincidences with the quasar 3C 273 and the ρ Orph cloud complex.

The gamma-ray source catalog expanded dramatically when the Energetic Gamma-Ray Experiment Telescope (EGRET) was flown as a part of the Compton Gamma-Ray Observatory (CGRO) from 1991-2000. The instrument was sensitive to photons with energies from 20 MeV to 30 GeV. EGRET detected a large number of galactic and extragalactic sources including pulsars, supernova remnants, active galaxies, and gamma-ray bursts. The EGRET catalog of sources with energies above 100 MeV is shown in Figure 1.1. The mission ended in 2000 with a controlled reentry into the earth's atmosphere. Several satellite missions have been launched since that time to monitor gamma-ray bursts, but nothing as comprehensive as CGRO will be available until the Gamma-Ray Large Area Space Telescope (GLAST) launches in 2007.

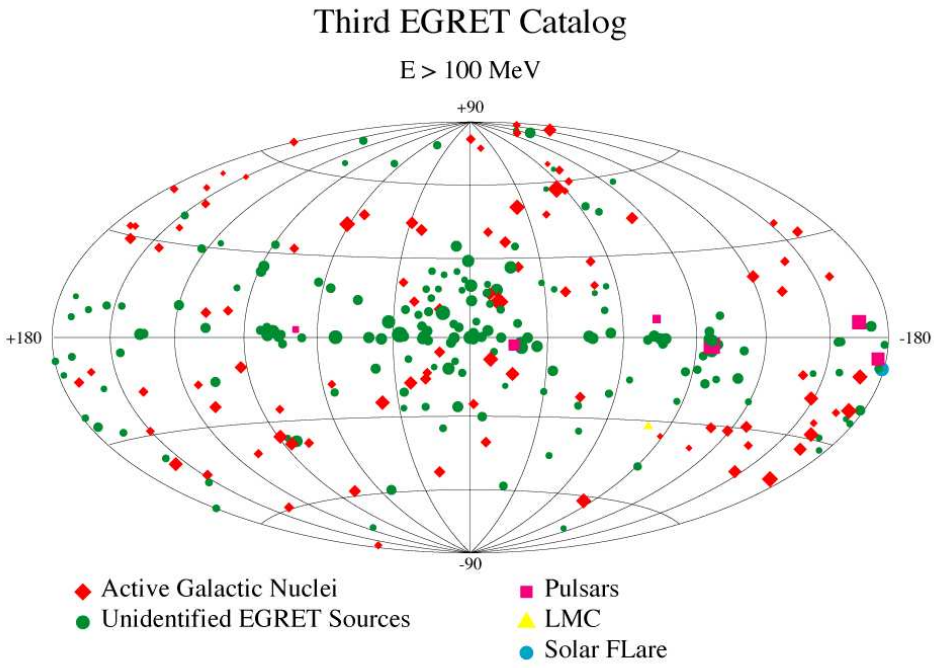

Figure 1.1: Sources of high energy emission (E>100 MeV)detected by EGRET from 1991 to 1996. Of the 271 objects 170 have not been identified with known sources in other wavebands. Figure from Hartman et al. (1999).

More than half of the EGRET detections remain unassociated with known sources in other wavebands (Hartman et al., 1999). The identification of these sources with those in other catalogs is complicated by the large angular resolution of EGRET when compared to lower frequency telescopes. The 95% confidence region for some

sources exceeds the area for a circle of 1° in radius. The uncertainty in the location creates significant source confusion with the multiple radio or X-ray sources that may be contained in the region. The EGRET catalog has a denser clustering of sources near the galactic plane that suggests that some portion of the unidentified detections are likely to be galactic objects. This distribution makes it somewhat surprising that few of the unidentified sources near the galactic plane have yet been associated with pulsars or supernova remnants.

An additional explanation for some of the EGRET unidentified sources may be the existence of additional galactic source classes at gamma-ray energies. One theoretical possibility for galactic sources primarily detected in the gamma-ray band is off-axis radio-quiet pulsars (Harding & Zhang, 2001). Another possibility could be regions with active star formation which include massive stars, strong stellar winds, and strong magnetic fields (Cesarsky & Montmerle, 1983). There is some hint of a correlation between a population of faint EGRET unidentified detections and the Gould belt, a region of our galaxy including the Sun that is slightly inclined to the galactic plane and contains many young massive stars known as OB stars. The association of a recent unidentified TeV detection Aharonian et al. (2002a) with an OB region provides some support for the potential of OB regions as gamma-ray emitters.

Another population of unidentified EGRET sources lies at high latitudes far from the galactic plane. These are likely to be associated with extragalactic objects like active galaxies. Observations at TeV energies, however, have not produced detections of any of the unidentified EGRET sources. This again could be due to large errors in the locations of the sources. Some of the error regions exceed 1° while many TeV instruments have angular resolution better than 0.5°. The possibility of additional extragalactic source classes at GeV and TeV energies which are not readily detectable in other wavebands is also being considered. There is some speculation that galaxy clusters containing shock regions from mergers or accretion could emit gamma-rays.

In 1989, TeV gamma-ray emission was first detected by a ground-based instrument, the Whipple imaging atmospheric Čerenkov telescope (IACT), from the Crab Nebula (Weekes et al., 1989). This galactic object is classified as a plerion, a type of supernova remnant which is thought to contain a pulsar that converts much of its energy into a pulsar wind. Plerions exhibit X-ray and radio emission within the expanding shell of the remnant, which itself may or may not be visible. Although EGRET observed pulsed emission from the Crab Nebula, the emission at TeV energies has not been observed to have any periodicity. This has proved convenient for comparing the sensitivity of TeV telescopes. The Crab Nebula, which is visible in the Northern and Southern hemispheres, provides an absolute standard for comparing measurements from different TeV instruments. The successful detection of TeV emission from the Crab Nebula provided long-sought proof of the atmospheric Čerenkov technique in addition to revealing a very high-energy steady-state emission component from a plerion. The observations of the Crab provided a useful source for improving the sensitivity of the technique. Unlike the satellite instruments, ground-based gamma-ray telescopes cannot be tested and calibrated using accelerators and controlled sources. The Crab Nebula provided a gamma-ray test beam that has been invaluable for understanding and improving instrument response and data analysis

methods.

The first extragalactic object detected at TeV energies, the AGN Markarian (Mrk) 421 (Punch et al., 1992), exhibited strong long and short term flaring. It was first detected in 1992 and has flared multiple times over the last few years reaching extremely intense luminosity levels. It opened up the potential of extragalactic objects as TeV emitters. The flaring behavior of AGN at TeV energies is quite different from the steady emission of the Crab Nebula. During one night of observation, the Whipple telescope observed the flux from Mrk 421 double in 15 minutes (Figure 1.2) (Gaidos et al., 1996). This was a ground breaking measurement because of the limit it sets on the size of the gamma-ray emission region. The timescale of variability is proportional to the radius of the emission region, $t_{var} \propto R/\delta c$. Variability on 15-20 minute timescales implies that the flaring emission comes from a very small region of the jet close to the central black hole that is believed to power the AGN.

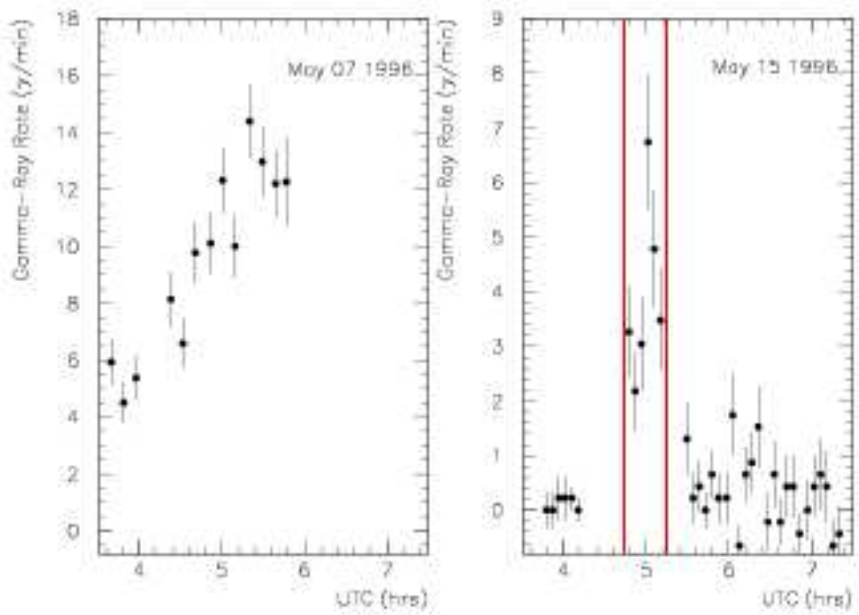

Figure 1.2: MRK 421 flares observed by the Whipple Collaboration on 7 May and 15 May 1996. The first observation is the highest flux observed from any TeV source and has a flux doubling time of about an hour. The second has a lower gamma-ray rate, but is the most rapid variability observed from an AGN, with a flux doubling time of about 15 minutes. Figure from Gaidos et al. (1996).

A second AGN was detected in 1996 with the Whipple telescope (Quinn et al., 1996). For the first time an extragalactic gamma-ray source was discovered by a ground-based instrument. After the TeV detection, Mrk 501 was also detected in EGRET data, but as only a weak GeV source. Despite the strong flaring behavior observed in IACTS, MRK 501 was barely detectable in the waveband of the satellite observations. Following several months of strong flaring, Mrk 501 returned to a quiescent state and has remained quiet in the gamma-ray waveband since that time.

1.2 Sources of Gamma-Ray Emission

The current catalog of high energy gamma-ray sources is split into two categories by the energy at which they were detected. This gap in energy is a result of the two broad classes of gamma-ray detectors, space-based and ground-based, which are sensitive to different regions of the gamma-ray waveband. The energy ranges available to the two types of detectors do not currently overlap leaving a divide between the high energy (20 MeV - 30 GeV) detections made by space-based detectors and the very high energy (300 GeV - 50 TeV) detections made by ground-based detectors.

The catalogs of sources in the two energy regimes differ in more than energy. The development of ground-based detectors has lagged behind that of the space-based detectors. The catalog of sources from space-based observations now contains a few hundred objects. The ground-based catalog is quite small in comparison, with some dozen sources. Of those sources, only a portion have been detected by multiple telescopes. Expansion of the TeV catalog is necessary to understand the unifying characteristics of source classes that can be translated into a cohesive picture of the underlying physical processes. A more detailed understanding of TeV sources will allow the study of the formation and characteristics of gamma-ray emitting regions as well as the fundamental acceleration processes and interactions of particles at energies beyond those available in accelerators on the earth.

Although the precise combination of physical interactions and conditions that produce the gamma-rays observed from individual sources causes debate, at the most fundamental level there are not very many ways to generate cosmic gamma-rays. Most methods require the acceleration of charged particles to extremely high energies. This phenomenon is most commonly explained using shock fronts that cause charged particles to undergo first order Fermi acceleration. There are then two major pathways for gamma-ray emission through leptonic or hadronic interactions. Electrons accelerated to 10^{19} eV can scatter from infrared (IR) photons through the inverse-Compton process causing the photons to attain gamma-ray energies. Protons at similar energies can generate gamma-rays through the by-products of interactions with other protons and IR photons. The hadronic interactions also produce secondary electrons that contribute additional components to the emission.

The connection between gamma rays and cosmic-ray nuclei has been one of the most tantalizing aspects of high energy astrophysics. Many attempts have been made to prove that protons are the generators of observed gamma-ray emission in galactic and extragalactic sources. The association would solve a long standing problem, the origin of highly accelerated cosmic-rays, by providing direct observations of the acceleration sites. Conclusive observational evidence for the direct connection between the sources of gamma rays and the sources of cosmic rays has yet to be found. Multiwavelength observations and the coming generation of more sensitive detectors will eventually resolve this question.

1.3 Gamma-Ray Detection

The two broad categories of gamma-ray detectors, space-based and ground-based, use very different methods to detect a gamma-ray signal.

1.3.1 Space-based Detectors

Space-based detectors, which are carried by satellites or high altitude balloons, detect gamma rays directly when they pass through the detector and and interact with the detector material. The resulting electron-positron pairs are used to determine energy and direction of the original photon. The satellite detectors typically include three main components: a tracking chamber, a calorimeter, and an anti-coincidence shield. The tracking chamber records the path of charged particles within the detector. The tracks are used to identify pairs and reconstruct the initial photon direction. The calorimeter measures the energy deposited in the detector to determine the initial photon energy. The anti-coincidence shielding typically consists of scintillator that is used to veto events caused by charged particles passing through the detector.

The backgrounds for direct detection of gamma rays are very low, making these detectors very sensitive to sources. The sensitivity to point sources is limited by gamma-ray backgrounds existing in and between galaxies. The energy range may extend from MeV to $\sim$10 GeV and is chiefly limited by the small size of the instruments and the low number of gamma rays at higher energies. The weight and size of space-based instruments cannot exceed the payload capacity of the launching vehicles. Only gamma rays actually passing through the active area of the instrument can be detected. The flux from gamma-ray sources, however, decreases as a power law with increasing energy. The area of previous detectors, at less than 1 m^2, severely limits sensitivity at energies above a few GeV. Although satellite detectors have detected gamma rays above a few GeV, the number detected is very low.

Space-based detectors have an advantage over ground-based detectors in exposure. They can be placed in orbits that allow year-long observation of sources. The high duty cycle monitoring available to satellite instruments not only prevents missed activity in transient sources but also eases coordination with simultaneous observations in other wavebands. The biggest limitation of satellite detectors has been the angular resolution. Although capable of monitoring a large portion of the sky, the location errors have been on the order of a degree. Most of the ground-based gamma-ray detectors and telescopes in other wavebands resolve sources on smaller scales, which makes it difficult to correlate observations.

1.3.2 Ground-based Detectors

The Earth's atmosphere is opaque to gamma rays. This can, however, be turned to an advantage for their detection. Instruments on the ground use the by-products of the photon interaction in the atmosphere to determine a direction and energy for the initial gamma ray. A gamma ray produces an electron-positron pair in the atmosphere at an altitude of approximately 25 km. The electron and positron then

produce additional photons through bremsstrahlung. The electromagnetic cascade continues until the photon energy drops below the threshold for pair production at 1 MeV. The resulting extensive air shower (EAS) reaches its broadest lateral extent, known as shower maximum, at an altitude of approximately 8 km. As the shower front continues through the atmosphere, the energy dissipates until the diameter is about 100 m for a shower generated by a TeV gamma ray at an altitude of 3 km. The altitude of shower maximum and the shower size at ground level depend on the energy of the initial photon and the altitude of the first interaction. The further below the altitude of shower maximum that the shower front is viewed, the less particles remain to be detected. Only detectors at high altitudes can detect enough particles to study gamma rays below 10 TeV.

Although the flux of gamma rays above a few GeV is quite small, the ground area covered by an EAS increases with photon energy. At energies for which few photons are available to be detected within a satellite instrument, ground-based detectors can view large, easily detected showers of particles. On the ground it is reasonable to build instruments capable of sampling the entire shower. The effective detecting area can be >10,000 m^2. For ground-based detectors the difficulty comes instead in background rejection. The isotropic cosmic-ray background generates EASs at a much higher rate than photons from gamma-ray sources. The ratio is roughly 1000 to 1. The development of effective background rejection techniques is the key to increasing the sensitivity of ground-based detectors.

1.3.3 Air Čerenkov Telescopes

The electrons and positrons in an air shower travel very near the speed of light and generate a cone of Čerenkov light along the line of the air shower. Imaging atmospheric Čerenkov telescopes (IACTs) focus the Cerenkov light using a large spherical reflector (existing detectors use reflectors on the order of 10 m in radius) onto a camera of photomultiplier tubes (PMTs). The Čerenkov light is very faint compared to moonlight or even bright stars within the field-of-view. Observations can only be made on clear, moonless nights because of the difficulty of detecting the Čerenkov light over any significant visible light background. This limits the duty cycle of these detectors to ∼10% and restricts them to viewing sources for the part of the year that they are above the horizon at night.

The current generation of IACTs can detect the Crab Nebula in around an hour. The sensitivity of the technique depends largely on the ability to reject background Čerenkov light from cosmic-rays and muons. An effective background rejection for cosmic-ray-induced showers has been developed for this technique based on the image characteristics of the Čerenkov light cone. The background showers are generated uniformly at the top of the Earth's atmosphere and, therefore, increase with the size of the area examined. Decreasing the angular resolution provides an additional method of reducing background events by reducing the area that must be examined for a signal. The imaging technique can achieve high angular resolution ($< 0.2^\circ$), especially when individual telescopes are combined into arrays. The detection of the same Čerenkov cone in three or more telescopes strongly constrains the axis of the

shower. Both single telescopes, such as the Whipple 10 m gamma-ray telescope, and array configurations, such as the High Energy Gamma-Ray Astronomy experiment (HEGRA), have successfully detected gamma-ray sources. The Crab Nebula for example, has been detected by several instruments with good agreement in absolute flux.

Good point source sensitivity has made IACTs highly successful at observing the flux variation and energy spectra of known TeV sources. Data from simultaneous multiwavelength campaigns with X-ray and optical instruments have provided information about the spectrum that probes the underlying emission models for some of these VHE sources. However, this is a narrow field-of-view technique, and only a few degrees of sky can be observed at one time. The high angular resolution and sensitivity make it inefficient to use IACTs as survey instruments or for viewing sources that are diffuse or have a large angular extent.

1.3.4 Extensive Air Shower Arrays

The study of air showers generated by cosmic-rays forms a separate field of study. The technology has been applied in some cases to detect gamma-ray showers. EAS arrays have typically consisted of numerous scintillator detectors spread out over a large area (>1 km^2). Several EAS arrays are described in Alexandreas et al. (1992) and Borione et al. (1994). The individual detectors that make up the array measure the arrival times of charged particles across the shower front. The times are then used to reconstruct the air shower direction. The individual scintillators measure the energy deposited by charged particles in the shower. This information determines the size of the air shower and can be related to the initiating particle energy. Some separation of gamma-ray-induced and proton-induced air showers is achieved with this technique by finding the presence of muons, a hadronic by-product.

Although the image characteristics of EAS shower fronts include exploitable differences between gamma-ray and cosmic-ray induced air showers, effective background rejections in EAS arrays were not found. The gamma-ray-induced air showers detectable with scintillator detectors have exceedingly high energies (>50 TeV) due to being located at low altitudes and sampling only the charged particle component of the air shower. The low flux of gamma-rays at this energy are not detectable above the large flux of cosmic-ray-induced air showers. Only upper limits for gamma-ray sources exist using EAS arrays.

1.3.5 Water Čerenkov Array

Ideally, a good survey instrument has a wide field-of-view and a high duty cycle for long-term monitoring of a large portion of the sky. EAS arrays meet these criteria, but lack sensitivity to gamma-ray sources. Using the water-Čerenkov technique, the EAS array concept is modified to lower the energy threshold to levels comparable to that of IACTs and allow the detection of gamma-ray sources. This is accomplished in three ways:

- Placing the detector at high altitude closer to shower maximum.

- Using water as an efficient detection medium detect.
- Employing a large external array to constrain the size and location of the shower.

A high altitude detector has much more opportunity to detect the EAS closer to its maximum development, where the particle content is higher. The concept for the water-Čerenkov technique came from the desire to keep the large field-of-view and high duty cycle of EAS arrays and the realization that the energy threshold could be lowered by using water as the detection medium. The EAS shower front travels very near to the speed of light. When the high velocity charged particles in the shower front enter water, they emit Čerenkov radiation. Not only does water allow efficient detection of the charged particles, but it also converts the photon component of the air shower into charged particles. The photons in the air shower produce electron-positron pairs in water that are then detected in the same manner as the charged component of the air shower. This also allows the shower front to be fully sampled over the area of the array and not only at the positions of individual detectors. Instruments using the water-Čerenkov technique are effective at detecting the smaller, lower energy EASs that fail to trigger large cosmic-ray arrays.

The distribution of energy in the array can be used as an indication of the location of the center, or core, of the shower front. Because the shape of the shower front has a dependence on distance from the shower core, the location of the core is a key parameter used in reconstruction of the shower direction. Knowledge of the size of the shower helps better locate the core position. The addition of a surrounding low density array measures the extent of the air shower and removes confusion between small showers and large showers with cores far from the inner array. The distribution of energy detected by an additional deep array allows imaging of the higher energy, penetrating particles expected in cosmic-ray induced showers. An application of cosmic-ray background rejection in Milagro is described in Chapter 5.

The Milagro water-Čerenkov detector has been observing the Northern Hemisphere since January 2000. It has been used to successfully detect gamma rays from the Crab Nebula (Atkins et al., 2003) and the AGN Mrk 421 during flaring activity. The wide field of view available to Milagro allows sensitive observations of sources with a large angular extent. Milagro has detected extended gamma-ray emission from the Cygnus arm region of the galactic plane and from the vicinity of 3EG 0520+2556 ,an unidentified EGRET source. Milagro observations for the entire available field of view over three years of data provide the most sensitive survey available of the Northern Hemisphere at TeV energies and show no other significant gamma-ray sources in the Northern Hemisphere (Atkins et al., 2004b).

Milagro can make observations of the Sun and the Moon by finding a significant deficit, or shadow, in the cosmic-ray background. The shadow of the Moon is detected and shows the displacement due to deflection of charged particles in the Earth's magnetic field. Detections of the shadow and non-detections of an oppositely deflected shadow provide a unique measurement of the anti-proton content of the cosmic-rays Observations of the Sun reveal a shadow that varies over time with changes in the Sun's magnetic field. The observations have been used to set limits on

the annihilation of WIMPs in the Sun. Milagro also observes changes in the cosmic-ray rate due to solar flares. Coincidence with detections of solar events in neutron monitors was observed on 6 November 1997 with Milagrito, and more recently with Milagro, a particularly notable change in the rate was observed in coincidence with a detection by neutron monitors on 28 October 2003.

1.4 Current Status of TeV Observations

Currently eight TeV sources are confirmed, meaning they have been detected at high significance by more than one instrument (Horan & Weekes, 2004). Two are pulsar nebulae within the galaxy and the remaining confirmed sources are all nearby AGN (z<0.129). There are additionally unconfirmed detections from single instrument observations which include several supernova remnants, several AGN (possibly at z=0.444), a starburst galaxy, a radio galaxy and an unidentified source near an EGRET detection in the vicinity of Cygnus OB2. The types of sources included in this list provide an unexpected variety of avenues to investigate the extremes of shock acceleration as well as the propagation of high energy photons through extragalactic space.

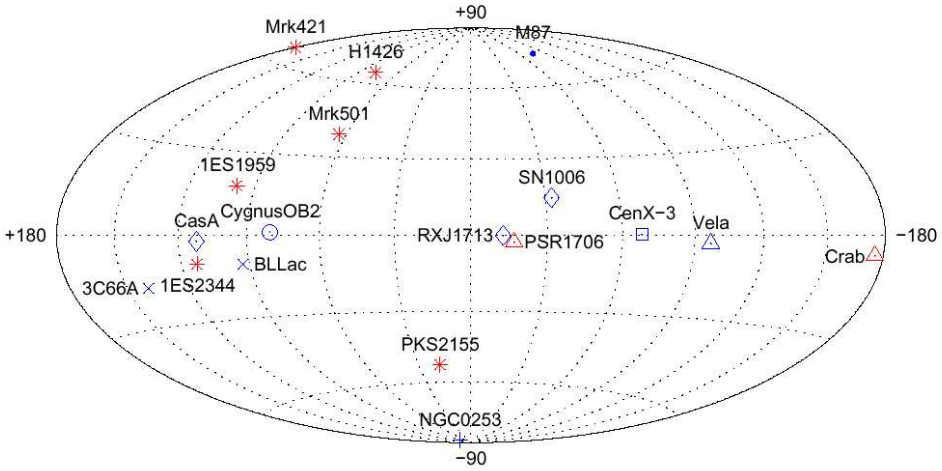

Figure 1.3: TeV catalog of confirmed (red) and unconfirmed (blue) galactic and extragalactic sources of TeV emission. Figure from Horan & Weekes (2004).

The first unidentified TeV object, TeV 2032+4131, was discovered serendipitously by the HEGRA experiment in the same field as another observation (Aharonian et al., 2002a). The HEGRA observation suggests that this source is not point-like, ruling out an AGN or pulsar identification. The TeV detection is located at the edge of the 95% error circle for the unidentified EGRET source, 3EG J0233+4118. Observations at GeV energies with better angular resolution are required to confirm the association. The detection is also associated with a young massive star region in the galaxy, Cygnus OB2. Some theories suggest that under appropriate conditions the emission at lower energies may not be observed due to low energy escape cutoffs due to strong

magnetic fields. This possibility opens up a potential class of diffuse sources that might only be detected by gamma-ray telescopes. The continued expansion of the TeV catalog will provide more observations in each source class to constrain models and develop the physics of the source types.

The appropriate search strategy for finding additional TeV sources using currently available detectors is not apparent. Initially the EGRET sources were considered promising TeV candidates, but none have been detected in targeted search campaigns by IACTs. Now that more AGN have been detected in the TeV band a reciprocal trend of weak detections or non-detections by EGRET has been established. The cause of the apparent divide between GeV and TeV detections of AGN is not yet clear. It can be explained by the characteristics of certain emission models, but in the absence of a strong understanding of what defines a TeV source, further observations are necessary.

The current TeV catalog may provide the best guidance for finding additional TeV sources until broader surveys are available. Extragalactic TeV candidate predictions have had some success. One class of source, BL Lacs, has produced multiple TeV detections. Searches of BL Lac objects with bright emission in the X-ray band have led to the discoveries. Although X-ray-selected BL Lacs are favored for extragalactic emission, it is still unknown when or how often to observe candidate BL Lac objects. There have not been enough detections to develop predictions for the frequency or duration at which flares from a specific source might occur.

The next generation of IACTs has already begun to gather data. Many are array systems that increase sensitivity by reducing background using multiple images of the same shower. The High Energy Stereoscopic System (HESS) has completed an array of four air-Čerenkov telescopes in Namibia that started operation in December 2003. CANGAROO III in Australia has completed four 10 m telescopes that are beginning operation in early 2004. MAGIC (Major Atmospheric Gamma-ray Imaging Čerenkov telescope) in La Palma, Spain is a large single 17 m air-Čerenkov telescope that relies on new technology to allow observations in moonlight. It began data taking in November 2003. VERITAS is beginning construction on an array of four 12 m telescopes in Arizona. One will be completed in the fall of 2004 while the other three are scheduled to be completed late in 2006. The sensitivity and global coverage provided by these facilities will allow unprecedented studies of TeV gamma-ray sources.

As the pointed instruments increase in sensitivity, however, instruments with large fields-of-view become increasingly important for monitoring transient activity. The small number of TeV detections and the unpredictable transient nature of the detected extragalactic TeV sources, make searches with narrow field-of-view instruments a less than optimal application of the high source sensitivity. Wide field-of view instruments offer an alternative approach to traditional TeV searches. The large amount of sky available to ground-based detectors like Milagro and the upcoming satellite mission GLAST removes the necessity of focusing searches on specific source classes. The unbiased information from broad surveys can best locate new classes of gamma-ray sources and most optimally monitor transients.

Chapter 2

Searching for TeV Emission from Active Galaxies

Many of the detected sources of high energy emission are active galactic nuclei (AGN). EGRET observed over 100 AGN and 6 of the 10 strongly confirmed detections at TeV energies are AGN. Observations of AGN in the gamma-ray waveband probe physics at extreme energies. They offer a view into interactions of particles accelerated well above the energies available to particle accelerators. Some progress has been made in determining the nature of the central emission engine of AGN using observations in radio and X-ray wavebands. It is the GeV and TeV observations, however, that are most critical for differentiation between models and for obtaining a full description of the acceleration mechanisms and physical characteristics of the emitting region. The rapid variability of AGN emission requires well-matched simultaneous observations in order to understand the properties of the source and to develop a fully self-consistent model of the environment and particle processes. Since the first extragalactic detection at TeV energies, there has been an effort to determine which AGN are most likely to produce TeV emission and to monitor those objects closely. Several samples of AGN likely to be TeV emitters have been compiled based on observations made in other wavelength bands. The sample described here is of particular interest because of accompanying predictions for TeV fluxes. The variable properties of these objects make them consistently interesting targets for observations in TeV telescopes.

2.1 Active Galaxies

Approximately 3% of the galaxies in the universe are classified as active. This classification distinguishes galaxies with non-stellar emission, which is often, though not exclusively, in the optical waveband. In cases where the host galaxy is visible the emission is associated with the center, or nucleus, of the galaxy. The most remarkable feature of AGN is the expanse of the electromagnetic spectrum covered by their emission. AGN have energy spectra extending from the radio to gamma-ray wavebands.

Galaxies with these characteristics are divided into subclasses in several ways depending on the relative prominence of emission in certain wavebands and various spectral features. The largest distinction is made in the radio waveband. The original radio telescopes only detected AGN with strong radio emission, known as

radio-loud AGN. Later more sensitive telescopes revealed that other AGN do emit in the radio waveband though at lesser luminosities. The majority of AGN are classified as radio-quiet. Other categories depend on the width and presence of emission lines in the spectrum. BL Lacs, for example, completely lack emission line features contrasting with Seyfert galaxies which exhibit thermal emission with strong emission line features that can be further be classified as narrow or broad.

The central emission engine, however, is thought to be the same for all AGN. Differences in the observed properties are attributed to the effects of viewing the galaxies at different angles with respect to the axis of rotation. Urry & Padovani (1995) reviewed the unified model of a radio-loud AGN, shown in Figure 2.1, which centers on a super-massive black hole, 10^6-10^9 solar masses, with a surrounding accretion disk and extended relativistic particle jets aligned along the spin axis. A dusty molecular cloud torus and various cloud structures may be present around the central black hole. The cloud structures produce spectral lines and thermal emission. The surrounding material provides a source of the strong emission lines observed in some galaxies and a method for obscuring observations of emission lines depending on the observer's line of sight.

2.2 Blazars

Blazars are a subclass of radio-loud AGN with highly-variable, highly-polarized, non-thermal continuum emission from radio to gamma-ray wavebands. The non-thermal emission from the nucleus mostly or completely dominates the thermal emission from the rest of the galaxy. The observed spectrum can be explained by an active galaxy oriented such that the relativistic jet is pointed nearly directly at the observer. These are compact sources with an optical depth for gamma rays expected to be high due to pair production with lower energy photons. The observation of gamma-rays from these sources implies that the emission region must be moving at relativistic speeds to reduce the apparent density of photons enough for gamma rays to escape (Ghisellini et al., 1993). Radio observations of superluminal motion, where the apparent velocity of the source exceeds the speed of light, provide additional support for the existence of large Lorentz factors in AGN jets. The strongly-beamed high-energy emission from the jet can only be viewed at observation angles closely aligned with the galaxy spin axis. The relative relationship between the observed numbers of AGN and blazars is consistent with the number of galaxies likely to have their jets oriented within a few degrees of the line of sight from the Earth.

BL Lacertae galaxies (BL Lacs) are a subclass of blazars with weak or absent emission lines. The spectral energy distribution (SED) for these objects extends from radio to gamma-ray frequencies with two broad components, the first peaking in radio to X-ray wavebands and the second peaking in the gamma-ray waveband ($> 10^{19}$ Hz, or > 100 keV) as shown in Figure 2.2. BL Lac objects are often additionally sub-classified by the low-frequency component of the SED (Padovani & Giommi, 1995). A high-peaked BL Lac (HBL) exhibits the strongest emission in the X-ray band while a low-peaked BL Lac (LBL) exhibits strong emission at radio

wavelengths. The BL Lacs found in radio surveys appear systematically different from those found in X-ray surveys. HBLs are also commonly called X-ray-selected BL Lacs and LBLs, radio-selected. More recent surveys, however, suggest that this is a selection effect and that an intermediate population of BL Lacs exists with the lower component peaking between the radio and X-ray bands (Laurent-Muehleisen et al., 1999).

The high degree of polarization observed in optical emission from BL Lacs indicates that the first component is caused by synchrotron emission (Jannuzi et al., 1994). The second, higher frequency component is often interpreted as inverse-Compton scattering of relativistic electrons in the jet with the synchrotron photons they have emitted, implying that HBLs with the highest frequency synchrotron peaks are the most likely to produce very high energy (VHE) gamma-ray emission (E>100 GeV). For this reason HBLs have been favored for extragalactic TeV search campaigns. The BL Lacs 1ES 1959+650 (Holder et al., 2003) and 1H 1426+428 (Horan et al., 2002) were both observed and eventually detected at TeV energies as part of search campaigns specifically targeting HBLs.

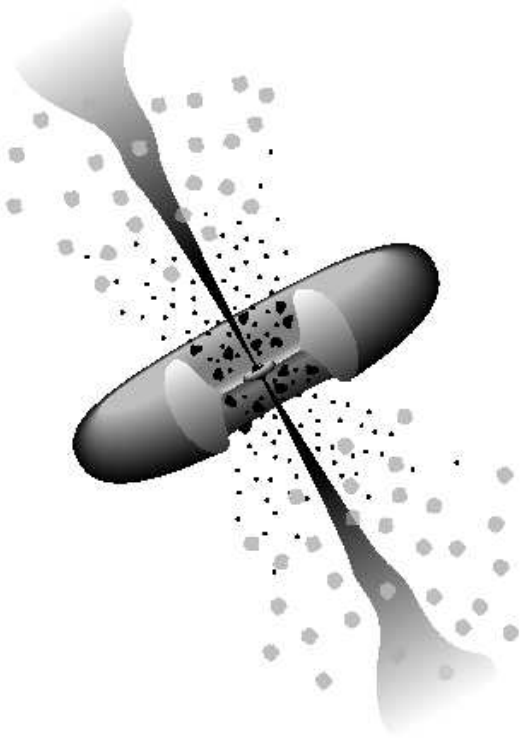

Figure 2.1: Cartoon model of an AGN. A central super-massive black hole is surrounded by an accretion disk. The region may be surrounded by clouds which exhibit broad-line emission closer to the center and narrow-line emission further away. A dusty torus may also surround the center, obscuring broad-line emission from some lines of sight. Radio, X-ray, and gamma-ray emission may be viewed from extended particle jets depending on the observation angle. Figure from Urry & Padovani (1995).

It is not yet clear what the fundamental cause of differences in the SEDs of HBLs and LBLs may be. While LBLs have more luminosity in the IC peak than the synchrotron peak, HBLs show comparable emission in both. This suggests an energy dependence in the efficiency of the emission mechanism. This could be explained if there are less photons available for IC scattering or less accelerating particles at higher energies. Emission models that assume leptons to be the primary photon emitters, explain the difference with radiative cooling of the emitting electron population and finite times for the injection of the electrons into the jet (Costamante & Ghisellini, 2002). Further observations of high and very high energy emission, which is most affected by cooling and external photon populations, in combination with lower energy observations of the seed photon populations will help to explain the differences.

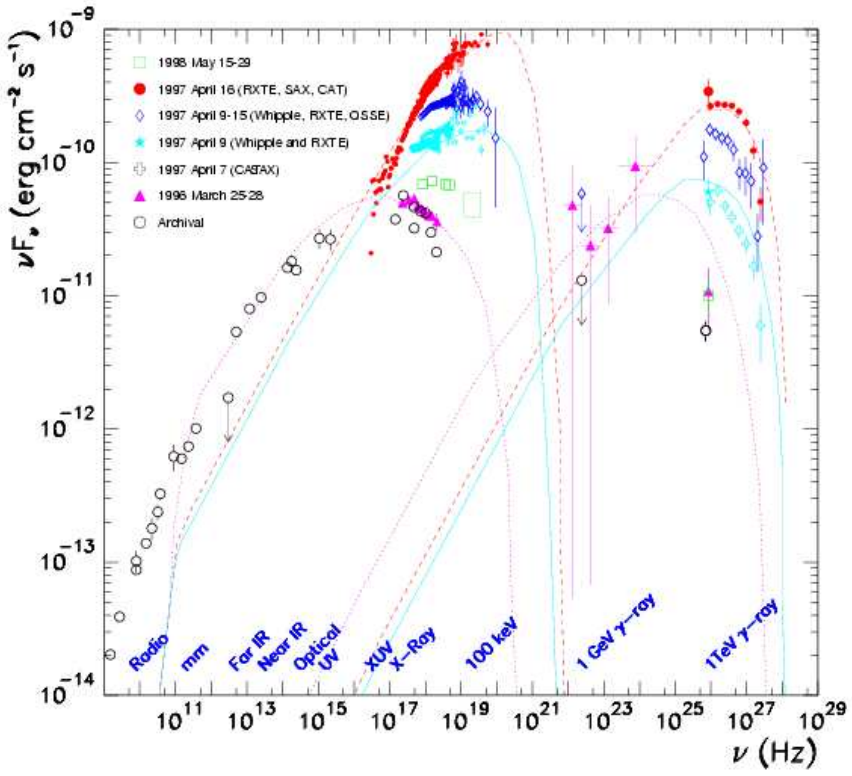

Figure 2.2: Spectral energy distribution data points for the blazar, MRK 501, from radio to gamma-ray frequencies. The points are from observations by a variety of instruments. The solid line is drawn to highlight the two emission components and does not represent an emission model. Observations at X-ray and TeV frequencies during strong flaring activity in 1997 measure a higher flux level and shifted locations of the peak frequencies. Figure from Buckley (2001).

2.2.1 The Blazar Sequence

A classification scheme developed in Fossati et al. (1998) attempts to find predictive power in the relationship between peak luminosity and peak frequency in blazar SEDs. The average SED for blazars is derived from observations broken into groups with similar 5 GHz radio luminosities (Figure 2.3). The resulting progression appears to form a continuous blazar spectral sequence as opposed to discrete classes of blazars. The bands of synchrotron power approximately match the different blazar classes. The SEDs with the two lowest radio luminosities and the highest frequency synchrotron peaks correspond to LBLs and HBLs respectively. The SEDS with higher radio luminosities correspond to Flat Spectrum Radio Quasars (FSRQs), which have not been detected in TeV instruments. The observations indicate a decrease in synchrotron power as the synchrotron peak moves to higher frequencies and a decreased ratio of the power in the IC peak to that in the synchrotron peak.Fossati et al. (1998) find a constant ratio of the frequencies of the synchrotron and IC peaks. They also find a ratio for the IC peak luminosity and the 5 GHz radio luminosity. By assuming a parabolic forms for both spectral components, the SED for a blazar can be predicted from these relationships using only the 5 GHz radio luminosity.

BL Lacs are not the most commonly observed AGN. Other galaxies are brighter in the radio band. Catalogs of BL Lacs tend to be small and the observations at multiple frequencies are limited. It is particularly useful for TeV search campaigns to be able to say something about the VHE emission of this category of blazar using only radio observations. This sequence does not represent a physical model, but does allow an estimate of which BL Lacs may be most likely to emit VHE photons.

2.3 Spectral Models

The two-peaked spectrum observed from blazars can be explained in several ways. The lower energy peak in the SED is attributed to synchrotron radiation due to observations of high polarization. The origin of the upper peak may be attributed to leptonic models that accelerate optical-IR wavelength photons through the inverse-Compton (IC) mechanism or to hadronic models that produce pions in proton-proton interactions that then decay to high energy photons. The current observations do not conclusively select either method for producing the high energy emission, although leptonic methods are favored.

Hadronic models predict that protons dominate the interactions in the jet that produce VHE gamma-rays. This could occur in two ways: by proton-induced cascades (Mannheim, 1993) or directly by the accelerated protons (Aharonian, 2000; Mücke & Protheroe, 2001). The proton-induced cascade model attributes the high energy component of the blazar SED to photo-pair production ($\gamma p \rightarrow e^+e^-$) and photo-pion production ($\gamma p \rightarrow \pi^0 p$). The neutral pions primarily decay to a pair of secondary photons. The secondary electrons contribute at a lesser level through bremsstrahlung and IC scattering of synchrotron photons. The size of the emission region indicated by short flares ($<$ 1 hr implies $< 10^{16}$ cm) requires proton energies, E$\geq 10^{19}$ eV, to reach good efficiency which in turn implies extremely high magnetic

fields, B$\gg$ 1 Gauss. The observed TeV fluxes require extremely high luminosities of the highest energy protons in the jet. The direct acceleration by protons instead focuses on the higher efficiency of proton-synchrotron radiation for producing high energy gamma rays for this level of proton energy and magnetic field. This type of model can explain the relatively small changes in spectral shape observed in Mrk 501 during strong flaring activity.

A variety of leptonic models have been developed. All attribute the primary acceleration to relativistic electrons and positrons in the jet. Differences exist in the source of target photons scattered through the IC mechanism to high energies (Dermer et al., 1992; Sikora et al., 1994), the number of emission regions (Tavecchio et al., 1998), and the uniformity of the physical parameters along the jet (Ghisellini & Madau, 1996). The source of the seed photons for IC scattering may be only the synchrotron photons produced in the jet, or additional photons from the accretion disk, scattered from surrounding dust clouds, scattered from the intergalactic background, or a combination of these. The electron and photon densities and spectra, magnetic field, Lorentz factor, and the size of the emission region or regions can be adjusted to match existing multiwavelength data. Time variations in some of these parameters can be introduced to explain more complicated flaring behavior. Models

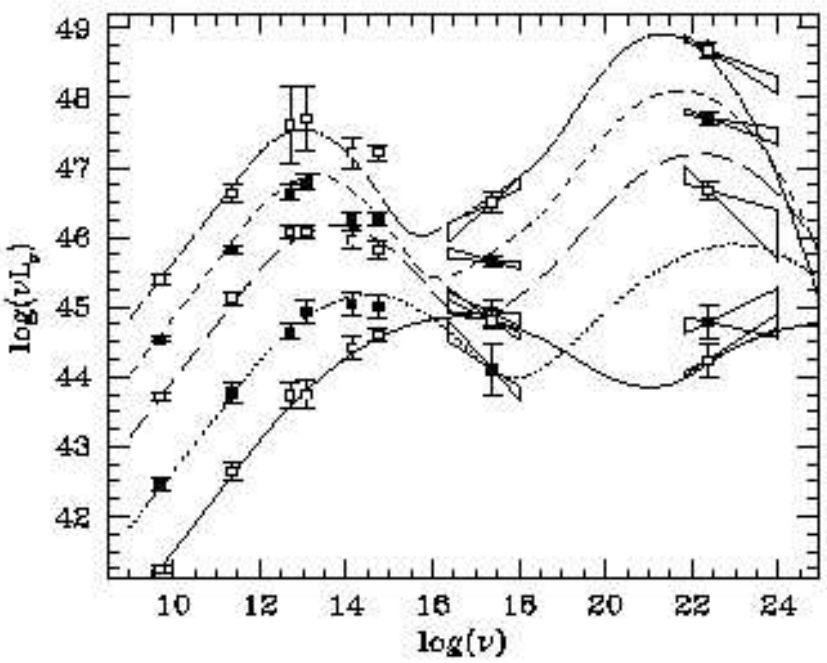

Figure 2.3: The average SED for blazars divided into five bands determined by 5 GHz radio luminosity. The SEDs with the lowest power in the synchrotron peak, produce the highest frequency and lowest power IC peaks. The two lowest radio luminosity SEDs correspond to LBLs and HBLs. The HBL SED has the only appreciable IC luminosity at the highest energies. Figure from Fossati, Maraschi, Celotti, Comastri, & Ghisellini (1998).

using electrons as the primary particles are generally favored because they more naturally explain some of the temporal behavior and relationships between the fluxes above the low and high energy component peaks.

The most common and the simplest leptonic model assumes that the photons IC scattered to high energies are the same emitted through the synchrotron process in the jet. These models are called synchrotron self-Compton (SSC) models (Marscher & Gear, 1985; Maraschi et al., 1992; Tavecchio et al., 1998). The SSC models take into account physical parameters including the strength of the magnetic field, the size of the emission region, the Lorentz factor of the relativistic particles, and the initial electron distribution. An example of an SSC model as in Ghisellini et al. (1996) or Tavecchio et al. (1998) demonstrates how multiwavelength observations allow these physical parameters to be constrained.

The general assumptions of the model are a homogeneous blob of electrons moving relativistically with Lorentz factor Γ that emits synchrotron photons and scatters those photons to gamma-ray energies through the inverse-Compton process. The emitting electron spectrum may be modeled by a broken power law with a break energy γ_b, where $\gamma_b = E/m_e c^2$. The break in the distribution represents the loss of efficiency at higher electron energies due to radiative cooling. This cooling is only relevant if a finite time injection of the electrons is assumed. The emission must be dominated by the peak in the electron population at γ_b, which is responsible for the locations of both peaks of the blazar SED. Because a single population of electrons provides the synchrotron emission and IC scatters that same synchrotron emission, the IC peak frequency relates to the synchrotron peak frequency by the square of the break energy, $\nu_{IC} \simeq (4/3)\gamma_b^2 \nu_{Synch}$. Simultaneous measurements of the frequencies and intensities of the SED peaks fix the values of γ_b, B, and δ within the framework of the SSC model.

Observations of the frequency of both peaks determine the break energy:

$$\gamma_b \simeq (\frac{3\nu_{IC}}{4\nu_{Synch}})^{1/2}$$

The average synchrotron peak frequency can be calculated for an electron of energy γ_b as

$$\nu_{Synch} = 3.7 \times 10^6 \gamma_b^2 \frac{\delta}{(1+z)}$$

where z is redshift. Combining the above relations leads to an estimate of the magnetic field, B, and relativistic Doppler factor, δ, in terms of the peak frequencies.

$$B\delta = (1+z)\frac{\nu_{Synch}^2}{2.8 \times 10^6 \nu_{IC}} \tag{2.1}$$

In the case that δ is unknown, the magnetic field can be estimated for a typical value of $\delta \sim 10$ to be $B \simeq (1/37)(\nu_{Synch}/10^{14} Hz)^2/(\nu_{IC}/10^{22} Hz)$.

The ratio of synchrotron and IC luminosities reveals the relative dominance of the two emission mechanisms, which relates to the magnetic energy density U_B and

the radiation energy density in the comoving frame $U^{'}_{Synch}$.

$$\frac{L_{Synch}}{L_{IC}} \simeq \frac{U_B}{U^{'}_{Synch}} = \frac{4\pi R^2 c U_B \delta^4}{L_{Synch}}$$

Note that $U_B = B^2/8\pi$ and $U^{'}_{Synch} = L_{Synch}/4\pi R^2 c\delta^4$. If R is determined from time variability, $R \leq \delta c t_{var}$, then the luminosities determine the combined magnetic field strength and Doppler factor

$$B\delta^3 \simeq (1+z)(\frac{2L^2_{Synch}}{L_{IC}c^3 t^2_{var}})^{1/2} \tag{2.2}$$

Using Equations 2.1 and 2.2 gives

$$\delta = 1.67 \times 10^4 (\frac{\nu_{IC}}{t_d \nu^2_{Synch}})^{1/2} (\frac{L_{Synch}}{L_{IC}})^{1/4}$$

and

$$B = 2.14 \times 10^{-11}(1+z)\frac{\nu^3_{Synch} t_d^{1/2}}{\nu^{3/2}_{IC}}(\frac{L_{IC}}{L^2_{Synch}})$$

where the luminosities are express in $10^{45} ergs/s$ and t_d is the variability time scale measured in days. The magnetic field strength, relativistic Doppler factor, and peak energy of the emitting electron distribution are all constrained by observations of both SED peaks and the time variability of the energy output.

Within the SSC model the variabilities of TeV and X-ray luminosities are predicted to be closely correlated since they arise from the same electron and photon populations. Changes in the emitting electron population affect both the synchrotron and the IC emission. The cross sections for the interactions vary with different powers of the peak Lorentz factor for the emitting electron distribution. The cross section for the synchrotron process depends linearly on the Lorentz factor while the cross section for the inverse-Compton process depends on this factor quadratically due to the emitting electrons and the synchrotron photons. In the event of a shift in the peak electron energy, the relation of VHE gamma-ray to X-ray flux will have a quadratic relation. If the scattered photon population predominantly includes photons produced externally to the jet, then the relationship should be linear instead. BL Lacs are generally known for X-ray spectra that harden with luminosity, suggesting that the TeV spectral index should change by a related amount. Simultaneous TeV and X-ray observations do not yet clearly support or completely exclude the SSC model. The presence of some incidences of correlated increase in the TeV and X-ray fluxes favors the SSC model over most proton emission models which do not naturally predict any correlation. The observation of independent flaring in TeV and X-ray wavebands, however, requires a more complicated model.

The SSC model fits reasonably well to the relatively small amount of simultaneous multiwavelength data available for AGN detected at TeV energies. The observed SEDs can be fit although the physical range reasonably expected for the magnetic field and bulk Lorentz factor are not well bounded. There is some dispute over what

values are too large in fits of some of the observed data. SSC models correctly predict the correlated increases in X-ray and TeV gamma-ray fluxes often observed during flaring. The same objects have also been observed to flare in only X-ray or TeV gamma-ray bands (Krawczynski et al., 2004; Rebillot et al., 2003). This behavior cannot be explained by SSC models, but other lepton-based models may account for the uncorrelated behavior. The SSC models also fail to account for blazars that have more luminosity in the IC peak than the synchrotron peak (Aharonian et al., 1999; Horan et al., 2002). This counters the expectation of a lower luminosity in the IC peak due to a loss of efficiency in the IC scattering process for ultra-relativistic electrons.

Modifications to lepton model that included IC scattering of external photon populations provide some explanation for both types of observations. Variations of the leptonic model that include additional regions of emission within the jet could also explain the more complicated temporal behavior that is observed. More simultaneous observations are necessary to better constrain and differentiate between these models. The energy spectrum at the highest emission energies is most sensitive to differences in the emission models. Observations above the peak of the second emission component are necessary to distinguish among competing models and completely constrain the physical input parameters.

In addition to explaining the shape of the energy spectrum, emission models also must be consistent with the rapid time variability and dramatic changes in flux level observed in blazars. Some change in the source environment or the physical characteristics of the jet increases the efficiency of the acceleration mechanism over periods of time varying from $\sim$15 minutes to hours with strong episodes possible over several months (Gaidos et al., 1996; Krennrich et al., 1999). An increase in efficiency moves the peaks in the SED to higher frequencies. The shifting of the energy distribution moves the strongest emission into the regions where it can be detected by X-ray and gamma-ray detectors. The shift of the peaks causes the shape of the spectrum visible in an energy band to change during a flaring state. TeV observations indicate some degree of hardening, or decrease in the spectral index, of the spectrum during flares that is consistent with this picture (Aharonian et al., 2002a).

2.4 Infrared Background Absorption

TeV photons are at the appropriate energy to interact with infrared (IR) photons, a component of the extragalactic background light (EBL). Starlight and re-radiated starlight from interstellar dust contribute to a population of photons that interact with TeV photons to produce electron-positron pairs (Gould & Schréder, 1967; Stecker, 1999; Primack et al., 1999; Vassiliev, 2000). The EBL has been measured at some wavelengths, but at others a direct measurement is quite difficult due to the level of foreground radiation. The current observations of the EBL are shown in Figure 2.4 along with the results of an empirical model. At wavelengths between 0.1-30 μm only upper and lower limits are available. Observations of spectral features at

gamma-ray energies can produce alternative methods of measurement in this range of the EBL spectrum.

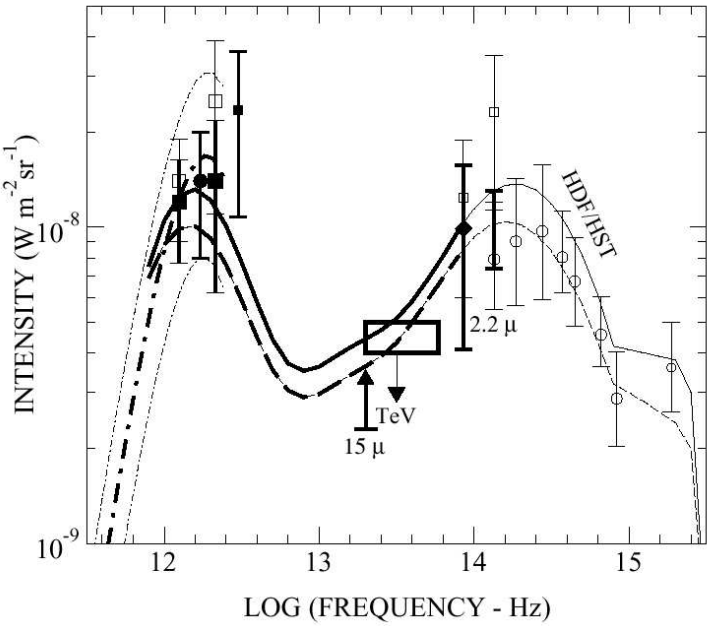

Figure 2.4: Measurements and models of the extragalactic background. The solid and dashed curves correspond to luminosity evolution models from Malkan & Stecker (2001). The frequency range that can be constrained with TeV observations of AGN is marked. Figure taken from Konopelko, Mastichiadis, Kirk, de Jager, & Stecker (2003).

A large sample of extragalactic TeV objects over a range of redshifts are required to fit the effects of the spectrum due to the EBL. The spectrum at the source is not well modeled yet. The shape of the spectrum at the highest energies is particularly susceptible to variations from source to source depending on differences in the detailed characteristics of the individual galaxies. It will take many objects to deconvolve the form of the unattenuated spectra from TeV observations. This is partially due to the likely confusion caused by other attenuation effects that may occur at the source. Additionally, because the form of EBL does not cause a distinctive cutoff in energy, but a broad curvature or overall reduction in luminosity, observations below the energies affected by EBL attenuation are the only unambiguous method of normalizing to the unattenuated spectrum. This type of measurement is not currently possible, but will be available with GLAST (Chen et al., 2004).

The precise amount of attenuation due to pair production on the EBL is not well known, but it is known to have an appreciable effect on TeV observations. It is believed to be the primary reason that TeV emission has not yet been detected from more HBLs. Measurements of TeV spectra indicate curvature that is not consistent with a sharp cutoff, but does not rule out attenuation due to the IR background.

To attempt to remove the effects of IR attenuation from measurements of the flux from AGN, models of the SED of the EBL can be applied. Although measurements

of the EBL are unavailable at the wavelengths most relevant to the absorption of TeV photons, other portions of the SED are measured and can be used to tune and constrain models of the EBL. Several approaches are taken to predict the density of radiation from UV to IR wavelengths. One approach develops the opacity of the universe by modeling galaxy formation and predicting the resulting contributions to light levels and dust content throughout the development of the universe (Primack et al., 1999). Primack et al. (1999) develop semi-analytic models (SAMs) for the galaxy formation using several cosmologies and star formation rates. Another approach uses the present-day galaxy luminosity function and predicts opacity to photons by evolving it back through redshift (Malkan & Stecker, 2001; de Jager & Stecker, 2002). The rate of evolution is altered to predict a "baseline" and a "fast evolution" model. The optical depth predicted by three models of the EBL is shown in Figure 2.5. Results of the "baseline" and "fast evolution" models from de Jager & Stecker (2002) are shown. The semi-analytic model shown is from a parameterization in Bullock (1999) for a Λ cold dark matter (LCDM) cosmology and the Salpeter initial mass function. The fast evolution model predicts the most attenuation while the ΛCDM SAM model predicts similar attenuation at 100 GeV and less above 1 TeV.

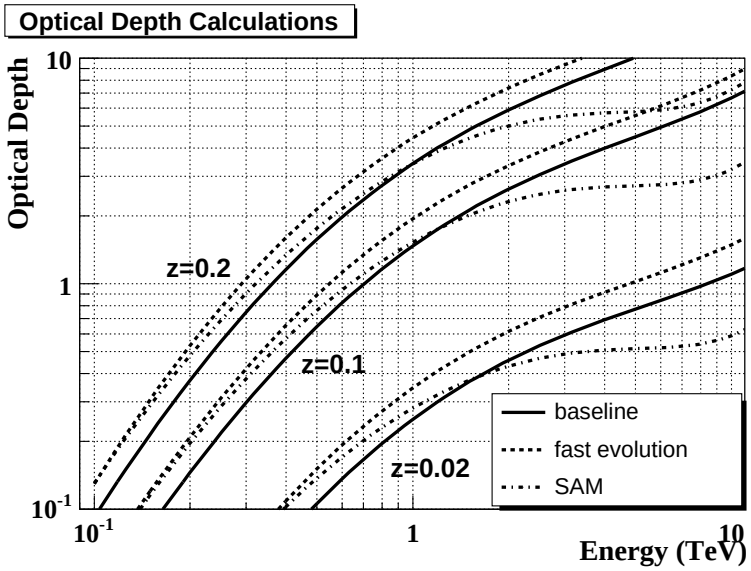

Figure 2.5: Optical depth of the universe to very high energy photons for several redshifts using three models of the EBL. Baseline and fast evolution from de Jager & Stecker (2002) and SAM for LCDM (Salpeter) from Primack, Bullock, Somerville, & MacMinn (1999). When the optical depth is 1, the photon survival probability is 1/e.

2.5 Selection of TeV Candidate BL Lacs

In Costamante & Ghisellini (2002) a sample of BL Lacs are selected as favorable sources of TeV emission based on brightness in X-ray and radio surveys. Costamante and Ghisellini argue that in this range the electron population and seed photon population that contributes to the highest energy photon emission are maximized. The previously observed TeV emitting BL Lacs, Mrk 501, Mrk 421, H 1426+428, 1ES 2344+514 and PKS 2155-304 fall within this parameter space (Table 2.1 and one of the selected sample, 1ES 1959+650, has since been detected by IACTs. The criteria used in Costamante & Ghisellini (2002) select thirty-two objects from several BL Lac samples as the best TeV candidates. Of this set twenty-seven fall within the field of view of Milagro which extends from approximately 0° to 80° DEC. Table 2.2 lists the BL Lacs included in the search and their equatorial coordinates. The table also summarizes the observations status for each BL Lac. Some already have TeV limits, but those with large redshifts or low flux predictions have not been observed by IACTs to date.

Name	RA (J2000)	DEC	Redshift	Type
NGC 253	00 47 06	-25 18 35	0.0006	Starburst
3C 66A	02 19 30	+42 48 30	0.444	LBL
Mrk 421	11 04 27	+38 12 32	0.031	HBL
M87	12 30 49	+12 23 28	0.004	Radio
H 1426+428	14 28 33	+42 40 20	0.129	HBL
Mrk 501	16 53 52	+39 45 36	0.034	HBL
1ES 1959+650	19 59 59	+65 08 55	0.048	HBL
PKS 2155-304	21 58 52	-30 13 32	0.117	HBL
BL Lacertae	22 02 43	+42 16 40	0.069	LBL
1ES 2344+514	23 47 05	+51 42 18	0.044	HBL

Table 2.1: Summary of extragalactic TeV detections. See Horan & Weekes (2004) for a review.

Costamante and Ghisellini use optical, radio, and X-ray data for each candidate to fit the spectral energy distribution (SED). Using the results of the fit, they predict the integral photon flux above several energies. Two types of models are applied to fit the SEDs (example in Figure 2.6). The first is the phenomenological model of Fossati (Fossati et al., 1998) with modifications by Donato and Costamante for low power BL Lacs. The Fossati parameterization predicts the location of the IC peak and the relation of IC to synchrotron luminosity using the blazar sequence. Costamante & Ghisellini (2002) adjust the luminosity relationship to better represent low power BL Lacs. The SED peaks are fit using parabolic forms that depend on the measured radio flux.

The second model is an homogeneous, one-zone synchrotron self-Compton (SSC) model with a finite time electron injection. This assumes one small emission region of

Name	RA (J2000)	DEC	RA (J2000)	DEC	z
1ES 0033+595[3 4]	00 35 52.6	+59 50 05	8.97	59.83	0.086
1ES 0120+340[4]	01 23 08.5	+34 20 48	20.78	34.35	0.272
RGB 0136+391	01 36 32.4	+39 05 59	24.14	39.10	0.2*
RGB 0214+517[3 4]	02 14 17.9	+51 44 52	33.57	51.74	0.049
3C 66A[1 2 3]	02 22 39.6	+43 02 08	35.67	43.04	0.444
1ES 0229+200[2 3 4]	02 32 48.4	+20 17 16	38.20	20.29	0.139
1H 0323+022[3 5]	03 26 14.0	+02 25 15	51.56	2.42	0.147
1H 0414+009[2]	04 16 52.5	+01 05 24	64.22	1.09	0.287
1ES 0647+250[2]	06 50 46.5	+25 03 00	102.69	25.05	0.2*
1ES 0806+524[3 4]	08 09 49.1	+52 18 59	122.45	52.32	0.138
RGB 0812+026	08 12 01.9	+02 37 33	123.00	2.63	0.2*
OJ 287[1]	08 54 48.9	+20 06 31	133.70	20.11	0.306
1H 1013+498	10 15 04.1	+49 26 01	153.77	49.43	0.200
1ES 1028+511[3]	10 31 18.4	+50 53 36	157.83	50.89	0.361
RGB 1117+202[4]	11 17 06.2	+20 14 07	169.28	20.24	0.139
MRK 180[3]	11 36 26.4	+70 09 27	174.11	70.16	0.045
RGB 1136+676	11 36 30.1	+67 37 04	174.12	67.62	0.135
ON 325[1 3]	12 17 52.1	+30 07 01	184.47	30.12	0.237
1H 1219+301[3]	12 21 21.9	+30 10 37	185.34	30.18	0.182
RGB 1417+257	14 17 56.7	+25 43 26	214.49	25.72	0.237
1ES 1440+122	14 42 48.2	+12 00 40	220.70	12.01	0.162
1ES 1553+113[4]	15 55 43.0	+11 11 24	238.93	11.19	0.360
RGB 1725+118[3]	17 25 04.3	+11 52 15	261.27	11.87	0.018
I Zw 187[1 3]	17 27 18.6	+50 13 10	262.08	50.22	0.055
1ES 1741+196[3]	17 43 57.8	+19 35 09	265.99	19.59	0.084
1ES 1959+650	19 59 59.9	+65 08 55	300.00	65.15	0.047
BL Lacertae[1 2 3]	22 02 43.3	+42 16 40	330.68	42.28	0.069

Table 2.2: BL Lacs selected as likely TeV emitters by Costamante & Ghisellini (2002) that pass within the field of view of Milagro. Several have unknown redshift and are given the sample mean for the purpose of calculations. Previous TeV observations are noted.
*: unknown z set to be 0.2
[1] 1992-1994 Kerrick et al. (1995); [2] 1997-1998 Aharonian et al. (2000a); [3] 1995-2000 Horan et al. (2004); [4] Oct. 2001-Jul. 2002 de la Calle Pérez et al. (2003); [5] Sept. 1996 Chadwick, Lyons, McComb, Orford, Osborne, Rayner, Shaw, & Turver (1999)

synchrotron emitting electrons and no spatially dependent variations in the physical characteristics of the jet. The finite time of the injection causes electrons to have a characteristic cooling time due to radiation that steepens the electron energy spectrum at high energies. SSC models in general predict less emission at TeV energies than the Fossati type model due to the energy dependence of the IC cross section

discussed earlier in this chapter.

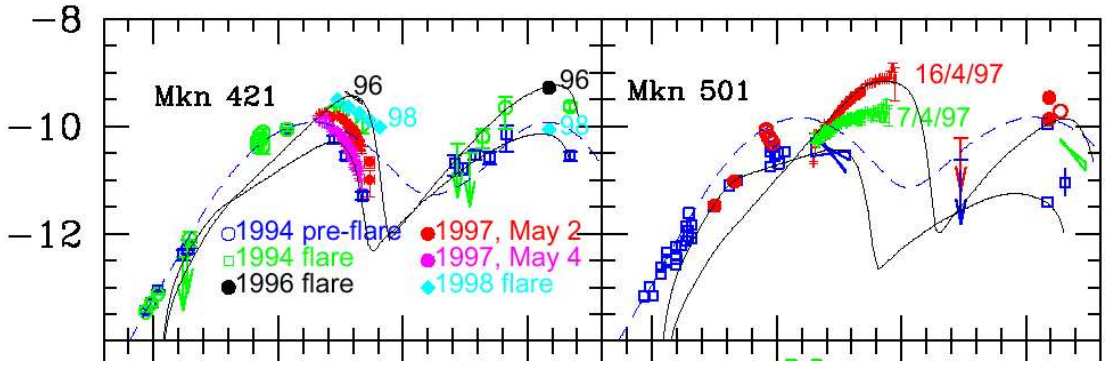

Figure 2.6: Spectral energy density (SED) fits to blazars Mrk 421 and Mrk 501 from Costamante & Ghisellini (2002). The solid lines represent SSC fits and the dotted line the modified Fossati model fit. The y axis is log νF_ν in $ergs/cm^2s$. The x axis is log ν from 10^8 to 10^{28} Hz.

2.6 Summary of Searches for Predicted TeV Candidates

BL Lacs have been the subjects of several searches, some successful, by TeV instruments. Most of the searches to date include only a few HBLs and cover limited periods of time. Typically, only the few closest BL Lacs have been included in the interest of maximizing the limited observational time available to IACTs. The CANGAROO collaboration has reported upper limits on 4 HBLs in the Southern Hemisphere (Roberts et al., 1998, 1999). The Durham group observed 3 different HBLs in the Southern Hemisphere (Chadwick et al., 1999) one of which is near the equator and is included as part of the sample considered in this work. The most extensive searches have been conducted using the Whipple gamma-ray telescope. An early search in Whipple (Kerrick et al., 1995) included a few HBLs, but more recent campaigns have focused on a larger sample and made short, frequent observations to target flaring. The sample in Costamante & Ghisellini (2002) has generated particular interest with the selection of the most extreme blazars. The flux predictions offer guidance for the necessary length of IACT observations required for constraint and a way to connect results to model predictions.

Whipple and Milagro are located at similar latitudes and, thus, have a large overlap in observed sources within this sample. The temporal characteristics of the observations, of course, differ substantially. The Whipple results for eight of the HBLs examined in this work are presented in de la Calle Pérez et al. (2003) and an additional fourteen are part of a longer term search presented in Horan et al. (2004). No detections in Whipple are reported excluding the discoveries previously mentioned. The observations presented in Horan et al. (2004) extend from 1995 to 2000 and have no temporal overlap with the search presented in this work. The eight

sources subject to a search in de la Calle Pérez et al. (2003) include observations for several to 20 hours per source from October 2001 to July 2002 and have only partial temporal overlap. The integral flux limits set by Whipple above 1 TeV are all below 0.1 of the Crab flux. The sources were each observed long enough to obtain a 5σ detection of the predicted flux.

The transient nature of the emission expected and the detections of formerly TeV-quiet BL Lacs suggests that previously undetected sources should not be discounted as potential TeV emitters. The limited scope of the IACT surveys in terms of sample size and time coverage make the observations in Milagro a unique study of the time-integrated behavior of these sources over a variety of durations. In some cases the Milagro observations of these objects provide the only TeV observations available for the time period examined here.

Chapter 3

The Milagro Detector

The Milagro Gamma-Ray Observatory is a ground-based TeV detector that makes use of the water-Čerenkov technique described in Chapter 1. The wide field of view ($\sim$ 2 sr), low energy threshold ($\sim 100GeV$), and high duty cycle ($> 90\%$) make Milagro an excellent survey instrument and provide observations of a broad range of gamma-ray and cosmic-ray phenomena. The details of the detector configuration, trigger conditions, and reconstruction algorithms, that in combination provide the stored data for further analysis, are described. Because this is a relatively new technique, an overview of its development is also included to put the current status in perspective and to indicate possible directions for further development.

3.1 Pond Layout and PMTs

The Milagro Observatory is located near Los Alamos, NM, in the Jemez mountains at latitude 35° 52' 45" and longitude 106° 40' 37" West. The altitude of the detector is 2630 m (8690 ft, 750 g/cm) to allow detection of EAS particles that do not survive to larger depths of the atmosphere. The Milagro detector consists of a 80 m $\times$ 60 m $\times$ 8 m deep pool instrumented with 723 photo-multiplier tubes (PMTs). The pool is covered with a polypropylene cover to block light and act as a protective barrier. The pond PMTs are in two layers attached to a weighted PVC grid anchored to the bottom of the pond with 2.8m spacing. The top layer sits 1.5m below the surface of the water. The 450 PMTs that make up the top layer, known as the air shower (AS) layer, are used primarily to reconstruct the core location and direction of an air shower. The second layer contains 273 PMTs placed at 6m below the surface with the exception of an outer ring of PMTs that must sit slightly higher due to the upward slope of the pond floor. It is called the muon layer (MU) because it acts as an imaging calorimeter that can detect penetrating particles such as muons that deposit dense clumps of energy in the detector. As indicated in Figure 3.2, the MU layer PMTs are horizontally offset from the AS layer PMTs by half the grid spacing to displace them from being directly beneath the AS PMTs. An additional array of 170 outrigger tanks, each containing a single PMT, surrounds the pool to provide sampling of a triggerring EAS over a larger area.

The reconstruction of air showers requires PMTs with fast response and good charge resolution. The PMTs used in Milagro are 20 cm in diameter (Hamamatsu

Figure 3.1: The Milagro site in the Jemez Mountains of New Mexico. The central, covered pond is surrounded black outrigger tanks. Some snow is visible on the cover.

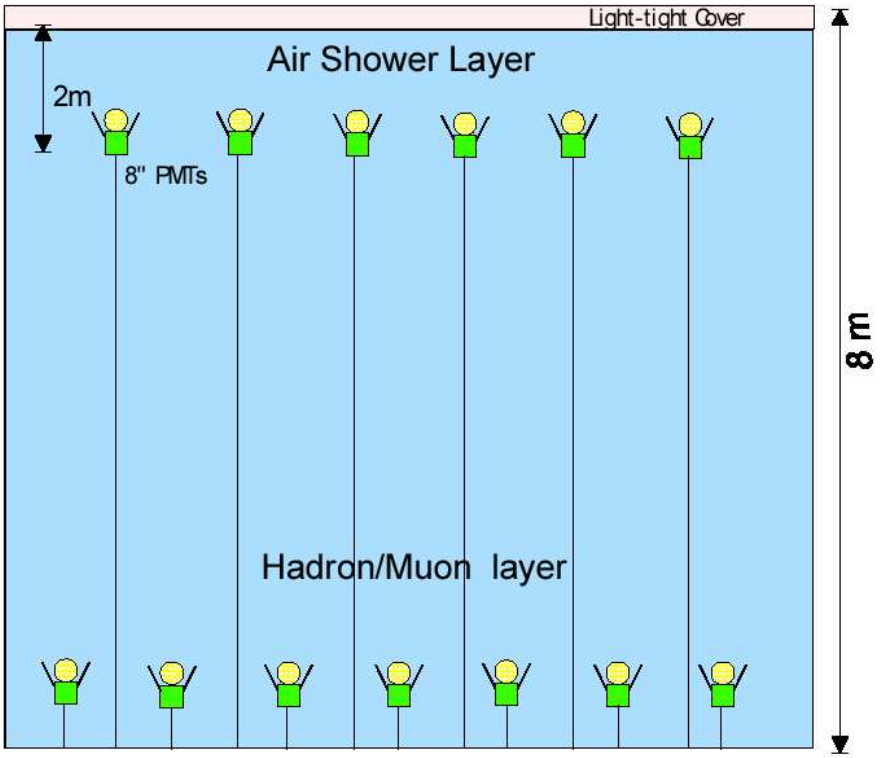

Figure 3.2: Illustration of PMT placement in the pond.

#R5912SEL). The electronic base for each tube is protected by a waterproof PVC housing. An RG-59 coaxial cable carries DC high voltage from the counting house to the PMT base and AC signal pulses from the base to the electronics system. The initial high-voltage Fisher connector used to attach the cable to the PMT base has a high failure rate when submerged in water. Several varieties of connectors have been

tested to correct this problem and prevent PMT "drowning". A reliable connector has been found in a combination of several applications of heat shrink applied to the spliced cable at the connection to the PMT base and to the access tube entering the PMT housing. PMTs using the initial Fisher connectors, however, still occasionally experience leaks, which require their removal from the pond for repairs. In additiona to failures due to leaks, the PMT base electronic components occassionally fail and require replacement. More than seventy PMTs have been taken out of the pond for repairs in past years, but this number has been decreasing each year as the Fisher connectors are replaced with the heat shrink method.

The PMTs are buoyant and are held below the surface of the water by Kevlar strings, which anchor them to a weighted PVC grid on the floor of the pool. To access the PMTs for repairs, SCUBA divers attach a system of floats and weights that allow the PMTs to be removed and replaced using boats. The divers attach a weight to the PMT to offset its buoyancy and a string which attaches to a float on the surface of the water. Then, the string which normally secures the PMT to the grid is removed and attached instead to the float, which serves as the access point and location marker. The PMTs are drawn up into boats using a string linked to the PMT. The high voltage cable is then removed from the PMT base and left attached to the grid point freeing the PMT for repairs. Once repaired, the PMTs are returned to the pond by boat and reconnected to the high voltage/signal cable. The PMTs are fixed to the grid again in a similar fashion to the removal process, with divers attaching the PMT to the Kevlar string connected to the grid and releasing the float.

The AS layer PMTs are outfitted with reflective cones, dubbed baffles, that fit like a collar around the PMT housing just below the photocathode. The baffle serves two purposes by blocking light from hitting the photocathode from below or horizontally and by slightly increasing the collection area. The baffles prevent scattered and reflected light from making late hits after a shower passes through the pond. Late hits cause error in the angle fitting and can cause a systematic effect in pointing. The first baffles were made of an inner cone of anodized aluminum sitting an external cone of black polypropylene but are now being replaced by a single cone of polypropylene with a white interior and black exterior. Aluminum was originally chosen because the reflectivity increases the collection area for the PMT. Small flaws in the anodizing have allowed the aluminum to corrode in the water over time leaving a deposit of aluminum oxide, a white chalky powder, on the PMTs and in the pond water. The white polypropylene now being used shows little change in the detector response, and does not degrade in water.

3.2 Light-Tight Cover

A sealed light-tight cover is used to prevent outside light from entering the pond. Because of the phases used to construct Milagro and the need for repair access, a cover and fan system has been developed to allow quick inflation and deflation. This also involves a system of tension ropes to keep the inflated cover in a stable state during the sometimes unstable weather of the Jemez Mountains. The cover is held

at points along the edges which are adjusted to be tight during normal operation and looser for inflation. Several long nylon cables run diagonally across the pond to provide additional stability when the cover is fully inflated. In the inflated state, the middle of the cover rises approximately twenty feet above ground level leaving plenty of room for work underneath. Several large fans speed the inflation process, but only smaller fans are necessary to maintain the internal pressure of the cover once inflated. The outside air is filtered to prevent contamination during inflation. The cover can be fully raised with this method in two hours and deflated in about forty-five minutes. The speed of deflation is important to prevent damage to the cover by the thunderstorms and high winds common during the late summer in the Jemez.

After deflation, the cover has residual air pockets that are worked out over time, but may remain for a few days. Because the contact between the cover and the water has a large effect on detector response, the data quality takes a few days to weeks to return to normal operation after repairs. The data rate tracks this effect and falls gradually in dry conditions, or quickly if rain pools on the cover pushing the air out after deflation. Because data cannot be taken during inflation and some time is required to return to normal conditions afterwards, the cover is only inflated once a year.

The thunderstorms common to the Jemez mountains bring lightning as well as wind. Because of the frequent lightning strikes in the area, a large Faraday cage surrounds the pond and associated buildings. It is constructed from telephone poles and large gauge copper wire. A portion of the outriggers fall within the cage, but the majority are outside it. To maintain the protection of the electronics systems, all the outriggers external to the Faraday cage are connected through it using spark gaps. These connectors act like a fuse, disconnecting under high current loads. Although there has been evidence of several lightning strikes close to outrigger tanks, no damage has occurred to the electronics inside the Faraday cage.

3.3 Water System

The pond holds 24-million liters of water. The water is filtered and softened before addition to the pond. Once added, the water is recirculated at 180 Gpm through 10 μm, 1 μm and 0.1 μm filters to maintain transparency. The water also passes through UV lamps before being returned to the pond to prevent any biological growth. The 0.1 μm filters have been removed due to clogging with the aluminum oxide from corroding baffles. Around half of the aluminum baffles were replaced during the Fall 2003 repair and the remaining baffles are scheduled to be replaced during the next repair operation. This will allow the filters to remove the aluminum oxide and return the water to its former quality. Measurements of the attenuation length of the water are made periodically using a laser unit (Coyne & Schneider, 2002). Measurements made in 2002 found an attenuation length of 12 m at 325 nm. Recent tests have shown an increase in the attenuation length to 17 m suggesting that the water transparency remains good despite the corrosion and has not had an adverse

effect on the detection efficiency.

3.4 Electronics System

The electronics system collects and processes the PMT pulses and provides the time and pulse amplitude information to computers for online reconstruction of the events. The PMTs are divided into patches of sixteen tubes that operate at the same high voltage level. Each patch is first processed by custom sixteen channel front end boards that extract the AC signals for each PMT and modify the pulses to measure the charge. The charge in the pulse is used to determine the number of photoelectrons released from the photocathode. This can be done by ADCs but because of expense and the high event rate, Milagro was designed to use the time-over-threshold method. Instead of using ADCs to measure the charge, TDCs are used to mark when the pulse crosses a voltage threshold. This is done for two thresholds, one at ∼1/4 PE and the other at ∼5 PEs. The Lecroy 1887 FASTBUS TDCs used can store up to sixteen edges per channel over a 3 ms period at a resolution of 0.5 ns. The time a pulse spends over each threshold is calibrated for each tube to determine a start time for the pulse and the number of PEs generated. A description of the timing calibrations can be found in Chapter 4.

The front end boards are also responsible for sending a signal from each PMT to the trigger logic. Each PMT pulse that passes the low threshold generates a 200 ns pulse. Before March 2002, these pulses were summed and used to generate a multiplicity trigger. The discriminator voltage level that set the trigger threshold did not precisely match a number of PMTs for the trigger and was often changed to select a desired trigger rate. During that time the most representative ideal trigger level was ∼55 PMTs [1]. Since then, a trigger card that takes the inputs from each PMT has been designed and implemented to provide a more flexible and stable trigger system.

3.5 Programmable Trigger Card

The original Milagro trigger was a simple multiplicity trigger requiring more than ∼60 PMTs to generate signals within a 200 ns window. A high-angle muon crossing the pond horizontally causes a cone of light that produces signals in a large number of PMTs. Events of this type can satisfy the multiplicity trigger condition. This was one of the motivations for adding baffles to AS PMTs to block horizontal light in the pond. The effect becomes a significant background again when the trigger threshold is lowered below 60 PMTs. Because of the cosmological nature of gamma-ray bursts (GRBs) and the impact of absorption of TeV photons on extragalactic background light, lowering the energy threshold is imperative for increasing the probability of de-

[1] The trigger level given here is ideal, not actual, meaning it excludes random PMT signals and represents only PMT pulses associated with an air shower. When random PMT signals are included this number increases by ∼5

tecting a gamma-ray burst with Milagro. Calculations of the opacity of the universe to gamma-rays can be used to define a detection threshold as function of redshift. Figure 3.3 shows the survival probability of gamma rays for several redshifts using a model from Primack et al. (1999).

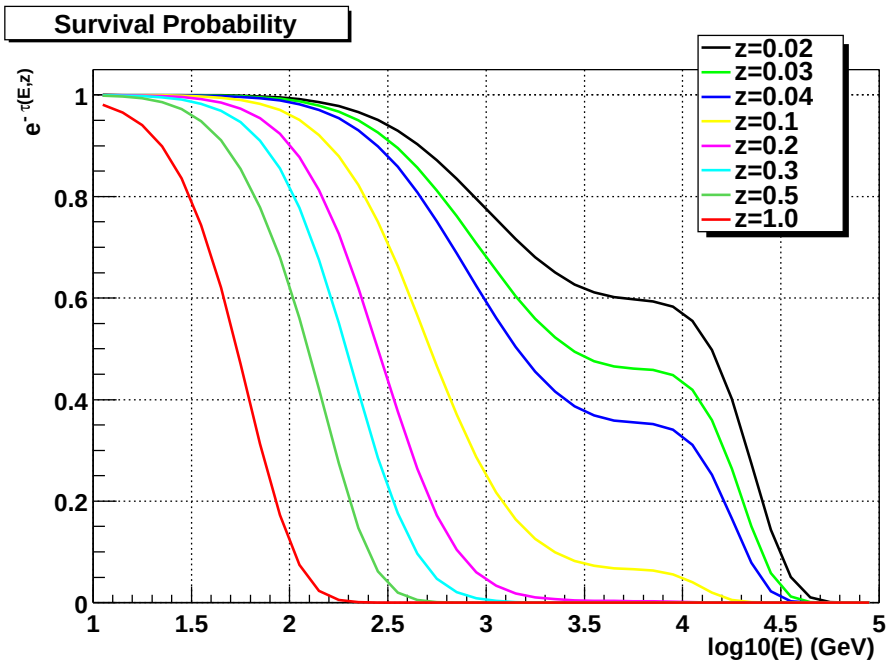

Figure 3.3: The survival probability of photons for energies from 10 GeV to 10 TeV as a function of redshift. The opacity, τ, is determined from models in Primack et al. (1999) for a LCDM cosmology and Salpeter initial mass function using the parameterization from Bullock (1999).

To improve the sensitivity to GRBs, low multiplicity triggers caused by the high-angle muon background must be reduced. This is possible because the arrival of a horizontal cone of light has a different time profile in the PMT arrival times than that of an air shower. While the particles in an air shower travel nearly the speed of light, c, the light from a horizontal muon travels at the speed of light in water, c/n where n is the index of refraction. This means that the hits from a high-angle muon will occur over a longer period of time than those from an air shower. After the angle reconstruction it is easy to remove events caused by high-angle muons because the resulting angles are unphysical. If these events are removed instead at the trigger level, then the trigger threshold can be lowered without a large increase in event rate.

A parameter, risetime, is defined to characterize the arrival times of an event in the PMTs by finding the time interval within which 10-90% of the hits arrive. The risetime distributions for low threshold data that fail the angle fitter show a good separation from the those of passing events and from the risetime distributions for gamma-ray simulations (Figure 3.4). The risetime can be calculated and applied at the trigger level to bias the events passing the trigger at low multiplicities toward

gamma-ray showers while limiting the event rate to below the 2000 Hz limit of the DAQ.

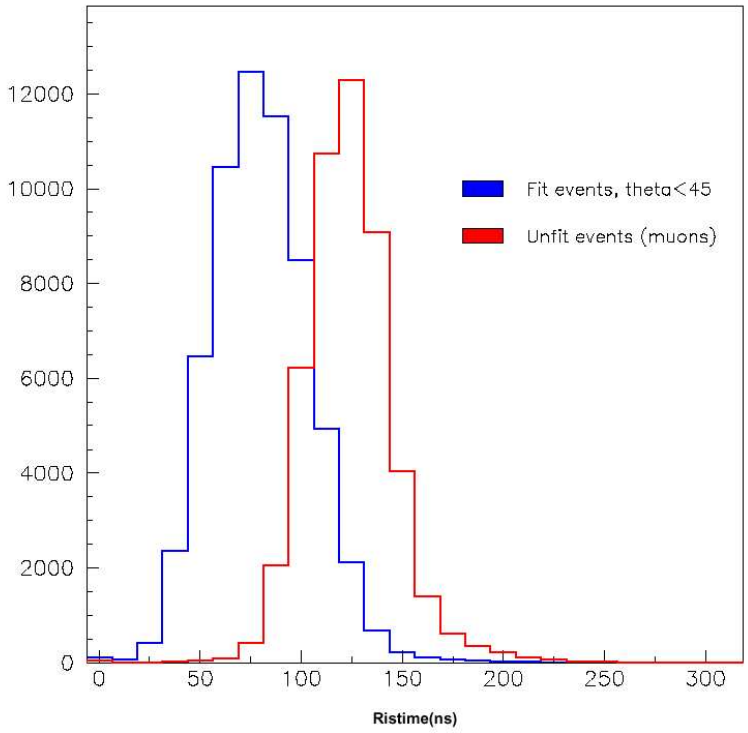

Figure 3.4: Distributions of risetime (10-90% of trigger pulse in ns) for data fits that fail to reconstruct (red) attributed to single muons and detected Monte Carlo simulated gamma-ray showers (blue).

A VME trigger card including a programmable logic device has been developed to allow the implementation of multiple trigger conditions. The card is reprogrammable, which allows the trigger conditions to be changed and expanded with the possibility of incorporating inputs from other cards. The card includes electronics to buffer arrival time information for calculating the risetime.. When one of the programmed multiplicity trigger conditions is passed, the risetime is available as an additional condition for processing the event. Milagro currently operates using four trigger levels simultaneously (Blaufuss et al., 2002):

- multiplicity trigger >74 PMTs
- multiplicity >53 and <74 PMTs, risetime cut keeping 80% of gamma-ray events
- multiplicity >20 and <53 PMTs, risetime cut keeping 65% of gamma-ray events
- multiplicity >20 PMTs, no risetime cut, only accepts 0.1% of passing triggers

With this combination the rate is held to a manageable level of ∼1800 Hz with ∼8% dead time.

The trigger card has been in use since March 2002, with trigger conditions very close to those listed above. The formation of ice in the pond during the winter months causes rates that exceed 1800 Hz, but the lowest PMT multiplicity requirement can be increased to bring the rate to a maneagable level. Although the driving motivation for the trigger card was to improve sensitivity to GRBs, increased detection efficiency at lower energies benefits other sources as well. Gamma-ray sources typically decrease in flux with increasing energy as a power law. The increase in effective area at lower energies improves the sensitivity to any gamm-ray source with a falling spectrum.

3.6 From DAQ to Data Storage

When the trigger card generates a trigger signal the information from the TDCs is read out using a FASTBUS Smart Crate Controller. The event time is set using a GPS clock module. The TDC information for all the channels is transferred into a VME memory module that is then ported to a cluster of PCs for data processing.

Originally, the online computer system consisted of a single 10 processor SGI mainframe. The cheapness and expandability of PCs led to developing a new DAQ controller consisting of a master PC and several PC workers. The DAQ and data processing operates using a client-server architecture in which the master controls the assignment of data blocks to worker processes on several PCs. The workers process the data and return it to the master, which orders the data and routes it to temporary storage on disk to await archiving. The new system began running online in May 2002. Additional workers can be added easily to meet the demand of running more complicated reconstruction algorithms online.

The method of data storage has also changed since Milagro began taking data. Initially, the data was written to DLT tapes at the site, which then had to be physically transferred to other facilities to be read and used for analysis. Since then, the cost of disk space has decreased dramatically. Now, all the reconstructed data is stored on disk arrays and transferred by the network to other facilities. The reading and analysis of data from disk is significantly easier and faster than cycling through DLT tapes and has had a substantial impact on analysis capabilities.

3.7 Online Reconstruction

Raw data, which encompasses all the TDC information for each PMT channel, is prohibitively large and cannot be kept for the whole field of view. A single day of raw data taken while running at 1800 Hz requires $\sim$250 GB of disk space. The raw data that was processed into the reconstructed data set used in this thesis would require more than 200 TB of disk space. Instead of saving all the information associated with each event, only the final results of the angle reconstruction and parameters used for background rejection are recorded to reduce the stored data to a maneagable size. Some raw data is saved for events occurring near the locations of sources of interest like the Crab Nebula, the Moon, the Sun, and the occasional flaring AGN to test and evaluate reconstruction and analysis techniques.

When a trigger condition is met, a common stop is set. The threshold crossings, or edges, from the TDCs are read out, counting backward from the time of the stop. An event develops in the pond over a few hundred ns, but the TDC information goes back further than that to allow the inclusion of signals that have further to travel to reach the counting house. The large time window can contain a variety of noise signals and must be filtered for the egde information relevant to the air shower event that caused the trigger. A well-behaved pulse produces 2 or 4 edges in a TDC, but due to noise and irregular pulses some PMTs are recorded with more than 4 edges in an event. The DAQ accepts all recorded edges for each channel within the 3 ms TDC time window. The best edges are then selected in software as the first step of event reconstruction. The good edges are chosen to fit the time separation and direction crossing the threshold expected from a well-behaved pulse. For example, the first and second edges for a pulse passing the high threshold should fall within a relatively short time range in order to both represent the steeply falling profile of a PMT pulse. The time cuts applied to the separation between adjacent edges eliminate stray edges caused by preceding or following hits that are not related to the shower causing the trigger.

Once the good edges are selected, the time over threshold for these edges is used to calibrate the starting time and the number of PEs for each PMT pulse. The PE values for each PMT are first used to find a shower core position. The lateral energy distribution in an EAS has the highest concentration near the center of the shower plane. Locating this center is necessary to fit the direction of the shower and locate the point of origin on the sky. Several algorithms have been used online since Milagro began taking data. The simplest algorithm uses weighting by PE values to find the center of mass of the hits. The original core fitter used this method, and constrained the core position to be located within the bounds of the pond. Simulations show, however, that a large percentage of gamma-ray showers with cores located externally to the pond can trigger the detector. Because the core position is an important input to the angle fitter, the on-pond constraint caused the reconstructed angle to be wrong for off-pond showers. The second generation core fitter was modified to improve on this method(Sullivan & Smith, 2000). The direction of the core location relative to the center of the pond was determined from the PE distribution, and for off-pond cores, the core was placed a set distance, 50 m, from the center of the pond in that direction. This core fitter was included in the online reconstruction on 15 December 2000. Because of the resulting change in sensitivity, this date is used as the starting point for the archival data set examined in this thesis.

The outrigger array provides additional information about the shower core position when it is located off the pond, and improves the angle reconstruction. A core fitter that includes information from the outriggers has been developed and used in the online reconstruction since Spring 2003. This fitter determines whether the shower core is on or off the pond using pulse height information. Showers falling on the pond are fit with the previously described center of mass fitter. Showers falling off the pond are fit using the outrigger PE information to weight the core location. The data set used for the results presented in this dissertation ends in September 2003. Because the combined center of mass and outrigger fitter does not have a large

impact on the results presented here, it has only been described briefly. More details are available in DeYoung (2003).

The angle fitter reconstructs the direction of the primary particle using the time and PE information from PMTs hit in an event. The arrival time of the recorded PMT pulses are used to do a χ^2 fit of the shower plane. The results of such a fit are shown in Figure 3.5. Before fitting the plane, the calibrated arrival times must be corrected for several effects. One effect, called sampling, corrects the arrival times of pulses to account for large amplitude pulses that appear on average to arrive earlier than small amplitude pulses. This is a separate correction from the "slewing" effect corrected by the timing calibrations (Chapter 4), where the pulse arrival time is corrected for the effect of large amplitude pulses crossing the TDC voltage thresholds earlier than small amplitude pulses. Sampling corrects for the time difference between PMTs hit by one photon as opposed to many photons, which arises due to the thickness of the shower plane. The sampling correction is determined as a function of PEs from Monte Carlo simulation and data optimization.

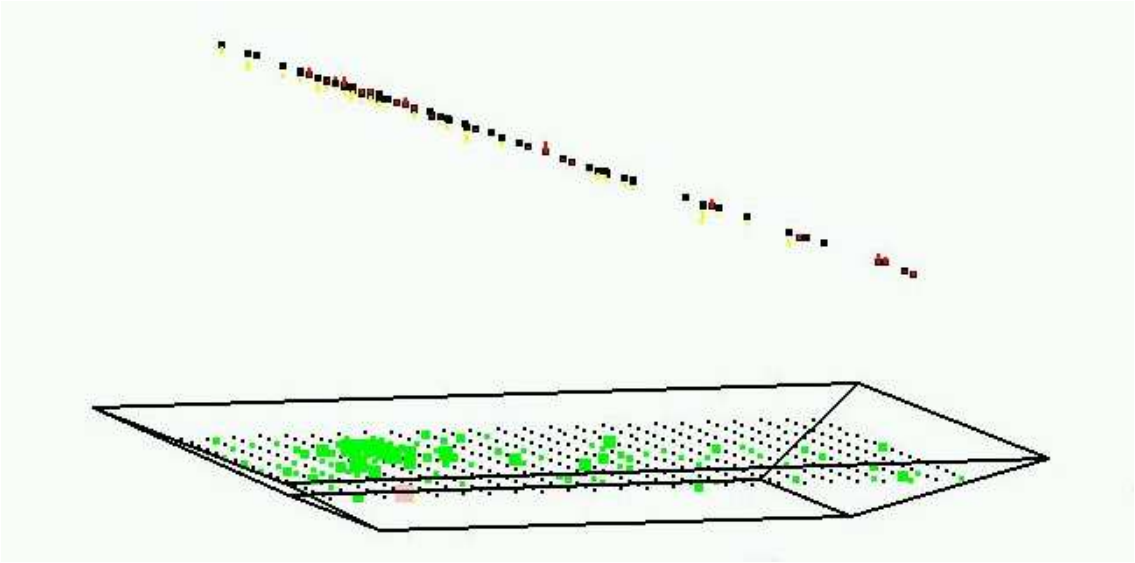

Figure 3.5: Reconstructed shower plane using times from AS PMTs. The yellow lines from the points in the plane indicate the time difference of the PMT time from the fit.

A curvature correction is made for the shape of the shower front. The shape has curvature and is not a true plane. In order to apply a simple plane fit, the time differences due to the curvature of the shower front are removed from the PMT arrival times to make the effective shape a plane. The curvature correction depends on the distance bewteen the PMT and the shower core and can be determined from Monte Carlo gamma-ray simulations.

The reconstructed angle is determined from five successive passes of a χ^2 fit of a plane to the arrival times corrected for calibration, curvature, and sampling. The arrival times are weighted in the fit by PE value to allow the stronger hits to have more influence on the fit. In each successive pass of the fitter, PMTs with poor

residuals are removed from the fit, and the cut on the minimum PE value for a hit to be included is decreased. The overall concept is to fit first without the low PE hits, which are more likely to be noise or scattered light, and then, to remove outliers, bring in lower PE hits, and repeat. If the angle fitter successfully deduces a physically meaningful direction, the local angles (θ,ϕ) are saved in the reconstructed event. Otherwise, a failure value is set. Occassionally, the reconstructed direction of the shower front does not make physical sense, and the event is marked as not fit. During typical operation, the percentage of events fit is $\sim$89%. The results of the angle and core fits along with parameters relevant to gamma-hadron separation algorithms are saved and stored for later analysis.

3.8 Development of the Milagro Detector

The Milagro site was previously part of Hot Dry Rock, a geothermal experiment on Fenton Hill, near Los Alamos, New Mexico. The key component, a large holding pond, was already in place, but had to be cleaned out and lined for use as a detector. An inflatable cover system was installed to provide a light-tight cover during data taking and to allow access to the pond for construction and repairs. An weighted PVC grid was placed on the bottom of the pond with 28 PMTs attached. This mini prototype was referred to as Milagrissimo and took data in the spring of 1996 to test the water-Čerenkov technique.

After Milgrissimo, the PVC grid was extended to the entire bottom of the pond and instrumented with 228 PMTs. The full prototype was called Milagrito and ran from February 1997 to April 1998. The water level was varied to determine the optimal depth of PMTs below the water surface for shower reconstruction. Milagrito was also used to test the laser calibration system designed to determine time and pulse amplitude conversions for each PMT. Observations made with Milagrito produced detections of the AGN Mrk 501 and evidence for TeV emission concident with GRB 940417.

The Milagrito detector was expanded to become Milagro. An additional 495 PMTs were added to the existing ones to fill out the bottom layer and add a second layer above it. The two layer design intends the top layer to be used for angle reconstruction and the deeper bottom layer to provide additional information about energy distribution useful for gamma-hadron separation. The pond expansion was completed and Milagro began taking data in December 1999. Data from the early phase of Milagro was used to develop background rejection and improved fits to the shower core. By July 2000, the reconstructed data saved for the entire field of view contained the parameters necessary for background rejection. The improved core reconstruction was added on 15 December 2000 and was used to define the starting point for analysis using the reconstructed data.

Additional construction continued from 1999 through 2003 to add 175 outlying tanks to the 40,000 m^2 area around the Milagro pond. The tanks, known as outriggers, are 3 m in diameter and 1 m high. Each is filled with water and contains a single PMT. They provide information about portions of an air shower falling outside the

boundaries of the pond. The installation of the outriggers was a major undertaking partially due to the Cerro Grande fire that occurred in Los Alamos in June, 2000. The unavailability of construction contractors following the fire led to the use of all available collaborators to install the tanks and accompanying 1000 ft signal/HV cables. By Fall 2002, signals from operational outriggers were included in the recorded data. As of Spring 2004, all the outriggers are operational and the array is nearly calibrated.

Milagro has a high duty cycle, with a live time of $\sim 91\%$ during three years of operation. Data is acquired continuously with a few exceptions. Occasional power glitches can cause a small amount of down time, typically a few hours. A few hardware problems have stopped data taking for a day or two. Longer gaps in data have occurred during PMT repairs. The repairs are conducted every September for one or two weeks. The experiment is stopped for the duration of the repair to allow the cover to be raised for accessing the pond and PMTs.

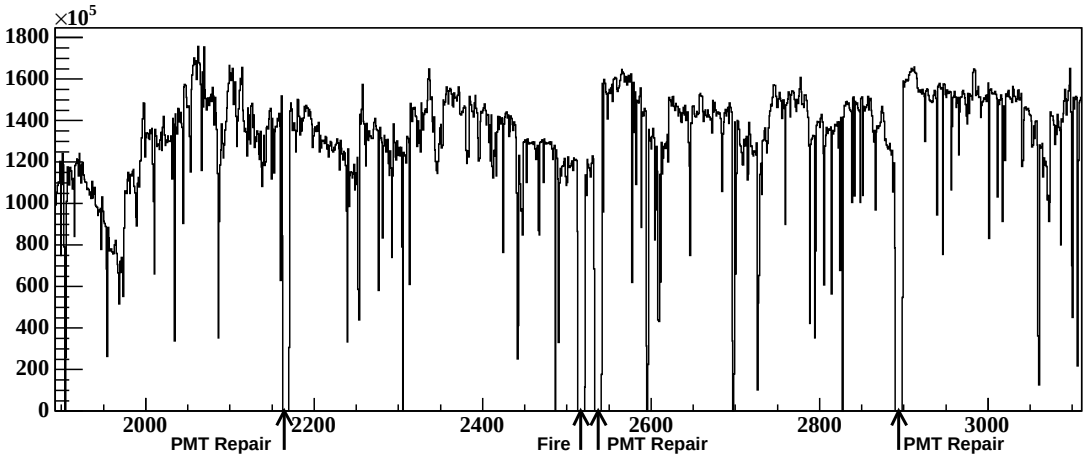

Figure 3.6: Timeline of recorded data events for each day from 15 December 2000 through 14 April 2004. Time is given in days using MJD-50,000. Significant gaps are visible for shutdowns caused by a forest fire near the site and PMT repairs.

The forest fires common in New Mexico during the summer months have caused more significant down time. During the Cerro Grande fire in June 2000, Los Alamos was evacuated. The experiment could not operate for several days until the lab was reopened and the road to the Milagro site cleared. A second fire occurred very near to the Milagro site itself in August 2002. Fortunately, it caused no direct damage. However, the Fenton Hill site was evacuated for ten days and no data was taken during that time.

Since the pond became operational, Milagro has detected several gamma-ray sources. In ~ 3 years of data, the Crab Nebula appears as a 6σ detection (Atkins et al., 2003). Mrk 421 has flared several times, and for the whole data set is detected at the 5σ level. For the period from 14 June 2000 to 24 April 2001, which included a major flare, the observed event excess corresponds to 4σ (Benbow, 2002). The Milagro survey of the entire field of view sets the strongest limits available for an

all-sky search for steady TeV emission in the Northern Hemisphere (Atkins et al., 2004b). Additionally, the shadow of the Sun in cosmic rays has been studied for the presence of a signal from WIMP annihilation (Fleysher, 2003). The Moon shadow in cosmic rays has been studied to understand the angular and energy response of Milagro. Several solar flares have been detected in the summed PMT counting rates, or scalers. An analysis of the Galactic Plane finds emission from a region including the Cygnus Arm with significance $> 4\sigma$. Studies are ongoing that include a search of the entire field of view for GRB emission and for coincident emission from satellite-detected GRBs that fall within the field of view.

A more detailed description of the Milagrito prototype can be found in Atkins et al. (2000b). Many of the prototype systems (water, cover, lightning, electronics) are identical to those in the Milagro detector. The major differences lie in the addition of baffles to the AS layer PMTs and the addition of the outrigger array. The status of the Milagro detector in 2001 including the early construction of outriggers is described in Sullivan (2001). In the near future, angle-fitting algorithms using the outriggers will be included in the online reconstruction in addition to the core fitting algorithm described here. Improvements to event reconstruction making use of the outrigger array and the bottom layer PMTs shows promise for increasing angular resolution and gamma-hadron separation. Improvements in both areas will increase the sensitivity to gamma-ray sources and make detections possible in shorter exposures.

Chapter 4

Timing Calibrations

The reconstruction of an air shower angle and core position requires knowledge of the time each PMT produces a signal and the total charge contained in the signal. The arrival time and photoelectron (PE) values of the signals must be calibrated to allow unbiased comparisons between PMTs. In Milagro, analog digital converters (ADCs) are not used to record the signal pulse and instead, the pulse height and timing are determined by measuring the width of the pulse with Time Digital Converters (TDCs). This is called the time-over-threshold (TOT) method. The TDCs mark each time that a pulse crosses a voltage threshold with a change in the output voltage, or edge. The time resolution is 0.5 ns and is counted preceding a common stop for a triggered event. The edges are converted into the time in counts spent above the threshold, or TOT, which is correlated to the pulse amplitude. The earliest edge measures the starting time of the pulse, known as TStart.

The TOT is recorded for two voltage thresholds at ∼1/4 PE and ∼5 PEs. The use of two thresholds provides better sampling for small and large pulses. The higher threshold is set above the level of noise in the signals. The TOT for the low threshold is referred to as Lo TOT and the high threshold TOT as Hi TOT. To associate the TOT values with the start time and PE value of a PMT pulse, the TOT is calibrated using a laser. The apparatus used for the PE and timing calibrations and the method to determine the timing corrections are described in this chapter.

4.1 Laser Calibration System

The calibration system consists of a pulsed nitrogen laser (LSI VSL-337ND-S) and an optics system that transmits the laser beam to thirty locations in the pond and to each of the outrigger tanks (Figure 4.1). In addition to transmitting the laser beam to the PMTs, the calibration system includes a photodiode and electronics that generate a trigger for the DAQ and provide monitoring of the laser output. Each trigger generated by the laser is tagged as a calibration event, which signals the DAQ that the event should be stored separately from normally triggered events. This keeps calibration events out of the data used for scientific analysis and provides distinctive data files to be used for calibration analysis.

The laser beam first passes through a dye module which alters the wavelength of the beam to 500 nm. The beam is then split and sent to several components. Part

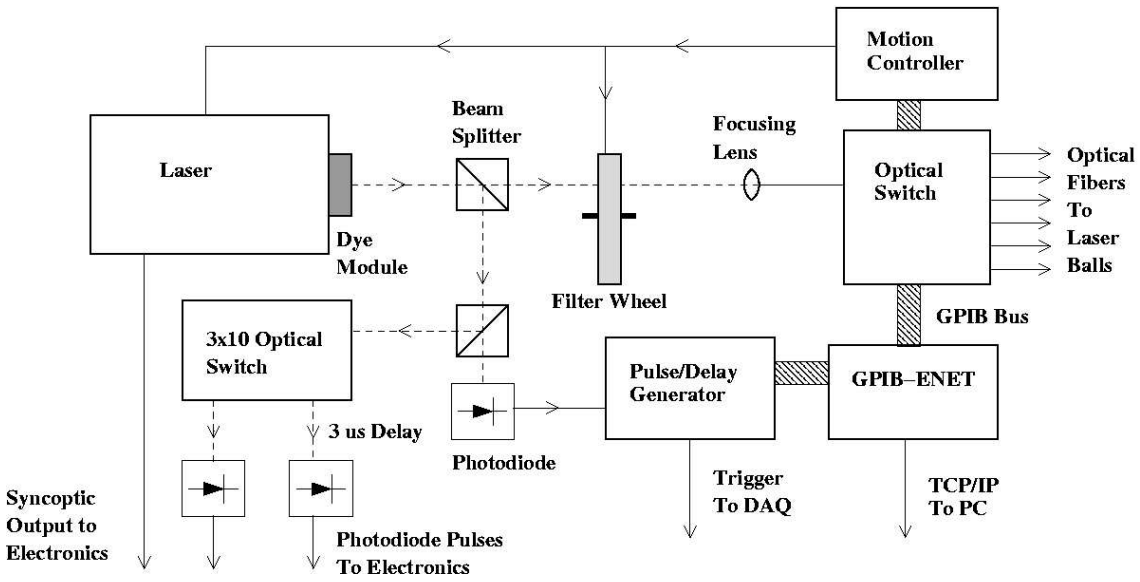

Figure 4.1: Diagram of optical system used to distribute light to PMTs for calibration.

of the beam is sent to filter wheel that is used to modulate the intensity of the light. Beyond the filter wheel, the laser beam is focused onto an optical fiber, which carries the light to a fiber-optic switch. The switch, controlled by software, routes the signal to one of the 30 fiber-optic cables connected to points in the pond or to additional optical switches and splitters connecting to the outrigger tanks.

The other original split of the laser beam is directed to a photodiode. The signal from the photodiode is sent to a discriminator, which is used to generate a trigger pulse for the DAQ. The discriminator threshold is set to eliminate spurious triggers from background noise. The output from the discriminator passes through a digital delay generator (Stanford Research DG535) before continuing to the electronics system. The laser beam passes through ∼300 ft of optical fiber before reaching the pond. The PMT signal cables are also around 300 ft in length. By the time a PMT signal generated by the laser pulse reaches the the TDC modules, the time window generated by the trigger has passed. The delay generator postpones the trigger signal to the DAQ until the PMT signal pulses can arrive within the trigger time window. This delay is typically 1 μs for pond PMTS but must be further increased for the outriggers, which have longer fibers and signal cables.

The effective intensity of the laser output is controlled using a neutral density filter wheel that varies continuously from full transparency to full opacity. A motion controller (Newport MM3000) rotates the filter wheel through a series of angular steps from a selected starting position. A step size of 10° provides reasonable sampling of pulse amplitude.

The calibration runs are controlled by a PC with a bridge to the GPIB bus. The rate of laser pulses, the laser ball selected to receive light, the filter wheel position, the appropriate monitor channel, and the trigger pulse delay are controlled by this system and can be adjusted to suit each calibration run. The software control allows

the calibration system, once started, to take data for each laser ball and filter wheel position without additional user intervention. The trigger delay and monitor channel adjustments necessary to receive data from the outriggers are set automatically in the software.

Additional outputs from the calibration system to TDC modules are used to monitor the timing and pulse amplitude of the laser. The laser sync-optic output and the output from a photodiode monitoring a split of the laser beam are sent to TDC channels. Both outputs generate a pulse each time the laser fires. Changes in the measured TOT or TStart of the monitor pulses indicate possible problems with the laser or calibration system electronics. The calibration system includes two monitors to allow for a delayed signal to be selected for outrigger calibration data. The outrigger fibers and signal cables are much longer than those in the pond (1000' vs 300') and a longer delay is required to insure that the monitor pulse falls within the time window containing the outrigger PMT signals. The photodiode signals provides a measure of any variation in the laser pulse amplitude to prevent errors in the calibration.

Using this system, the laser calibration data is taken simultaneously with normal data. The laser is typically pulsed at 10 Hz to limit pulse to pulse instability. The normal triggered event rate from air shower events is $\sim$1800 Hz. At $< 1\%$ of the event rate, the calibration events are recorded in addition to the normal trigger, while incurring only a slightly higher dead time for air shower events.

Before April 2001, calibration data was taken separately from the air shower data. Normal data runs were discontinued until the completion of the calibration runs. A full set of laser data for the pond PMTs takes from 12-30 hours depending on the number of laser pulses per wheel position and the number of filter wheel positions selected for use with each laser ball. The procedure has occasionally taken longer than that due to problems with the controlling hardware and software. The addition of a permanent calibration trigger input and the tagging of calibration events has enabled both triggers to operate together, eliminating down time due to laser calibrations and allowing more frequent calibration runs.

4.1.1 Lasers

Several lasers have been used to obtain calibration data sets (Laser Photonics LN120C, Laser Science, Inc. (LSI) VSL-337-ND-S and LSI VSL-337-ND, see Table 4.1). The most noticeable differences in data taken using the different models are due to the power output. Data sets taken with lower power lasers do not extend as far into the upper range of TOT although this can also be influenced by other factors in the optical setup. The laser used most recently, LSI VSL-337-ND-S has the advantage of higher average power and an output for monitoring the laser pulse amplitude and timing.

Model	Pulse Width (FWHM)	Pulse Energy	Average Power (at 20 Hz)
Laser Photonics LN120C	300 ps	70 μJ	1.2 mW
LSI VSL-337-ND	4 ns	120 μJ	2.4 mW
LSI VSL-337-ND-S	4 ns	300 μJ	6.0 mW

Table 4.1: Specifications for lasers used to obtain calibration data sets.

4.1.2 Laser Balls

The fiber ends in the pond, referred to as laser balls, are covered by a sphere of epoxy that acts as a diffuser. The laser balls are attached to PVC floats, which are secured in place by a Kevlar string attached to the PVC grid. There are thirty laser balls in the pond, spaced so that each PMT will see light from at least one and many see light from several (Figure 4.2). In this way the laser can be effectively fired from several positions to obtain multiple measurements of the time and pulse amplitude response of each PMT. The outriggers each have a single optical fiber mounted at the top of the tank. They each receive light from the laser individually and cannot be cross calibrated. The original surveyed positions for the pond laser balls and additional surveys appropriate for different epochs of the detector are given in Appendix A.

4.2 Slewing Corrections

The first stage of timing calibration determines the correction of the PMT signal arrival time for pulse amplitude. The start time should represent the beginning of the PMT pulse, the time the first photon interacted with the photocathode. The angle reconstruction does not define absolute time, but the relative time differences between signals from different PMTs must be measured accurately to get the best possible angular resolution. The TDCs mark time at fixed voltage crossings and do not account for different pulse widths. As the pulse amplitude increases, the TDC threshold is further from the peak. The shape of the pulse does not change with increased charge but the relationship between the start time of the pulse and the time that the pulse crosses the threshold does. A larger pulse crosses the TDC thresholds earlier relative to the beginning of the pulse than a small pulse beginning at the same time as illustrated in Figure 4.3. This effect, referred to as electronic slewing, is corrected by measuring the dependence of the pulse start time on TOT using laser generated events over a range of TOT.

To maintain independence of the PE and timing calibrations the electronic slewing correction is made as function of TOT without knowledge of the conversion to PEs. The advantage of this is that the slewing calibrations are not affected by errors in the calibration of PE level or subsequent changes in the PE calibrations. To measure the electronic slewing correction, the starting time in TDC counts (TStart) for low and high TDC thresholds is recorded for a range of TOT values.

TOT is measured in counts preceding a common stop initiated by the trigger. The conversion of an analog PMT pulse into TDC edges is illustrated in Figure 4.4.

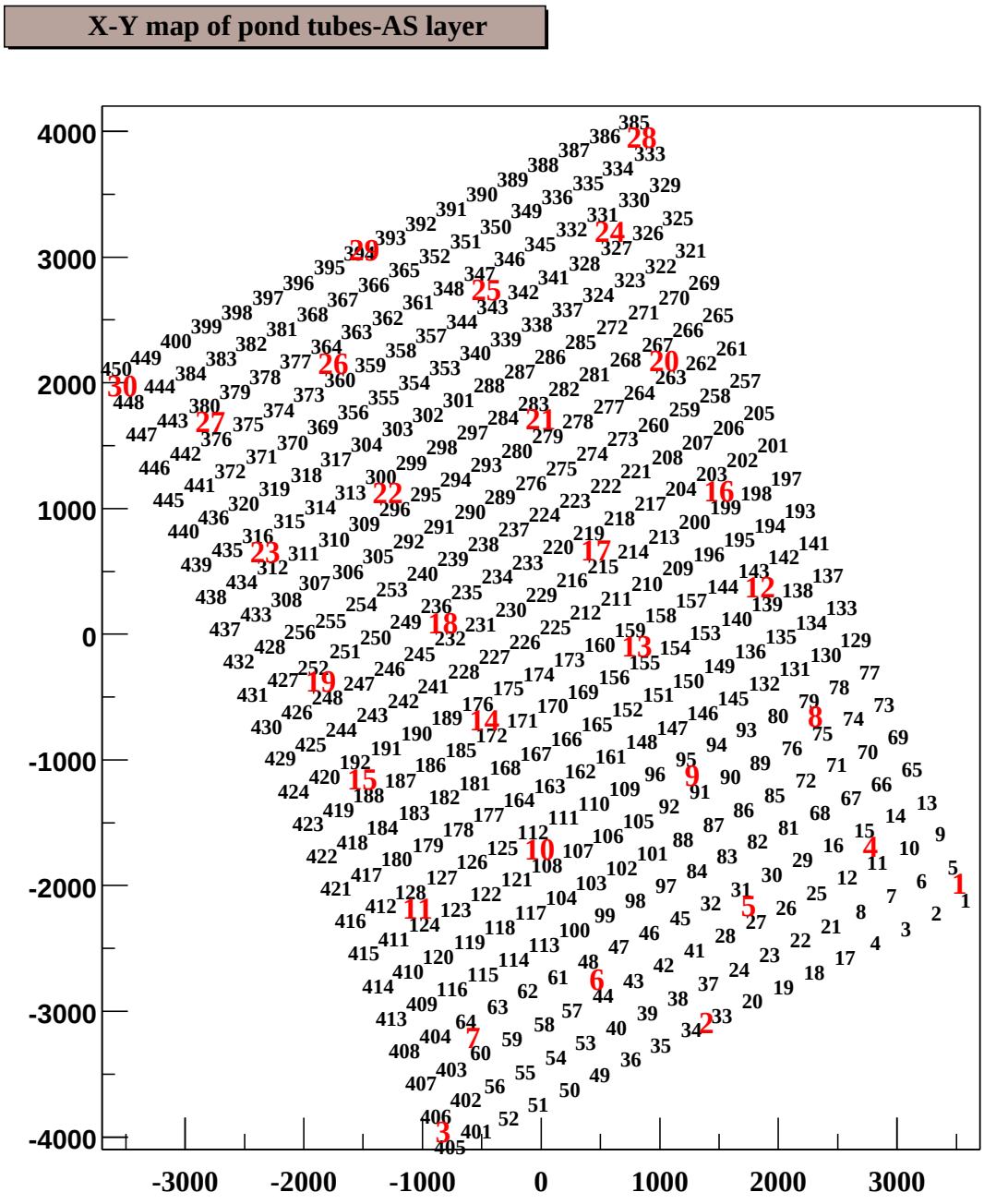

Figure 4.2: Location of laser balls (red numbers) in the pond. Black numbers indicate the locations of AS PMTs.

Counting backward causes larger TStart values to indicate earlier and not later times. The earlier arrival times for larger pulses translate into higher TStart values with increasing TOT. The shape of the TStart correction curve follows the relationship of the peak and the TDC threshold. Small pulses are sampled near the top of the pulse

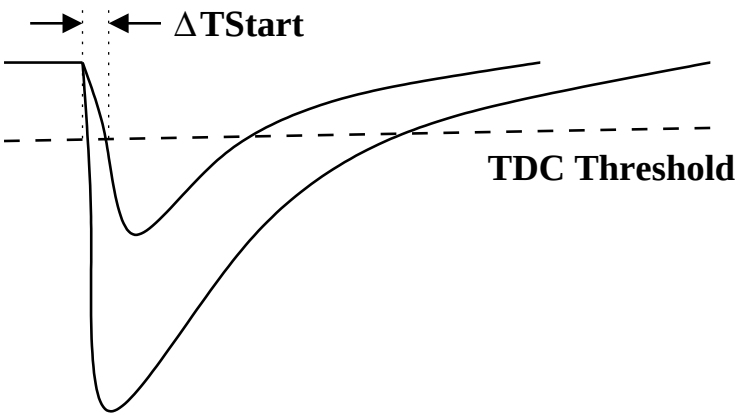

Figure 4.3: Illustration of electronic slewing effect. Both PMT pulses begin at the same time, but the time that they cross the TDC threshold depends on pulse amplitude.

where the width changes quickly with pulse height. As the pulse height increases beyond this, the peak is well above the threshold, and the relationship becomes approximately linear. The limiting value of TStart approaches a constant value as the pulse amplitude becomes very large. This behavior can be seen in the measured correction curves that are initially steep, turn over, and then flatten with increasing TOT (Figure 4.5).

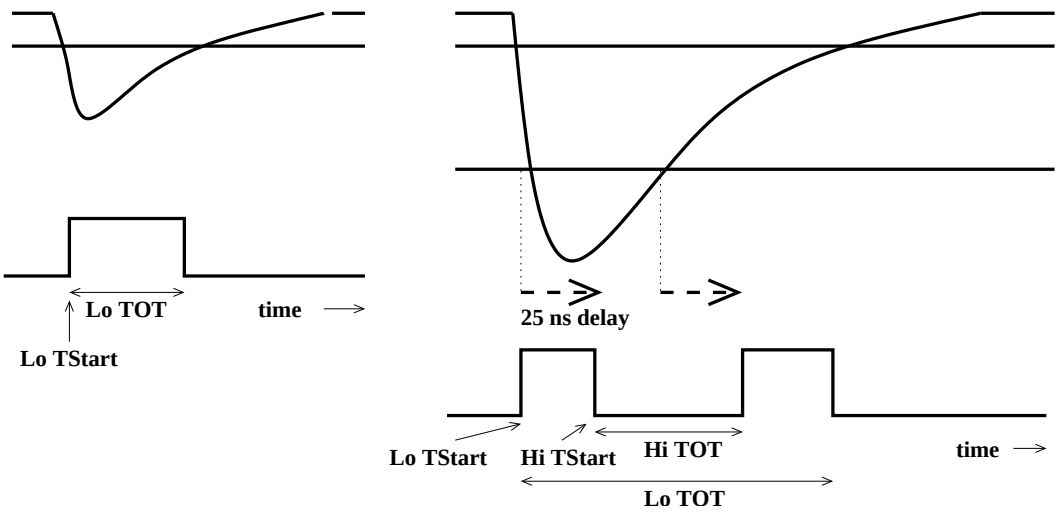

Figure 4.4: Illustration of conversion of pulse into TDC edges. Pulses are shown crossing low threshold only, a two-edge event, and high threshold, a four-edge event. Lo and Hi TStart are defined as the leading edges for low and high threshold. Lo and Hi TOT are defined as the differences in time of the low and high threshold edges respectively.

The variation of the filter wheel position provides TStart data points over a range of TOT similar to the typical range of photon energies for events in the pond. To put this into perspective, a 1 PE pulse in a typical Milagro PMT corresponds to around

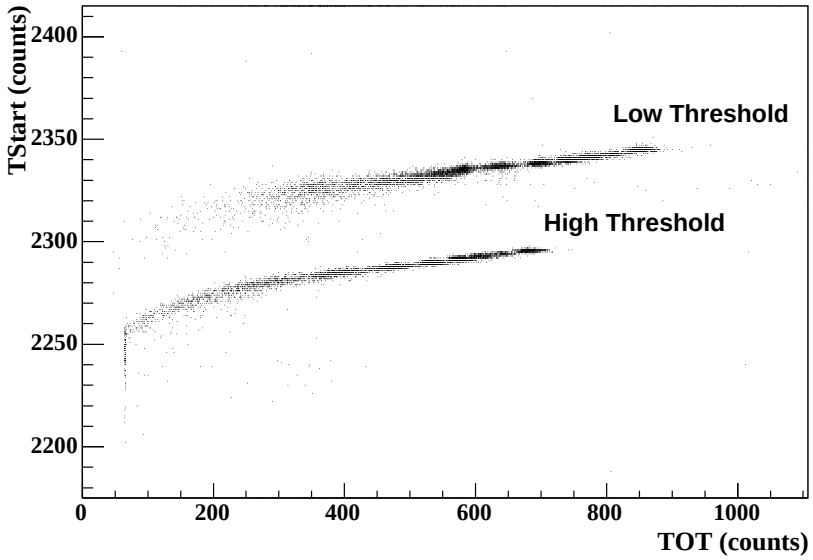

Figure 4.5: TStart as a function of Hi and Lo TOT from laser data. The upper (earlier) curve is for the low TDC threshold and the lower (later) curve is for the high TDC threshold. The reversed time dependence of TStart comes from the TDC modules counting backward from a common stop.

300 Lo TOT counts; a 1000 PE pulse corresponds to 600-700 Hi TOT counts.

The laser generated time measurements are a subtractive correction, which produces a flat dependence of start time on TOT for each PMT. The correction curve is given a functional form and fit for each PMT for both TDC thresholds. For purposes of fitting this curve, several things are noted. First, the two thresholds are sampling different portions of the same pulse implying that the measured curves for high threshold are offsets of the low threshold curves. Second, the slewing curves for all the PMTs are very similar. A study of the global properties of the combined slewing curves reveals a single shape that can be applied as the fitting function for both thresholds. The parameters of that shape do not vary substantially from PMT to PMT (Figure 4.6).

A study of the AS PMTs shows that to a good approximation the slewing curves are linear with a break at some characteristic TOT for each threshold and PMT. An examination of the slopes of linear fits above the typical break TOT for the high TOT curves shows that the slopes are very similar from PMT to PMT. Likewise, the slopes above the typical low TOT break are similar for all the AS PMTs. Below the typical break for both TOT thresholds, the data are poor with large errors because these values of TOT are below 1 PE. Although this region has some curvature, the quality of the data is poor and fits reasonably well to a line.

The linear fits to the slewing curve below and above the TOT break can be combined smoothly to form a continuous function that is simple, well-behaved, and

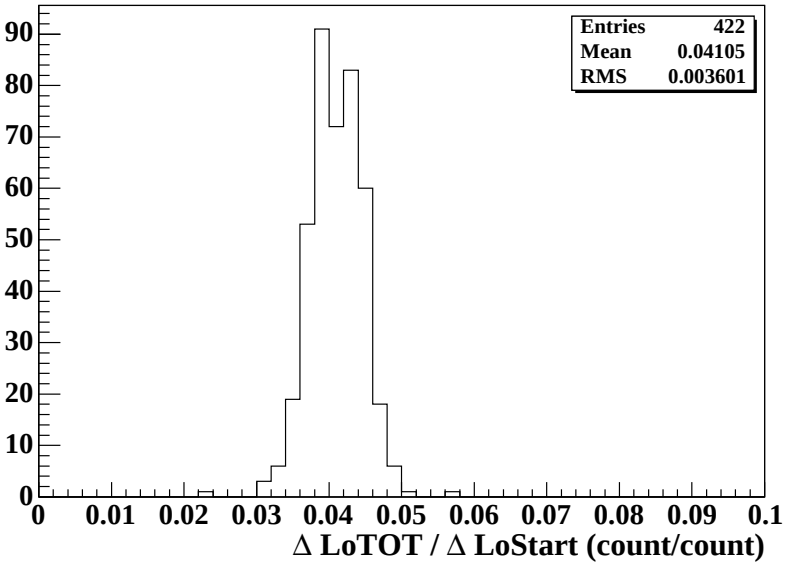

Figure 4.6: The results of fitting a line to slewing curves above 300 Lo TOT. The slope of the Lo TStart, Lo TOT data is shown for all AS PMTs with data. The distribution sets the range for a_1 and demonstrates the global similarities of the PMTs.

well constrained by the global properties of the slewing curves.

$$TStart = (a_0 + a_1 * TOT) * expFall + (b_0 + b_1 * TOT) * expRise \tag{4.1}$$

where

$$expFall = \frac{e^{-(TOT-c_0)/c_1}}{1 + e^{-(TOT-c_0)/c_1}}$$

and

$$expRise = \frac{e^{(TOT-c_0)/c_1}}{1 + e^{(TOT-c_0)/c_1}}$$

This function produces a generally reliable fit with parameters that can be tested for divergence from acceptable values. The parameters a_0 and b_0 are TStart offsets that should be close in value and close to the overall TStart level. The values of these parameters will be shifted ∼25 counts from low to high threshold due to a built in delay between the thresholds. [1] The parameters a_1 and b_1 are slopes below and above the TOT break which is represented by c_0. The parameter c_1 controls the rate of rise or fall of the exponentials. Because these parameters relate closely to properties of the slewing curve, it is possible to constrain them to be in sensible value ranges and to define a quality of fit that can be used to select the best slewing curve of several for each PMT and threshold.

[1] The delay is necessary to resolve the TDC edges from the high and low thresholds. The effect of this delay is removed naturally from the TStart value by the timing correction.

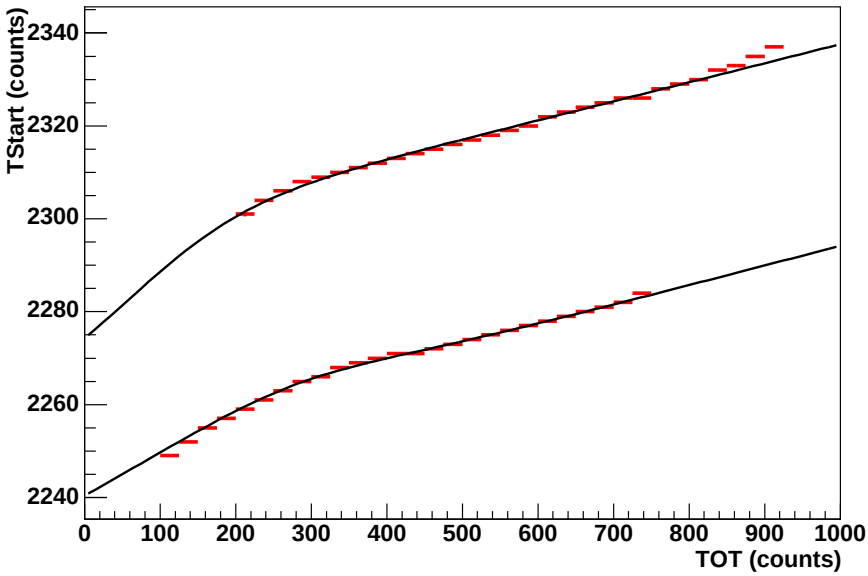

Figure 4.7: Fits of slewing curves to laser data for an AS PMT. The upper curve is for low threshold and the lower curve is for high threshold. The horizontal bars are the fits to the TStart distribution in 25 count wide strips of TOT. The error bars in the TStart fits are too small to appear. The black line is the slewing correction, the result of the six parameter fitting function, Equation 4.1 the TStart data points.

The redundant coverage of the laser balls provides several slewing curve fits for each PMT. The best fit for each PMT, either that with the broadest range in TOT or the least error in the fit, is selected to be used for the slewing correction. The best fits for a PMT for both Hi and Lo TStart are required to be from the same laser ball to simplify the time offset calibration. The goal of the slewing calibration is to remove the TOT dependence of TStart for each PMT. To see if this is the result, the slewing distributions for standard air shower data are examined after applying the calibration. The corrected TStart values do become flat in TOT as shown in Figure 4.8. Ultimately, The angle reconstruction depends on the calibrated TStart and PE values. A more stringent check is that the TStart distribution is flat in PEs instead of TOT, although that depends on the PE calibration as well (Figure 4.9).

A few PMTs used in Milagro have a flaw that allows a photoelectron to miss the first dynode and progress through the PMT ahead of the rest of the charge in the signal. This results in a small early bump preceding the main PMT pulse that causes an artificially early TStart time if it crosses the TDC threshold. This effect is only observed for large pulses in a few PMTs. The bump is large enough to cross the low TOT threshold, but not the high TOT threshold. Thus, the effect can be excluded by using the high TOT calibration instead of the low TOT calibration for levels of low TOT where the effect can occur. The prepulsing causes upward curvature in TStart that can skew the slewing fit. To prevent prepulsing from adversely effecting the slewing fit, the low slewing curves are fit using data points below 600 LoTOT. When the fits are applied to data only the high slewing correction is used for PMT

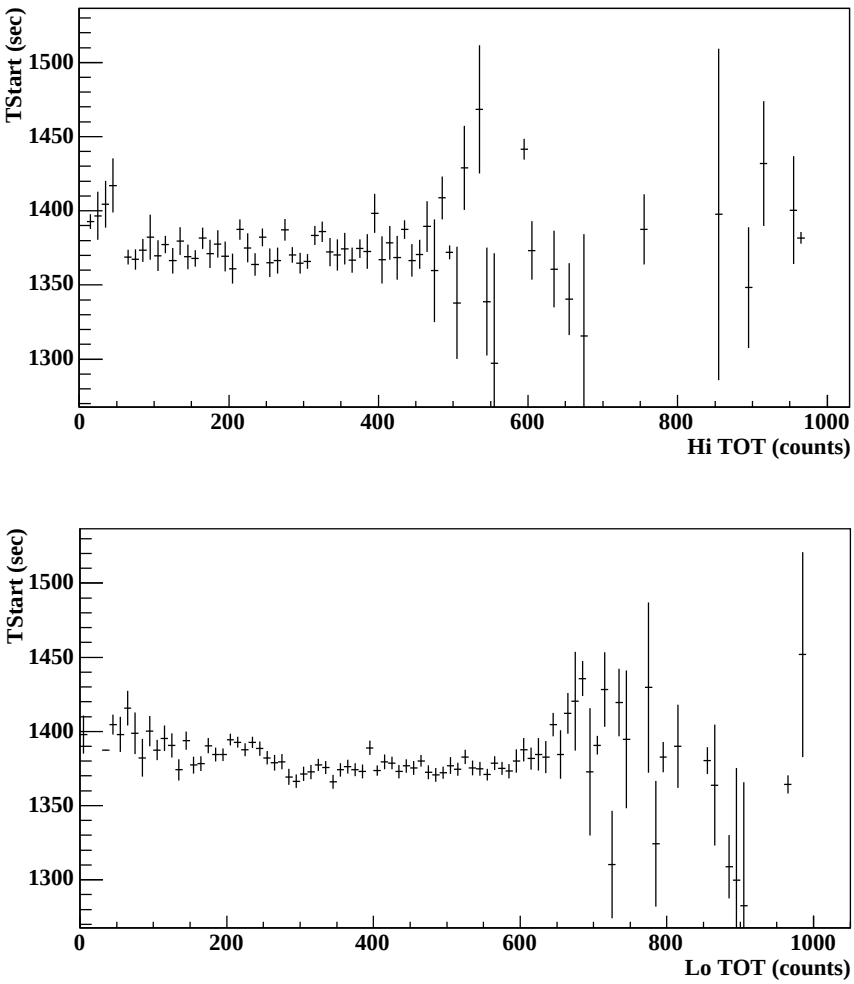

Figure 4.8: Calibrated TStart as a function of Hi and Lo TOT for an AS PMT. The calibrated time has the slewing correction and, thus, the pulse amplitude dependence removed. The times for both the high and low thresholds also appear at the same level in TStart.

hits with Hi TOT>300 counts. This cut simultaneously avoids the region of low slewing susceptible to prepulsing and the region of high slewing with larger errors in the calibration data.

4.3 Time Offsets

In addition to correcting the start time of the PMT pulse for the pulse height, the time must be corrected for differences in travel time through the electronics for each PMT. An initial time offset for each PMT and TDC threshold is arbitrarily defined using the TStart value of the slewing fit at 400 TOT counts. This value includes time differences that are artifacts of the calibration. The corrections are determined by

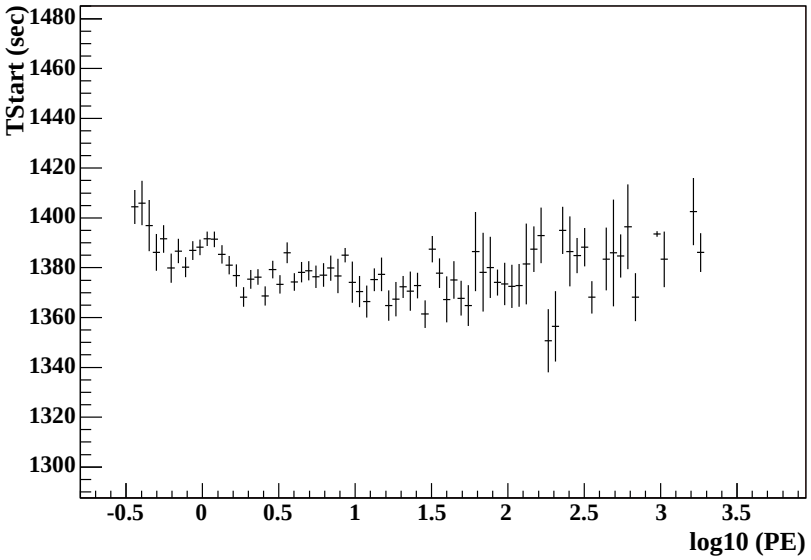

Figure 4.9: Calibrated TStart as a function of PEs. The statistics are poor at very high and very low PE values.

using the relative differences in PMT signal arrival times from the laser calibration data. The corrected time offset when applied to the start time of a PMT pulse in an air shower event returns a time that can be compared with those of the other PMTs to establish the plane of the shower front.

The PMT time offsets from the laser calibration data include three contributions.

$$TStart = t_{Fiber} + t_{Water} + t_{Electronics}$$

The quantity, t_{Water}, is the time of travel from the laser ball to the PMT. This is calculated using the surveyed positions of the PMT and laser ball and the phase velocity for 500 nm light in water, calculated to be 22.04 cm/ns (see Fleysher et al. (1997b) for details). The travel time of the laser pulse from the laser to the laser ball, t_{Fiber}, is measured using the calibration data. Once t_{Fiber} is determined, the travel time of the signal from a PMT to the TDC modules, $t_{Electronics}$, can be calculated.

The time difference between the slewing corrected TStart value, TSlew, and the uncorrected TStart for a single PMT laser event is

$$TStart - TSlew = \Delta t_{Fiber} + \Delta t_{Water} \tag{4.2}$$

where Δt_{Fiber} is due to a difference in length of two fibers and Δt_{Water} is due to a difference in distance between two laser balls and a PMT. The calculated t_{Water} is removed from TStart and TSlew for each event using the PMT and laser ball locations. This allows a measurement of Δt_{Fiber}, the unknown correction required for the time offsets.

$$\Delta t_{Fiber} = (TStart - t_{Water}(PMT, LB)) - (T_{Slew} - t_{Water}(PMT, LB_{Slew}))$$

Each PMT has calibration events from multiple laser balls. The Δt_{Fiber} for data from the laser ball used to make the slewing calibration should be zero within the spread of the TStart data points. Data from different laser balls for the same PMT provide a measurement of the difference of Δt_{Fiber} from zero for the fiber of interest and the fiber used for the slewing calibration.

Using the whole calibration data set, each PMT gives a measure of Δt_{Fiber} for several fibers relative to the fiber used in the slewing calibration for that PMT. The difference of Δt_{Fiber} for data taken with two different fibers gives the relative difference independently of the fiber used in the slewing calibration,

$$\Delta t_{Fiber}(AB) = \Delta t_{FiberA} - \Delta t_{FiberB}$$

The measurements of Δt_{Fiber} can be made for many pairs of fibers and are over constrained. The linear system of the pairwise differences can be solved for the difference for each fiber length relative to one selected fiber. The accuracy for each measurement is judged by the width of the distribution for Δt_{Fiber} (Figure 4.10). A Gaussian fit determines the peak position and RMS for the distribution. Only distributions with well-fit, narrow peaks are included in the linear system of fiber length differences.

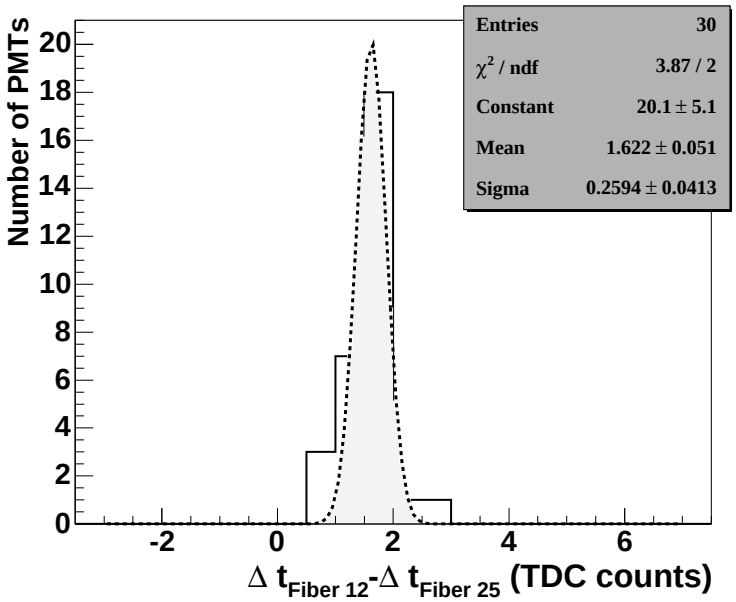

Figure 4.10: Δt_{Fiber} for PMTs receiving light from laser balls 12 and 25. Thirty PMTs pass the cuts to be included in the distribution for the data set examined. A Gaussian fit is used to define the peak and judge the quality of the data.

Once the relative Δt_{Fiber} is measured for each fiber used in the calibration, the timing offsets can be corrected for all PMT dependent differences. No absolute values need to be determined because the angle fitting depends only on the relative times that the PMTs are hit. The offsets for each PMT and threshold are corrected by

removing the t_{Water} and Δt_{Fiber} values appropriate for the laser ball used in the slewing calibration.

$$TOffset = TStart - t_{Water} - \Delta_{Fiber}$$

where TStart is as defined in Equation 4.2. The remaining differences in the time offsets from PMT to PMT are caused by variations in travel time through the individual electronic channels from the PMTs to the TDC modules.

When $TOffset$ is subtracted from the TStart value recorded by the TDCs for each PMT pulse, the timing differences in individual electronic channels are removed, leaving the calibrated TStart value:

$$TStart_{Cal} = TStart_{Data} - TOffset - TSlew(TOT).$$

After subtracting the slewing correction and the time offset, the time calibration is completed by multiplying the calibrated TStart value by a factor of two to convert from counts to ns.

Further descriptions of the time offset calibration method can be found in Fleysher et al. (1997a,b).

4.3.1 Evaluation of Time Offset Accuracy

Accurate measurements of the time offsets are necessary to achieve the best angular resolution with the angle reconstruction. The method used to determine the time offsets has very low error in the fits, but is susceptible to systematic effects. Some systematics are caused by the hardware problems discussed and can be corrected, while others remain to be determined with future calibration data sets. The presence of remaining systematic effects is inferred by examining the data.

The high event rate in Milagro allows tests with low statistical error. The angle reconstruction applies a chi-squared fit of the PMT times to a plane. The time residuals from this fit for a PMT over a large sample of data events expose systematic problems with the time offsets. A non-zero mean for the time residual distribution for a PMT indicates times that are typically early or late compared to the reconstructed shower front. The calibrated time offsets are adjusted once by the difference of the mean of the timing residuals from zero. This improves the angle reconstruction by reducing DelEO, which is the reconstructed angle difference from using only even and only odd numbered PMTs, and by increasing the number of PMTs included in the angle fit. Additional iterations of this adjustment do not show as much improvement and carry the risk of introducing a systematic effect in the reconstructed direction.

The pointing accuracy can be tested by fitting a plane to the time offset values. This assumes that for the whole pond, the plane normal should point up. The time offsets have a dependence on the voltage used with the PMT. The PMT voltages are set by 16 channel patches and are correlated in position. It is not clear that perfectly calibrated time offsets would produce a plane with the normal pointing directly up. The voltage levels are not changed over time, however, making comparisons between different time offset calibrations possible.

The pointing accuracy can be tested by examining the distribution of reconstructed shower directions. To first order the mean of the reconstructed direction distributions should be at zenith. The majority of reconstructed events are from cosmic-ray nuclei. This makes the method dependent on the distribution cosmic-rays being isotropic in the sky. Additionally, it would be more ideal to optimize the calibration to gamma-ray events instead of the cosmic-ray background.

Ultimately, the accuracy of the timing calibrations can best be evaluated using a gamma-ray point source. The gamma-ray point sources detected by Milagro, the Crab Nebula and MRK 421, provide a test of the pointing accuracy. The difference between the observed and known locations of the sources for several detector epochs has suggested the presence of pointing systematics. The application of angle corrections based on the distribution of reconstructed shower directions improves the observed locations substantially. More improvement may be possible, particularly if the systematics can be eliminated at the calibration level.

4.4 Hardware Issues

Several hardware issues have been discovered in the calibration system. Most of the issues have been resolved. Unfortunately, calibration data that accurately represents a specific configuration epoch of the detector cannot be retaken after changes have been made to the detector configuration. The problems are described in general here. The specific corrections that need to be applied to the existing calibration data sets are described in detail in Appendix A.

4.4.1 Time Delay Shifts

The digital delay generator, which sends a signal used to trigger the DAQ, has shown some variation in the time delay. A variation in the timing of the trigger pulse causes a systematic shift in the start times used for calibration. The shifts are typically discrete jumps of 8-10 ns although some data show continuous variation that cannot be accurately measured. In the data, the time shifts are evident when TStart is plotted against time as in Figure 4.11. In the slewing plots, TStart against TOT, the effect is a doubling of the slewing curve which causes an unreasonable and unreliable slewing fit (Figure 4.11).

The effect can be corrected for data in which the time shifts are discrete and infrequent. The amount of the shift is simply removed from the data over the time it occurred. A correction is necessary for most of the calibration data sets taken before the effect was understood and the delay generator repaired (August 2003).

The offset in TStart is measured relative to preceding and following TStart values for data with clean, discrete shifts. The assumption is that for a single wheel position the mean of the TStart value should be constant.The error in the correction is similar to the resolution of the TStart fits and does not effect the accuracy of the slewing fits. The values used for TStart shift corrections in the existing data sets are available in Appendix A. Data with uncorrectable TStart values are excluded from

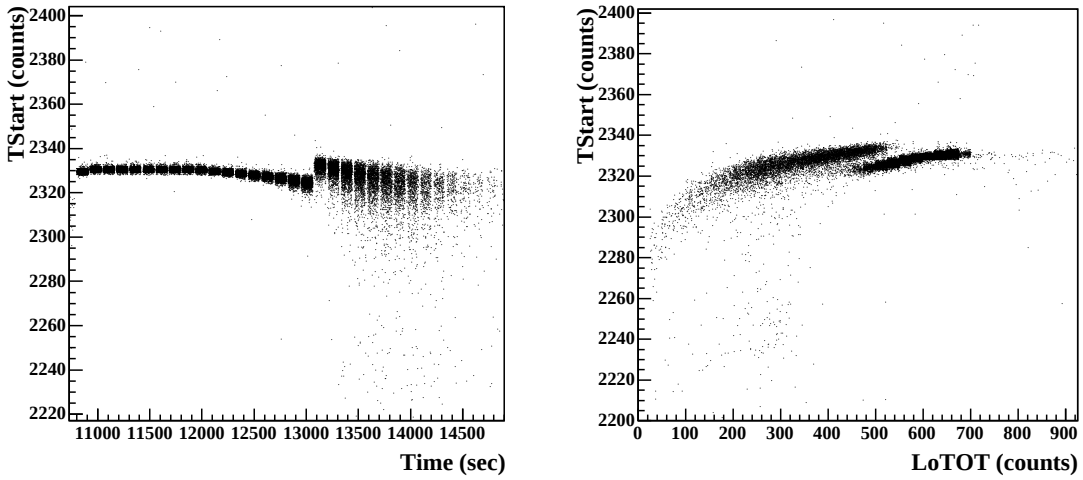

Figure 4.11: Example of a shift in time delay from the delay generator. The abrupt shift in TStart in the time plot (left) should not occur and causes a discontinuity in the slewing curve (right).

the calibration.

Nothing can be said about time shifts that may occur during gaps in the calibration data between laser ball runs. Fortunately, any global time shifts from laser ball to laser ball are removed automatically by the time offset calibration as long as the shifts are discrete and not gradual over long periods of time. Discrete time shifts between laser balls have probably occurred in several data sets. The disparities in the relative fiber length time differences from data set to data set would be explained by arbitrary shifts in the trigger time. A gradual effect could cause systematic errors in the timing calibration. The recently installed monitoring of the laser output provides a way to insure that there is no gradual drift in the trigger delay time.

4.4.2 Laser Ball Position Changes

The laser ball floats are at the pond surface and become encased in ice that forms at the top of the pond during cold weather. In the last several years the expansion of the ice has pulled some of the floats free from their moorings. The position of the laser balls is a necessary parameter used to determine the time offsets as described earlier. If a laser ball is displaced from the surveyed position, the coordinates must be determined by other means.

An error in the position for a laser ball causes Δt_{Water} to be calculated as too short for some PMTs and too long for others. This causes the distribution of the difference of Δt's for a laser ball pair to broaden. The time offset calibration excludes this distribution when the RMS is large. When the distribution for all pairs involving a particular laser ball are large, the standard calibration returns no $\Delta tFiber$ for that laser ball. The true position can be fit using the calibration data by finding the laser ball position that minimizes the width of the difference of Δt distributions for several

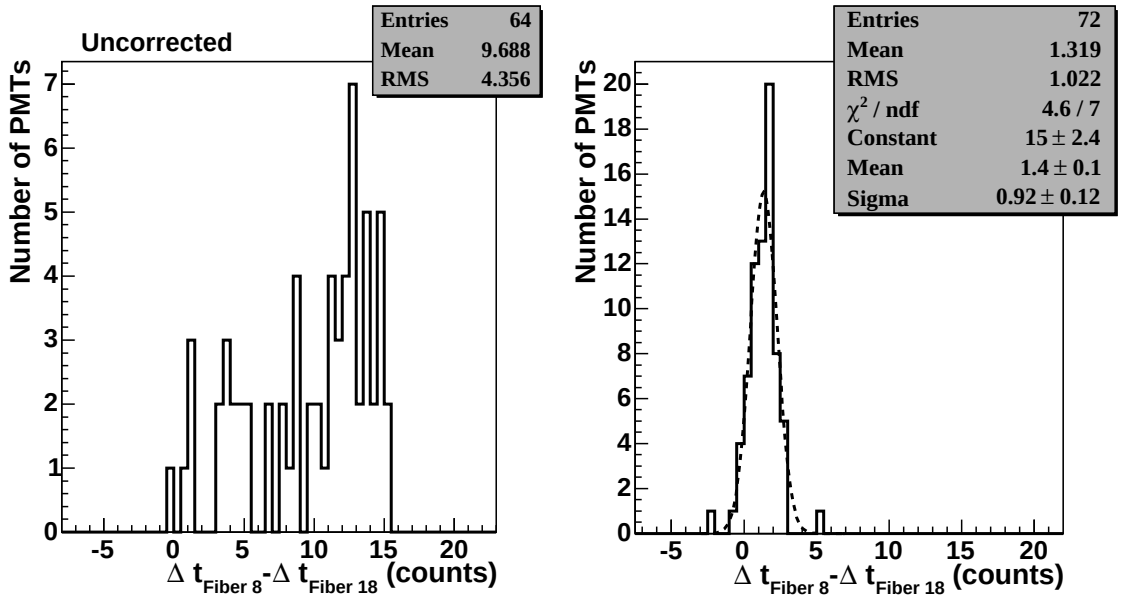

Figure 4.12: Distribution of Δt_{Fiber} differences for laser balls 8 and 18 before and after correcting the position of laser ball 18 in calibration data taken in November, 2001. The corrected distribution lists the parameters for a Gaussian fit.

laser ball pairs that include the loose one. The distribution for a pair including a loose laser ball shows significant improvement after fitting for the unknown location (Figure 4.12). Tests of this method on laser balls with known positions show the location is determined to within 30 cm.

The position can be corrected as long as the laser ball stays stationary during the calibration period. A better solution is to reconnect the laser balls to their surveyed positions. The 2002 and 2003 repair operations included a visual inspection of each laser ball float. Those found to be dislocated (eight laser balls in 2002, one in 2003) were attached to the appropriate grid locations with the assistance of divers. One fiber optic cable was found to be disconnected from its PVC float and had to be retrieved and secured to the float again. Following the realization that some laser balls may be out of position, each calibration data set has been checked for a correlation of the PMT receiving the most light and the surveyed laser ball position.

The dependence of the time offsets on knowledge of the laser ball positions makes the slack in the some of the strings attaching the laser ball floats to the grid a concern. The laser balls were designed to be held stationary just below the surface of the water. The current water level is a few inches below the original level due the loss of water out of a drain due to weight on the cover from snow and rain. Now many float at the surface instead of below and a few have noticeable freedom of movement. This introduces an additional error into the time offset calibration.

Systematics in the timing calibrations have not been carefully studied given the variety of changes made to the laser system over the past few years and the lack of comparable data sets. Now that the system is stabilizing into a more optimal and reliable configuration, a study of stability and errors could be considered. Compar-

isons could be made in the future of the PMT slewing parameters from different calibration versions, particularly, of several versions for the same detector epoch. A comparison of the relative fiber differences would give an indication of stability in the time offset calibration.

Chapter 5

Reconstructed Data Analysis

Data that has been processed online (Chapter 3) is later used to create event maps of the sky and expected background. These maps are used to evaluate event excesses at locations in the sky. If the excesses are significant, the event rate is converted to a photon flux. In the absence of a significant detection, the event rate is used to set an upper limit on the photon flux. To obtain the sky maps, the reconstructed data is subjected to a series of filters, corrections, and cuts in order to remove problematic data and enhance gamma-ray signals (see Figure 5.1). Events passing the quality filters are subjected to several calibration corrections and a cut to remove poorly fit events. The selected events must then pass a gamma-hadron separation cut to be included in the signal map and estimation of the background. The resulting maps must also pass a length cut to be included in the final analysis.

The background estimation described here is optimized for detecting long ($\geq$2 hour) time scale emission from point sources. Most of the filters and cuts are applied to both the real-time transient search, an analysis conducted immediately following online data processing (see Chapter 7), and the analysis used to search for selected AGN (see Chapter 8). The gamma-hadron separation cut and the background estimation method apply to both analysis methods, and are used generally with Milagro data. The real-time search accepts some data and maps that may be excluded from the AGN analysis due to later data filtering. Several cuts, which are noted, cannot be applied online and are used only with archived data. Data filtering at the run and map levels is specific to the analysis of selected AGN presented here.

5.1 Refinement of Reconstructed Data

5.1.1 Event Filters

Over the history of data acquisition in Milagro, there have been a variety of hardware, software, and data archiving issues that have been identified. Data taken before solutions were available benefits from the application of some simple filters at the event level. Some of data errors relate to reading the GPS clock out to the VME memory module (see Chapter 3 for specifics of the data acquisition system), which is used to determine the recorded event time. Several time anomalies have been observed in the event data. For example, large time gaps between events, non-physical ordering of

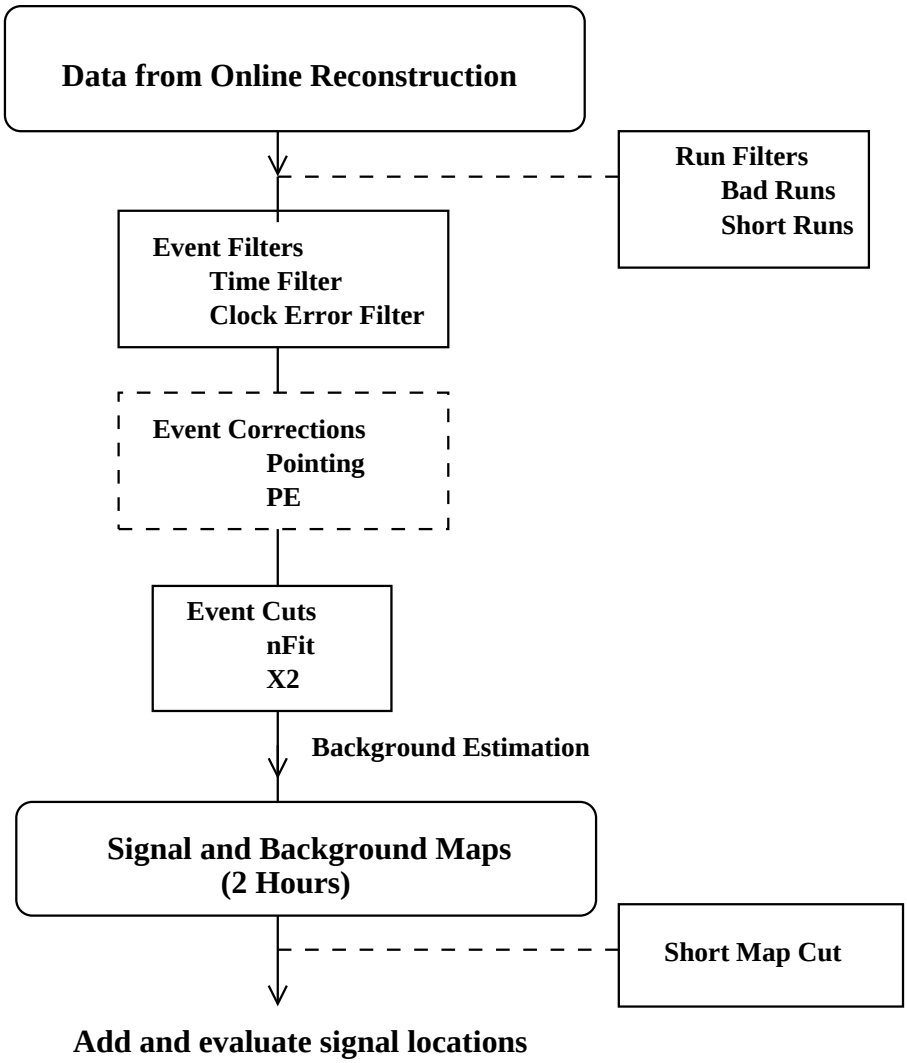

Figure 5.1: The data analysis process from the reconstructed data to signal and background measurements that can be evaluated for significance and flux from a source. The steps marked with dotted lines are not included in all analysis or are only relevant for certain periods of the data.

event times, and multiply repeated event times have been observed. These problems are rare, but time errors cause significant difficulties for the analysis of the data. A time filter is applied to events to check the value, order, and spacing of event times for reasonable behavior before the signal and background maps are generated. Those events not passing the filter are excluded from any further analysis.

The accuracy of the GPS clock depends on the antenna receiving a single from enough GPS satellites to get a good position localization. If less than four satellites are in view, the time reported by the GPS clock is advanced internally and gradually drifts away from an accurate value. A drift in event times causes an offset in the reconstructed event directions. The time error reported by the GPS clock is used to exclude events with a large enough drift to adversely affect analysis results. It

takes a significant loss of contact to cause a noticeable impact on Milagro data. The time error must be on the order of the angular resolution, $\sim 0.75^{\circ}$, to degrade a signal. The time error required to affect the angular reconstruction at this level is approximately three minutes. The error in the GPS time very rarely exceeds more than a 100 μs. Nevertheless, the accuracy is monitored in the analysis routines, and events are excluded if the error exceeds 1 ms. This cut excludes very little data, but prevents data with large reconstruction inaccuracies from being included in analysis.

5.1.2 Pointing Correction

Systematic errors in the timing calibration can lead to positional inaccuracies in the data. There are methods available that use existing data to evaluate and improve the pointing. The number of events recorded by Milagro is large and offers much higher statistics than available to the calibration method. Although the vast majority of recorded events are initiated by hadronic cosmic-ray particles and not gamma rays, they can be used to determine the pointing of the detector.

The cosmic-ray background can be used to determine pointing by examining the direction from which the most events come. Following the assumptions that the cosmic-ray background is uniform and that the efficiency of detecting events with Milagro depends chiefly on the thickness of the atmosphere, the distribution of events should peak directly overhead. Measurements of this peak for different epochs of calibrations and detector configurations show a divergence from overhead. The displacement is measured and removed from the reconstructed angles for the relevant epochs. The significance at the positions of detected sources, the Crab Nebula and Mrk 421, shows improvement when this pointing correction is applied (Figures 5.2).

5.1.3 PE Calibration Correction

A specific correction to the calibrated photoelectron (PE) values is made for data taken between December 2002 and May 2003. The correction is necessary to properly apply the background rejection parameter. A hardware problem led to an incorrect calibration of the filter wheel positions used for laser data taken after the repair in September 2002. Each filter wheel position is associated with a light level to judge the number of PEs corresponding to the time over threshold (TOT) levels in each PMT. The actual filter wheel position was offset from the recorded position causing a systematic shift in light level for each filter wheel position. The filter wheel attenuation varies logarithmically, which caused the PE calibration to become increasingly shifted from the proper value at larger TOT values. The major effect was an error in calculating the gamma-hadron separation parameter, X2, which depends on the maximum PE value recorded for a bottom layer PMT. The error in X2 caused a loss in signal sensitivity, which is explained in greater detail in the section on errors in the flux calculation. The reconstructed data cannot be calibrated again for this time period, but it can be corrected by rescaling the calibrated PE values to a level that reproduces the appropriate X2 distribution and rate of events passing the X2 cut. After rescaling, the application of the gamma-hadron separation parameter

reproduces the expected significance at the location of the Crab Nebula.

The PE and pointing corrections are applied to the data used in the AGN search. The online search, however, only includes the PE correction for data that were analyzed a second time to recreate the maps for periods I,II, III, and the full data set (See Chapter 7). Maps made for shorter timescales, one month and shorter, represent the original online reconstruction and do not include the PE correction or the pointing correction before May 2003. After May 2003, the PE and pointing corrections are included in the online reconstruction as part of the calibration.

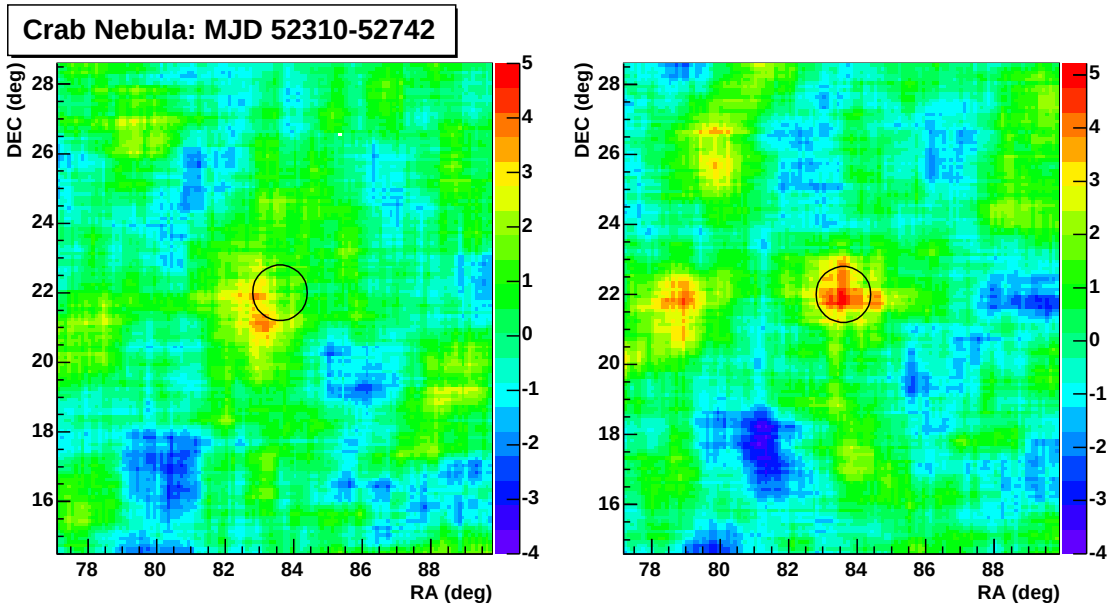

Figure 5.2: The significance map for the region containing the Crab Nebula is shown. The black circles are centered on the expected position. The figure on the left is the result of analysis without the pointing or PE calibration corrections. The figure on the right includes both corrections and demonstrates the improvement in significance and location.

5.2 Analysis Cuts

Several cuts are made on events included in the signal and background estimation maps to improve the quality of the data and enhance a gamma-ray signal. Ground-based observations are heavily dominated by the cosmic-ray background. Parameters that exclude unusable background events and bias the analysis to gamma-ray-induced air showers are vital to the detection of a signal.

5.2.1 Reconstructed Direction

The angle reconstruction for an event is assessed in two ways. First, the event must have a reconstructed angle. Some events receive non-physical directions. These are

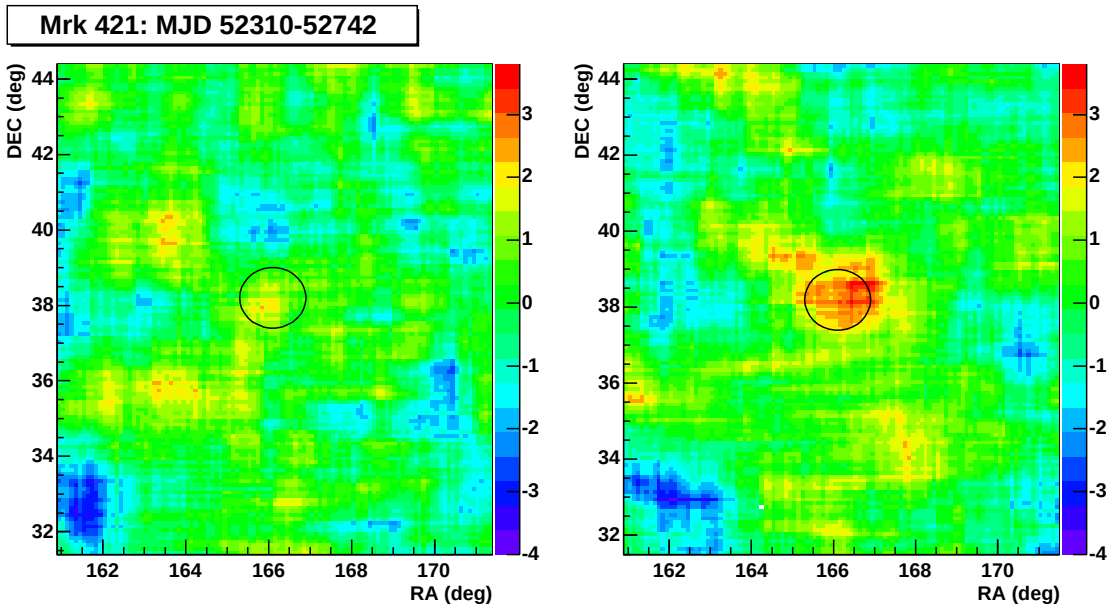

Figure 5.3: The significance map for the region containing the AGN Markarian 421 (Mrk 421) is shown. The black circles are centered on the expected position. The figure on the left is the result of analysis without the pointing or PE calibration corrections. The figure on the right includes both corrections and demonstrates the improvement in significance and location.

either cases where the angle fitter finds a fit to times from PMTs not associated with the air shower, only fits part of a shower, or attempts to reconstruct light from a single muon arriving at a large zenith angle. All events failing to receive a direction are excluded. Second, there must be enough PMT times used in the angle reconstruction (nFit) to produce a reliable direction. At the extreme minimum, there must be enough PMT times included in the angle fit to constrain a plane. The accuracy of the angle fitter can be tested in simulations. The simulated reconstruction of gamma-ray-induced air showers shows that the error in direction becomes large for fits using less than 20 PMTs. To exclude these high error events, a cut is made requiring nFit>20.

5.2.2 Gamma-Hadron Separation

The cosmic-ray background, as previously mentioned, is very large in comparison to gamma-ray signals. The background must be reduced to allow the detection of a signal. The background events in Milagro can be removed using the different properties of gamma-ray-induced and proton-induced air showers. The heavier particles, pions and muons, that form in proton-induced showers cause a nonuniform distribution of energy in the detector. The more massive particles penetrate more deeply into water than the electrons, positrons, and secondary photons in gamma-ray-induced showers. In the deeper bottom layer of PMTs (MU layer), the heavier penetrating particles are

noticeable. The energy distribution appears in Monte Carlo simulated events as clusters of large PE values for proton-induced showers, but as more smoothly distributed PE values for gamma-ray induced showers. The gamma-ray-induced showers show a much higher correlation of PEs among the MU layer PMTs.

The difference in the energy distribution can be parameterized based on a ratio. The highest PE value for a MU layer PMT in an event is large for events with penetrating particles. Events that are gamma-like with a smoother distribution of PEs across the pond will have a number of weak hits and a low maximum PE value. A parameter is defined based on the number of MU PMTs with PE values >2 and the maximum PE value for any PMT in the MU layer.

$$X2 = \frac{N_{MU}\ PMTS > 2PE}{Max\ MU\ PE}$$

It can be interpreted as an inverse-compactness cut. Gamma-like showers will have a higher ratio while proton-like showers will have a small ratio. The distribution of X2 for simulated protons and simulated gamma-rays is shown with the distribution from data in Figure 5.4. The discrepancy between the proton simulations and the data at large values of X2 is mostly due to the lack of higher mass cosmic rays than protons in the simulations. Helium, for example, produces more compact energy deposits in the MU layer. Requiring X2$\geq$2.5 optimizes the cut for a gamma-ray signal. Simulations show that the cut removes 90% of protons and keeps 50% of gamma-rays.

5.3 Run Exclusion

The archived set of reconstructed data includes some runs that have been taken under special conditions. Some of these were acquired using non-standard trigger levels to get a sample of events at low trigger levels, test the trigger card, or take ADC calibration data. Runs taken using special trigger conditions or that have noticeably different event rates are removed from the data set used for the AGN analysis. To calculate the flux from a source, assumptions must be made about the sensitivity of the detector to a gamma-ray signal. Although runs with different rates may contain valid events, the difference in sensitivity causes problems in interpreting the data. These runs comprise a small fraction of the entire data set. They can be removed with little consequence to eliminate the necessity of a complicated sensitivity analysis.

For the same reasons and the added concern that runs that were started and immediately stopped may have had some severe problem, runs containing less than 5 subruns (a subrun is about 5 minutes long) are removed from the data set for the AGN analysis. This removes <1% of the reconstructed data events (less than 2 days of data over the whole data set) causing little impact on exposure, but a large improvement in the quality of data examined.

The online analysis runs on all the data that is reconstructed online as it is acquired. Special runs or data that are recognized as problematic only after a first

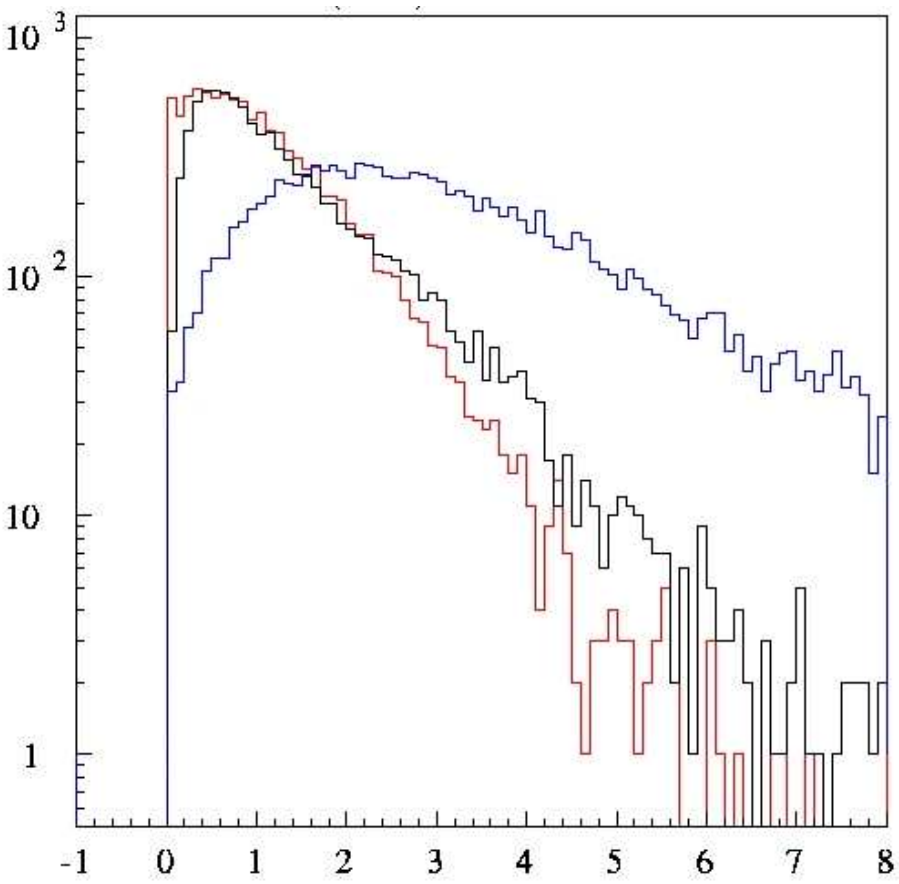

Figure 5.4: The distributions of the gamma-hadron separation parameter, X2, from simulated proton-induced air showers (black), simulated gamma-ray induced air showers (blue), and data (red).

analysis cannot be easily removed at this point. The online search, however, is dedicated to the quick location of a significant signal. It is reasonable to err on the side of reading data in this case. The flux calculation is a secondary procedure. In the event that a significant signal was detected, the data would be analyzed again to properly test the signal and determine the corresponding flux. The removal of runs with different sensitivities is not as critical for this style of search.

5.4 Background Estimation

Events that pass filtering are included in the signal map and background estimation. The background estimation for long duration analysis is done using direct integration (Atkins et al., 2003), a variation of the "background map" binned analysis method described in Alexandreas et al. (1993). The basic idea is that the efficiency for detecting events depends on the local angles and remains approximately constant for short periods of time. The angular distribution of accepted events is independent of the event rate. Although the rate may change over the period of integration, it can be

tracked and accounted for when calculating the background estimate. The method assumes that the cosmic-ray background at the top of the atmosphere is isotropic. The expected background is determined from the detector rate and the efficiency for detecting events from different parts of the overhead sky. The "background map" method randomly selects local angles (θ,ϕ) from those of observed events and gives them the times of real events to generate a background estimate in a (RA,δ) bin. Direct integration improves on this by using all the observed event locations within a band of declination to generate the background estimate for any bin at that declination.

The background estimation is a numerical integration of

$$N_B(RA,\delta) = \int\int eff(HA(t),\delta) Rate(t) \epsilon(HA, RA, t)\ dHA\ d\delta\ dt$$

where N_B is the background estimate within a bin at equatorial coordinates (RA,δ), eff is the detection efficiency at local coordinate (dHA,dδ), and ϵ is 1 if an event falls in the (RA,δ) bin at sidereal time, t. The hour angle, HA, is a function of sidereal time, $HA = t - RA$, and provides the conversion from the local, rotating acceptance coordinates to the static equatorial coordinates. The background map is determined by binning all the events in local coordinates (HA,δ). This local map is transformed into an efficiency map by dividing out the number of events in each bin by the total number of events observed in the integration period. At the end of the background integration period, two hours in this case, the local efficiency map is converted to a map in equatorial coordinates (RA,δ) by using the rate of events collected for each 24 s of time. The size of the time bin is 24 s to eliminate appreciable motion of the sky within the angular bin of 0.1°. Note that weighting the efficiency map by the observed rate gives the background events the same time distribution as the collected data. This compensates for any changes or gaps in the data rate. To attempt to summarize, the background estimation can be interpreted as taking all the available signal events at some declination and redistributing them smoothly according to the detector's angular acceptance. The fact that the angular acceptance is also determined by distribution of the signal events serves to guarantee that the current state of the detector is represented.

An assumption inherent in direct integration is that the efficiency for detecting air showers, a function of local angles, remains constant over the period in which the background is estimated. In other words, the shape of the detector acceptance in local coordinates is expected not to change. Because the atmosphere plays a role in the detector, the efficiency does change over the period of a day with varying pressure and temperature. Either the background map must be made shorter than the typical time scale of these changes, or the changes in the efficiency must be monitored and corrected in the background analysis. The analysis used in this work takes the former approach and limits the length of the background map to two hours. The optimal period for estimating the background is a balance of limiting the time, which reduces error in knowledge of the efficiency, and maximizing the number of events in the background, which reduces the statistical error by increasing knowledge of the background. Two hours is selected as a period in which the efficiency remains

approximately constant, but a large number of events is collected to estimate the background.

Using direct integration, a small fraction of the events used to estimate the background are from the signal bin of interest. This means that the background estimate will be higher in the presence of a gamma-ray signal because the extra excess events are included in the efficiency map. The effect of including the signal events in the background can be removed later from the event excess and the significance calculation (See Chapter 7).

An additional consequence of using the same event pool to estimate the background in the bins at the same declination is a conservation effect. The integration over the excesses and deficits within the declination band comes to zero. At the declinations of detected gamma-ray sources, the excess events due to the source cause an overall deficit in excess (increase in the background estimate) for the rest of the bins at that declination. On the contrary, the different bands of declination are completely independent in the background estimation and do not have a relative normalization. This has some consequence for absolute measurements of the background, but has no effect on evaluating the significance of gamma-ray source locations.

5.5 Optimal Bin Size

The signal and background event maps are initially binned in 0.1° RA x 0.1° δ square bins. The angular resolution of the detector is larger than this at ∼0.75°. A 0.1° bin will not contain most of the signal events from a point source. A bin size is selected to complement the angular variation in reconstructed shower direction and maximize the signal sensitivity. The optimal bin contains the most favorable ratio of signal events to background events. A small bin contains less background events, but not enough signal events fall within the bin. A large bin contains most of the signal events, but the background is also large. Something between these extremes returns the best significance for a signal.

The optimal bin size is determined using Monte Carlo simulations of gamma-ray induced air showers. The fraction of gamma rays showers that are reconstructed to originate within a circular bin of radius R is compared to the background expected in that bin. The background events scale with the area of the bin. The significance of an event excess in the Gaussian regime is approximated using

$$Significance \approx \frac{N_S - N_B}{\sqrt{N_B}} \propto \frac{N_\gamma}{R}$$

where N_S is the signal counts, and N_B is the background counts. This is proportional to the ratio of the fraction of successfully reconstructed gamma-ray showers to the radius of the bin. Figure 5.5 shows the dependence of the significance on bin radius. The peak occurs at a radius of ∼1.1°. The equivalent area square bin has a full width of 1.9°. There is little loss in sensitivity if a slightly larger bin is used, and a more noticeable loss if the bin is too small. For all analysis presented in this work, the slightly larger square bin width of 2.1° is used. The bin size is also scaled to have

equal area on the sky. This requires the width in RA to be scaled by $1/cos(\delta)$. The resulting bin is rectangular with a width of $2.1^\circ/cos(\delta)$ in RA and 2.1° in δ.

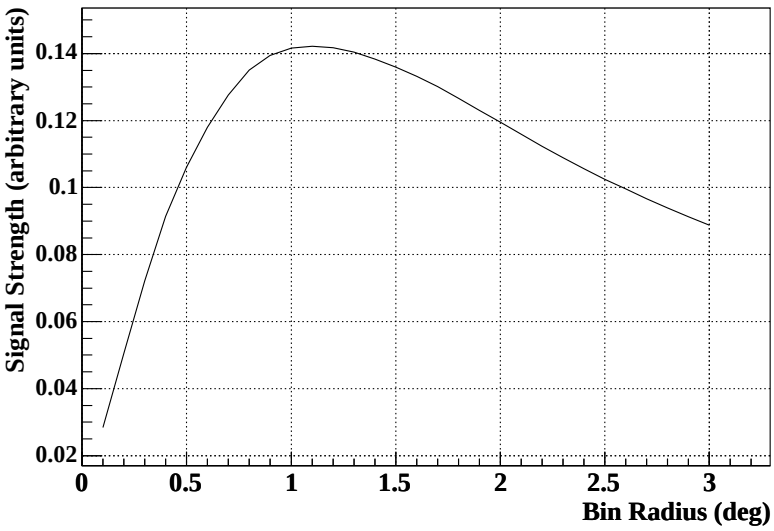

Figure 5.5: Dependence of the significance of a gamma-ray signal on the radius of the analysis bin containing the signal and background events.

5.6 Map Exclusion

In addition to the data filtering and cuts already described, a final cut is applied to the completed signal and background maps in the AGN analysis. The duration of the background map is required to extend over a time period long enough to encompass a search bin. The optimal bin size for a point source has a width of $2.1^\circ/cos(\delta)$ in RA. At the maximum source declination included in the AGN search, $\delta = 68^\circ$, the width of the search bin in RA is 8°. For the map to extend past the RA width of the bin, 2900 sec of data are required. For maps with durations shorter than this, the background estimation is incomplete and the maps are excluded from further analysis.

5.7 Flux Calculation

The measured photon rate in Milagro is converted to a value of the differential energy spectrum for the source. The calculation depends on the source declination,(δ), and the form of the photon energy spectrum, dN/dE. In the simplest case a power-law approximation is used.

$$\frac{dN}{dE} = I_0 \times (E/TeV)^{-\alpha}$$

The flux calculation uses the background subtracted event rate at the source position and solves the equation

$$\int_{Emin}^{Emax} A_{Eff}(E, RA, \delta) \times \frac{dN}{dE} dE = EventRate(RA, \delta) \tag{5.1}$$

for the flux amplitude, I_0. A_{eff} is the total calculated effective area for a source at (RA,δ) and with photon spectrum, dN/dE. A_{eff} is determined using Monte Carlo simulations of gamma-ray-induced air showers. A detailed discussion of the calculation of A_{eff} and the dependence of Milagro results on various gamma-ray source parameters can be found in Chapter 6. The remaining discussion focuses on the effects that the detector configuration and analysis parameters have on the calculation of flux. The most important effects to simulate are highlighted and the size of errors in the flux due to variation in these parameters are examined.

To accurately find the value for I_0, A_{eff} must represent the efficiency of the appropriate Milagro detector configuration and reconstruction analysis. To the conditions in the detector and the analysis cuts applied to the data, several cuts are applied to simulated gamma-ray events. A trigger condition is chosen to produce distributions of calibrated and fit PMTs from simulated events that are similar to the data. The data analyzed in this work is best represented by a simulated trigger requiring more than 55 PMTs in the event. To represent the typical operating state of the detector, some PMTs are excluded from simulated events. This compensates for PMTs that cease to operate properly and are disconnected from the electronics system. The typical number of "dead" PMTs in the data examined is $\sim$35 in the AS layer and $\sim$5 in the MU layer. The removal of this number of PMTs from the simulated events reduces the detection efficiency by decreasing the number of events capable of passing the trigger threshold. The inclusion of dead PMTs increases the calculated flux amplitude, I_0, by 5-13% depending on the assumed spectrum. The effect is larger for steeper spectra that correspond to a lower peak in the energy response. The effect of dead PMTs is included in all flux limits presented in this work.

For some periods of time, a few PMTs may lack calibrations and be excluded from the angle Reconstruction. To simulate this effect, a set of PMTs are considered for generating a trigger, but not for reconstructing the shower direction. A PMT without a calibration is also unavailable for the calculation of the gamma-hadron separation parameter, X2. With the exception of a period following the 2002 repair, few PMTs have lacked calibrations. The effect on the flux calculation is small and is not considered in this analysis.

Only successfully reconstructed gamma-ray showers contribute to the measured photon rate in the detector. To simulate a successful detection, a cut on the number of PMTs used in the angle fit (nFit) is applied to the simulated events. The same cut is used as that applied to data, nFit$>$ 20. Additionally, the reconstructed direction of the simulated event must fall within the analysis bin in order to contribute to the detected gamma-ray count. In the simulations, this requirement translates into requiring the angular difference of the reconstructed direction and the true direction for an event to be less than the analysis bin radius, 1.2°.

The gamma-hadron separation cut removes some gamma-ray events in addition to background events. The distributions of X2 from simulated proton-induced air

showers and data are similar, and imply that the distribution of X2 for simulated gamma-ray showers also matches that of real gamma-ray events. The simulated gamma-ray events are required to pass the same X2 cut that is applied to data. The AGN analysis and the current version of the online transient search both require X2>2.5. Variation of this cut in the calculation of A_{eff} produces a substantial change in I_0. If the mean of the X2 distribution shifts to higher values and the same cut is made, I_0 decreases by an amount similar the percentage of the shift. A shift to higher values effectively makes the cut looser than predicted and allows more gamma-ray induced showers to be detected. If the distribution shifts lower, then the cut is harder, and I_0 increases for the same detected photon rate. As an example, the shift in the PE calibrations moved the X2 distribution lower, or equivalently made the cut of X2>2.5 have the effect of a cut of at X2$\sim$2. The flux required to get the same detected photon rate from the Crab Nebula is less for this looser cut, but the background acceptance is too high. The significance is reduced. To see the Crab at the same significance takes a factor of 1.4 longer in time. Happily, the significance of the Crab after including the PE correction is as expected for the optimal X2 cut. This gives some confidence that the error in the X2 distribution is not at a discernible level when the correction is applied.

Two other detector-related effects are included in the flux calculation itself. The detector electronics cannot process any additional events until the current one is read by the DAQ. This "dead time" is measured from the trigger card to be around 8%. The "dead time" reduces the available exposure to gamma-ray events. To account for the effect on the calculated flux, the predicted event rate from the simulations is reduced by 8%.

The second effect accounts for the exposure to a particular part of the sky. The effective area is a function of RA. To accurately find the effective area for a location within a period of data, the RA exposure is included in the effective area calculation. Essentially, the effective area is integrated over time and includes only those times that the source was visible and the detector was operating. Over the entire data set the RA dependence of the observations is quite weak. There is little correlation over a whole year between down time and a particular part of the sky. Shorter periods of time may have a non-negligible difference in exposure for different times of day. As an example, the late summer produces thunderstorms at the Milagro site on most afternoons. If the power is out several afternoons in the same week, sources that are overhead during the afternoon will not have the same exposure as sources that are overhead during the night or morning. The analysis used to determine the flux limits for the AGN sample calculates the time in data spent at each 1° bin in zenith angle by each source to account for any disparity between the map length and the actual exposure to a source position. This is most critical in the shortest maps, but is applied for each of the time scale results presented in Chapter 8.

5.8 Analysis Confirmation

Each step of the analysis and the effects of the cuts are studied using comparisons of parameters in the data and the Monte Carlo simulations. The confirmation that everything is working as expected is best examined using a detected signal. Milagro has detected two gamma-ray point sources in the last 3 years of data, the Crab Nebula and Mrk 421. Their detections offer a measurement of Milagro's sensitivity and can be used to insure that the analysis and flux calculation are working as intended. The significance maps in Figure 5.6 are taken from the same data set used to generate the AGN results presented in Chapter 8. The Crab Nebula and Mrk 421 are the most significant locations in the whole map. The significance at the Crab location is 6.0σ and at the location of Mrk 421 is 4.1σ. When the analysis and flux calculation described above are applied to the Crab Nebula the resulting flux amplitude is $I_0 = 2.15 \pm 0.31 \pm 1.3 \times 10^{-11}\ cm^{-2}s^{-1}TeV^{-1}$ using $\mathrm{dN/dE} \propto \mathrm{E}^{-2.49}$ Hillas et al. (1998). If the measured value of the spectrum is taken instead from Aharonian et al. (2000b), $\mathrm{dN/dE} \propto \mathrm{E}^{-2.59}$, then $I_0 = 2.42 \pm 0.35 \pm 1.5 \times 10^{-11}\ cm^{-2}s{-}1TeV{-}1$. This value is consistent within errors with the flux results from IACTs when the appropriate spectral measurement is used. The systematic error is dominated by errors in the simulations which affect the calculation of effective area. The systematic effect on I_0 is estimated at 60%. Details of the flux calculation that include a description of the declination dependence of Milagro's point spread function are in Atkins et al. (2003). The detection of the Crab Nebula in this data set confirms that the analysis used is sensitive to a gamma-ray signal.

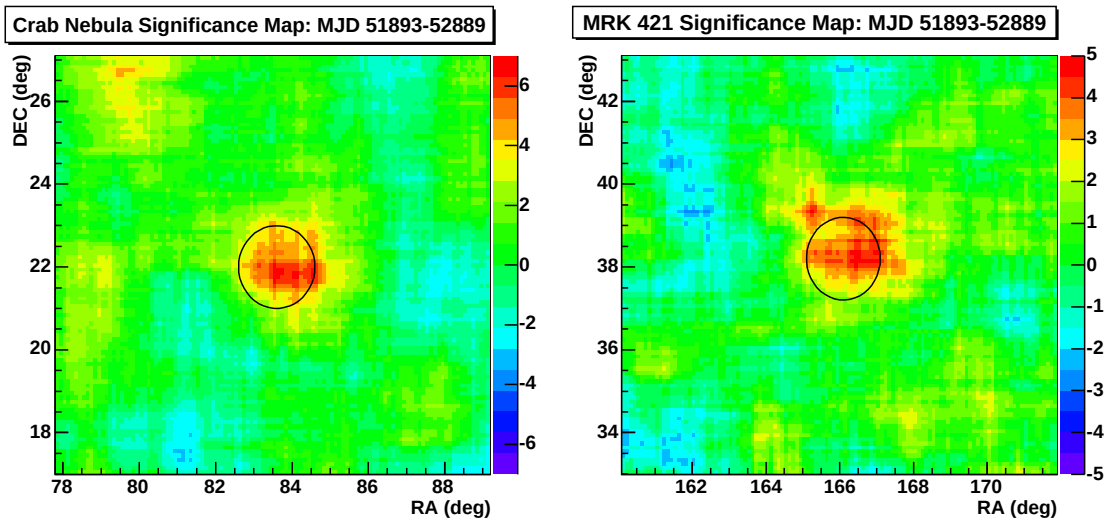

Figure 5.6: Sky maps of the significance of the excess for the locations of the Crab Nebula and Mrk 421. The data set used contains 906 days of exposure from 15 December 2000, through 8 September 2004. The two detections are the first and second most significant locations in the all-sky map for the analysis presented here.

Chapter 6

Interpreting Milagro Data for Extragalactic Point Sources

The interpretation of Milagro observations into an absolute flux from a source requires an understanding of the ability of the instrument to detect a gamma-ray signal. The detector response to sources is characterized by the efficiency with which air showers are detected. A successfully detected air shower must trigger the detector, have a reconstructed direction, and pass the analysis cuts applied to data. The efficiency with which these conditions are met depends on the local coordinates and energy of the gamma ray initiating the air shower, as well as the position of the shower core. When the efficiency is combined with an energy spectrum, it translates the excess event rate in Milagro to the photon flux from a source. When extragalactic sources are observed, parameters such as the path of the source through the sky and the source redshift must also be considered.

6.1 Simulated Gamma-Ray Events

There is no way to send a controlled sample of gamma-ray induced air showers with a known direction and energy into the detector. The showers and interaction of shower particles with the Milagro detector are instead simulated using Monte Carlo methods. The detection efficiency is determined from a simulated event sample to evaluate the detector response. The simulated showers cover the full range of parameters that produce detectable air showers in order to accurately evaluate detection efficiency.

The range of zenith angle, initial particle energy, and shower core location used to generate simulated events are chosen to represent the full set of gamma-ray air showers that can trigger the detector, be reconstructed, and pass analysis cuts. The shower core location is defined in terms of the radius from the center of the detector. The ranges of parameters used for the simulated showers are shown in Table 6.1. These were selected such that showers with parameters outside this range are detected with negligible efficiency and can be ignored as shown in Figures 6.3 and 6.2.

Parameter	Simulation Range
Zenith Angle	$<45°$
Gamma-Ray Energy	0.1 TeV - 100 TeV
Core Radius	<1000 m^2

Table 6.1: Parameter ranges used for Monte Carlo simulated gamma-ray air showers.

6.2 Energy Dependence

One parameter used to characterize the energy response of an astrophysical detector is effective area, A_{eff}. Effective area describes the efficiency for successfully detecting a gamma-ray induced air shower based on the primary gamma-ray energy and the zenith angle at which the shower originates. Effective area is calculated by combining the detection efficiency for a set of simulated gamma-rays with the total area in which the simulated air showers fall.

$$A_{eff}(E,\theta) = efficiency(E,\theta) \times Area \tag{6.1}$$

The effective area for Milagro is shown as a function of energy in Figure 6.1. It is also a function of position in the overhead sky and is shown divided into three ranges of zenith angle. The areas are calculated only for those events falling within the specified range of θ. The θ dependence is discussed further in the next section. The effective area at energies above 10 TeV exceeds 10^4 m^2. Notice that this exceeds the physical size of the pond, which is 4.8×10^3 m^2. This demonstrates that Milagro has some efficiency for detecting air showers with core locations outside the boundaries of the pond. A successful detection of an air shower only requires enough PMTs to generate a trigger and reconstruct the shower direction. At very high energies, some portion of showers with cores off the pond meet these conditions. The total area covered by the simulated showers, 3×10^6 m^2, is chosen to include the entire area in which the shower core can fall and still be detected. Simulated gamma-ray air showers with core radii beyond 10^3 m are detected with negligible efficiency and may be safely ignored.

Effective area indicates the range of gamma-ray energies over which Milagro has some detection efficiency. The effective area is small at low energies where gamma rays rarely penetrate deeply enough into the atmosphere to generate an air shower with an appreciable size at the altitude of Milagro. The effective area increases with energy as more showers are initiated deeper in the atmosphere. Higher energy showers are detected very efficiently, but this must be taken in context with the steeply falling energy spectrum of gamma-ray sources. The increased detection efficiency makes little difference at energies where there are few gamma-rays to be found. For this reason, the effective area alone is not enough to define the sensitivity to a source.

A source-specific way to examine the sensitivity to gamma rays comes from combining the effective area with an energy spectrum. The effect on sensitivity of including an energy spectrum can be seen in the distribution of detected gamma-ray energies. Figure 6.2 shows the distribution of detected gamma-ray energies for an

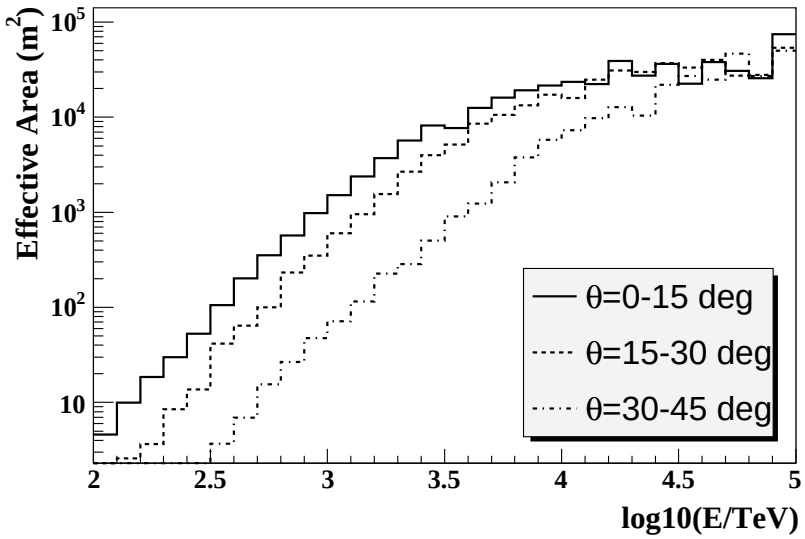

Figure 6.1: Effective area in m^2 as a function of the log of energy in GeV. Area is shown separately for gamma rays in different ranges of zenith angle, θ.

energy spectrum similar to that of the Crab Nebula. The median energy for the distribution is 3.6 TeV. 90% of the detected gamma rays from a source with this spectrum fall between 400 GeV and 35 TeV. The median energy provides a reasonable description of the gamma-ray energy at which Milagro is most sensitive to this source.

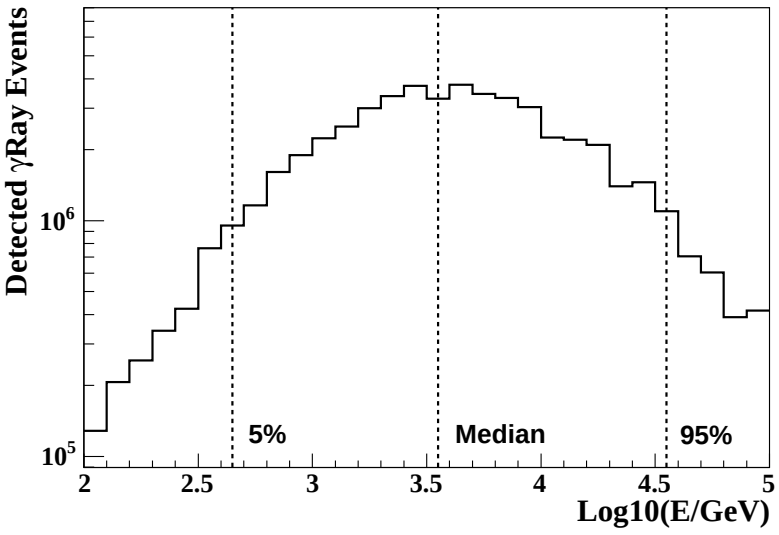

Figure 6.2: Detected events in bins of gamma-ray energy for $dN/dE \propto E^{-2.4}$. The median energy is indicated by a dotted line as well as the energies above which 5% and 95% of the detected gamma rays fall.

6.3 Declination Dependence

Milagro's sensitivity to a source depends strongly on local coordinates. The amount of atmosphere between the point at which a gamma ray interacts and the location of the Milagro pond determines the typical gamma-ray energy required for an air shower to be detected. The azimuthal angle, ϕ, has little effect on detection efficiency because of the symmetries of the atmosphere and the detector. The width of atmosphere an air shower crosses depends primarily on the zenith angle, θ. Figure 6.3 shows the decrease in detected events with increasing θ. The low number of detected events near 0 is a geometrical effect due to the reduced area of sky at small θ. Milagro has some efficiency for events originating at zenith angles beyond 30° but is much more sensitive to locations nearer to overhead.

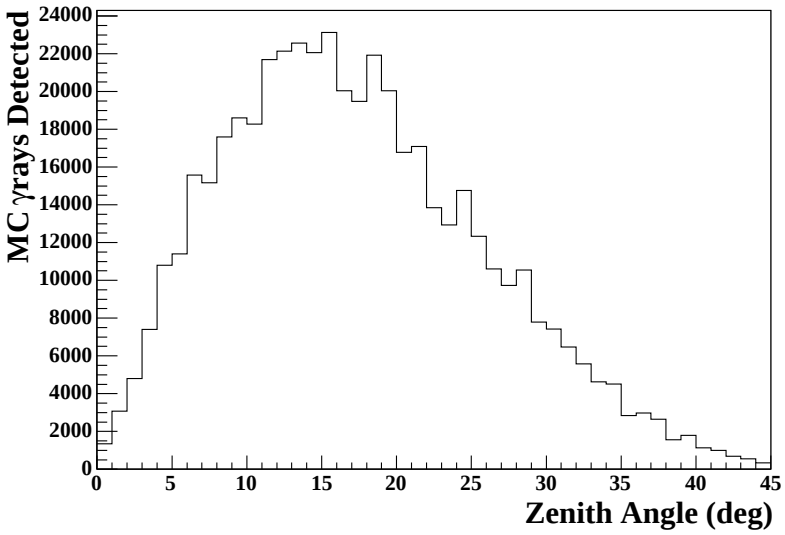

Figure 6.3: Detected Monte Carlo gamma-ray events with energies from 0.1 TeV to 100 TeV as a function of zenith angle, θ.

The rotation of the Earth causes any source observed for more than a few minutes to pass through a range of zenith angles. Searches for long-term transients use maps of the sky constructed from a series of two-hour observations. In two hours the Earth rotates 30°. There is a significant change in the sensitivity of the detector to a point source as it travels over the detector. Objects that pass directly overhead spend more time at zenith angles with high detection efficiency.

To properly account for the path of a point source through the local sky, the detection efficiency is integrated over the zenith angles for each point along the source path.

$$A_{eff}(RA, \delta) = Area \int_{t_1}^{t_2} efficiency(\theta(t, RA, \delta))\ dt \tag{6.2}$$

where θ is a function of time and declination, and t_1 and t_2 represent the times that a source at a specified RA passes into and out of the field of view. Over a full sidereal

day, the amount of time spent at each θ is the same for all RA positions at that δ and the RA dependence drops out. The detection efficiency for a point source over long observations can be stated as a function of declination instead of zenith angle.

6.4 Sensitivity to Energy Spectra

The energy at which Milagro is most sensitive to a source depends on the assumed energy spectrum in addition to the source declination. The plot of effective area as a function of energy (Figure 6.1) shows that Milagro detects gamma rays over a broad energy range. It also shows that there is no well-defined lower limit in energy for the gamma-rays detected from a source. The convention used by other high energy telescopes of turning an event rate into the integral flux above a threshold energy does not work particularly well in this case. The reconstruction methods used for Milagro data presented in this thesis do not provide any energy resolution. The energy spectrum for a source cannot be measured and, therefore, must be assumed to calculate the flux from a source. Because of the lack of energy resolution and the broad range of energies detected, a calculation of flux from a photon rate in Milagro depends on the energy spectrum assumed.

The fundamental shape of the assumed energy spectrum is chosen to be a power law,

$$\frac{dN}{dE} = I_0(E/TeV)^{-\alpha} \tag{6.3}$$

where I_0 is a constant indicating the photon flux from a source at a specific energy and α is the spectral index defining the shape of the energy spectrum. The function is simple to manipulate and is a good approximation to the emission expected from very high energy sources. Beyond the physical reasons for expecting a power law because of the shock acceleration involved in producing emission, power laws also fit reasonably well to very high energy observations of AGN. The canonical TeV source, the Crab Nebula has an energy spectrum well fit by a power law at TeV energies. The power-law fit to the spectrum observed by the Whipple Air-Čerenkov Telescope finds $\alpha = 2.49$ (Hillas et al., 1998).

A spectrum such as Equation 6.3 is convolved with A_{eff} and integrated over the simulated energy range to produce a predicted event rate in Milagro. Using an observed event rate in Milagro accomplishes the opposite, a measurement of I_0 when the appropriate effective area for the source is used. A detailed discussion of the flux calculation is included in Chapter 5.

The median energy of detected events gives the peak of Milagro's energy response for the spectrum and declination of a source. Taking the Crab Nebula as an example, the shape of the assumed energy spectrum is as in Equation 6.3 with $\alpha = 2.49$ and $\delta = 22°$. Using these inputs, the median energy for detected events is 4 TeV (Figure 6.2). At the same declination a steeper spectrum, α=3, shifts the peak of the distribution of detected events to lower energies with a median of 1 TeV. A shallower spectrum, α=2, moves the median energy higher, to 9 TeV. Changing the declination while keeping α fixed also changes the median energy. The Milagro

detector is located at 36° latitude and performs best for sources at that declination. For α=2.49, the median energy of detected events is 3.2 TeV at δ=36°, 8 TeV at δ=6°, and 15 TeV at δ=-4°.

The effects of the spectral index and declination of the source on Milagro's energy response are summarized by Figure 6.4. The figure shows the median energy of detected events as a function of declination for several spectral indexes. The optimal field of view can be deduced from the regions where the median energy for a particular α is flat in declination. The median energy of detected events increases quickly for declinations with transits passing further than 30° from zenith where the path to Milagro through the atmosphere is longer. At large zenith angles, higher energy photons have a much higher probability of generating air showers that can be detected. However, for a power law spectrum the number of photons available at higher energies drops rapidly. In this context, a higher median energy indicates reduced detector sensitivity to a gamma-ray source.

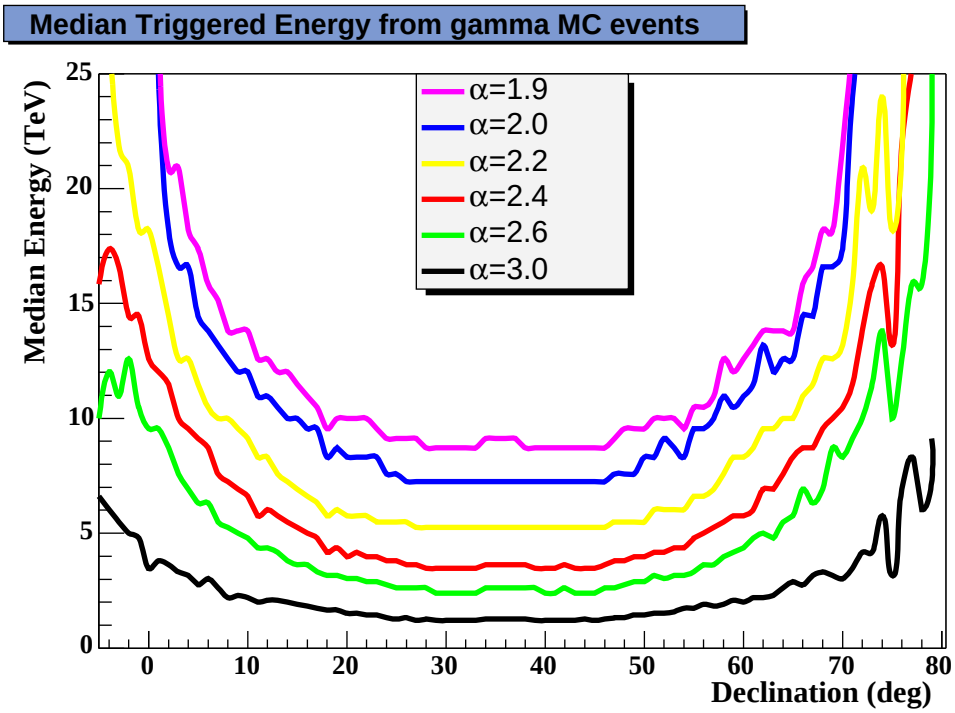

Figure 6.4: Median energy of detected gamma-ray events in Monte Carlo simulations assuming $dN/dE \propto E^{-\alpha}$.

The interpretation of the median detected energy is inverted for the comparison of spectral indexes. The median energy increases for a sources that produce more photons at higher energies, where Milagro has more effective area. Contrary to the interpretation for declination, the increase in median energy for fixed δ and decreasing α indicates a better detector response. The best way to interpret both trends together is to consider that the gamma-ray source to which Milagro is most sensitive has a low α and passes directly overhead. For a declination further from overhead and an increased spectral index, the sensitivity decreases.

The median energy for detected events also indicates the energy at which a Milagro measurement of flux is traditionally given. Observations over a broad range of frequencies for a source are combined in the spectral energy distribution (SED). To place a measurement on the SED, a suitable energy must be selected for the observation.

Source spectra are often expressed as νF_ν, where ν is frequency and F_ν is the photon flux at some frequency. This is proportional to $E^2 dN/dE$. The median energy of detected events in Milagro gives the value at which the measured value for the source spectrum is least sensitive to changing the assumed spectral shape. For example, if two spectral indexes are assumed to calculate flux from the same photon rate in Milagro, the νF_ν value will change the least if it is calculated at the median detected energy. A graphical example of this is given by Figure 6.3. Expressing Milagro results in this way removes some of the dependence of the result on the assumptions made about the source spectrum.

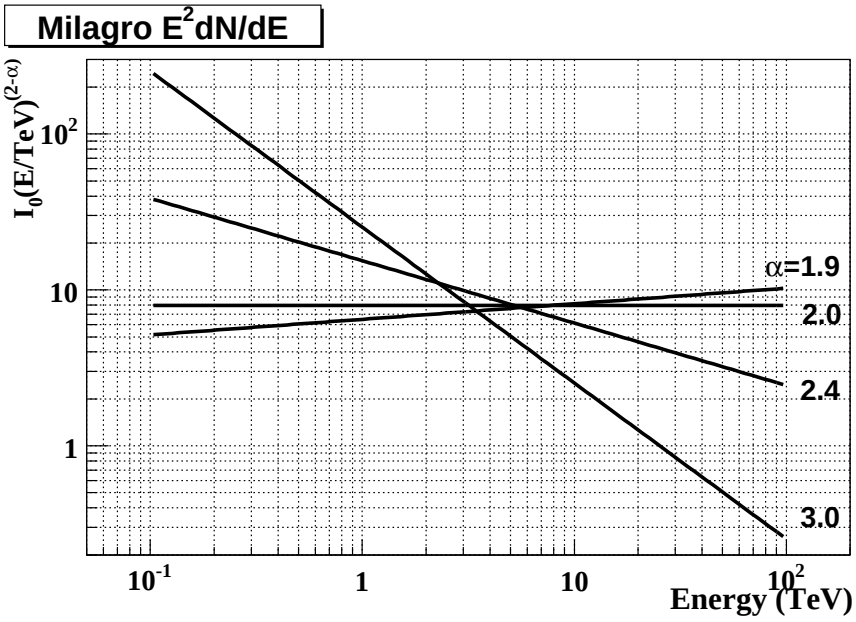

Figure 6.5: $E^2 dN/dE$ as a function of energy, where $dN/dE = I_0(E/TeV)^{-\alpha}$. I_0 is calculated from Monte Carlo simulations using the same Milagro event rate for each line and assuming different spectral indexes. The region where the lines intersect indicates the energy at which the energy flux is least dependent on the assumed spectrum. The center of this region is 4.3 ± 1.4 TeV.

The power-law fit to an energy spectrum can be easily adjusted to allow for the absorption of high energy photons. An energy dependent attenuation or an exponential energy cut off can be included on top of the power law dependence as

$$\frac{dN}{dE} \propto (E/TeV)^{-\alpha} e^{-\tau(E,z)} \tag{6.4}$$

or

$$\frac{dN}{dE} \propto (E/TeV)^{-\alpha} \exp^{-E/E_c} . \tag{6.5}$$

In the case of an energy spectrum with a cut off there are two possibilities for the peak energy response. The cut off either lies above or below the median energy for the underlying power-law energy spectrum without the cut off. If the cut off falls higher in energy than the median energy, the energy of peak detector sensitivity to a source is the median energy. Otherwise the peak is at the energy cut off. This simply says that the peak energy response is either at the energy at which the detector can best detect photons from an unattenuated spectrum or else the energy where the most photons are available to be detected.

Although the energy cut off for some sources lies below the typical median energy for an unattenuated spectrum, there is still some efficiency for detection. This is because Milagro has effective area down to ∼100 GeV. Milagro has a reduced sensitivity to sources with an energy cut off , however, depending on the shape of the spectrum, it may be a relatively small loss. The change in sensitivity to a source depends on the energy of the cut off as well as the power law index.

Figure 6.6 and Table 6.2 illustrate the change in the differential flux amplitude, I_0, for assuming power-law energy spectra with and without energy cut offs. E^2dN/dE is plotted assuming several spectral shapes. For each shape, I_0 is calculated using the same observed count rate in the detector. I_0 determines the "height" of the spectrum on this plot. Table 6.2 lists the calculated I_0 values for each spectral shape with the median triggered energy for that spectrum and the integrated flux above the median energy. An increase in the calculated I_0 for a fixed event rate indicates a decrease in sensitivity to a source with that spectral shape. Changing the assumed spectral shape requires I_0 to change to compensate for the energy distribution of photons.

α	E_c (TeV)	I_0 ($10^{-11} \frac{phot}{cm^2 sTeV}$)	E_{med} (TeV)	$F > E_{med}$ ($10^{-12} \frac{phot}{cm^2 s}$)
2.1	none	0.96	6.31	1.09
2.1	3	3.73	1.74	4.59
3.0	none	2.53	1.32	7.26
3.0	3	4.31	0.72	24.69

Table 6.2: Calculated values and selected parameters for Figure 6.6. Assuming $dN/dE = I_0 E^{-\alpha} e^{-E/Ec}$ and an event rate of 10 $phot/day$, the photon flux amplitude, I_0, is calculated for a hypothetical source at $\delta = 26°$. The median triggered energy from simulations and the integrated photon flux above the median triggered energy are also given.

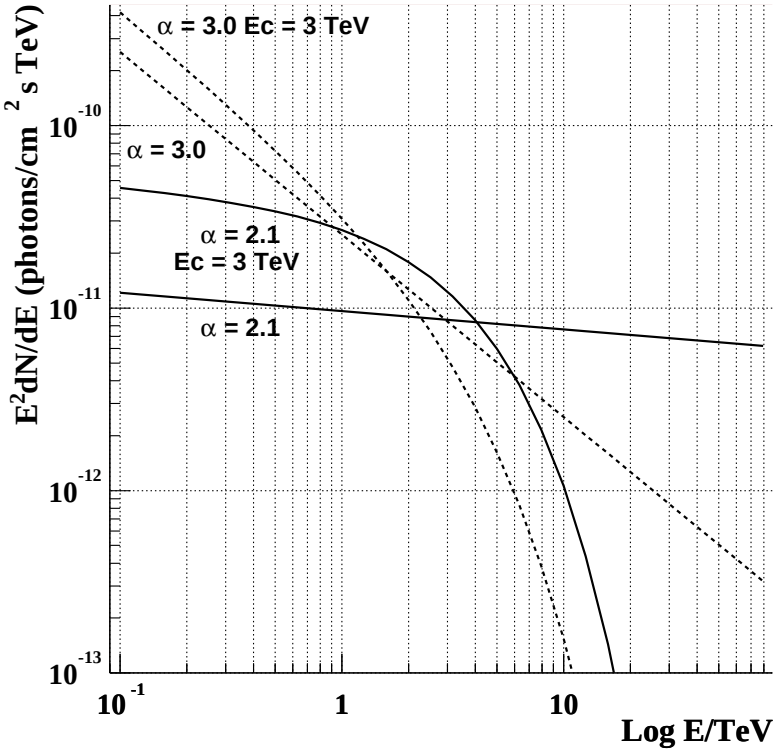

Figure 6.6: Differential flux dependence on the assumed energy spectrum. The plot shows E^2dN/dE, where $dN/dE = I_0(E/TeV)^{-\alpha}e^{-E/E_c}$. The exponential factor is dropped in the case of no cut-off energy. For each curve the event rate in the detector is chosen to be the same and the differential energy flux is calculated for different values of α and the cut-off energy, E_c. The resulting values of I_0 for each combination are given in Table 6.2.

6.5 Sensitivity to Extragalactic Sources

The emission from extragalactic sources is susceptible to attenuation by IR background light from stars and dust re-radiation. Observations by IACTs provide evidence for energy cut offs of a few TeV for nearby blazars ($z < 0.13$) (Samuelson et al., 1998; Krennrich et al., 2001; Aharonian et al., 2002b, 2003a,b). The absorption of TeV energy photons on IR background photons reduces or eliminates TeV gamma rays. This causes a cut off in the energy spectrum at the energies for which Milagro has the best energy response. When deducing the sensitivity of Milagro to steady state or flaring emission from extragalactic sources such as AGN, redshift dependent attenuation should be included to represent a realistic shape for the spectrum. Declination, photon index, and redshift dependent attenuation effects must be considered together to properly characterize the energy response and source sensitivity.

6.5.1 Infrared Background Models

In the absence of measurements necessary to determine the density of the IR background, theoretical models of IR background radiation are used to correct for absorption. The sensitivity calculations presented here are made for both IR models discussed in Chapter 2 to provide a comparison of the effect on Milagro data of different shapes of the EBL SED. The baseline and evolution models from de Jager & Stecker (2002) are referred to as IR1a and IR1b. The parametrization of a semi-analytic model for LCDM cosmology from Bullock (1999) is referred to as IR2. Both models parameterize the optical depth of the universe, τ, as a function of redshift and energy. The absorbed spectrum for the source takes the form of Equation 6.4. When only one model is used, IR1a is selected because the predicted τ typically falls between that of IR1b and IR2 (see Chapter 2).

6.5.2 Median Energy with Attenuation

An energy dependent reduction of gamma rays from a source changes the peak of the energy response. To look at the effects of increasing redshift on energy response, Figure 6.7 reveals the change in the detected gamma-ray distribution caused by redshift dependent attenuation. Figure 6.8 shows the dependence of median energy on declination for several redshifts. The median energy curve flattens in declination with increasing redshift. For the $z = 0$ median energy plot, the flat region corresponds to declinations with similar sensitivity. For larger redshifts, the flattening actually indicates a loss of higher energy photons, which initiate the majority of detectable events at declinations far from zenith. The sensitivity at those declinations for $z > 0$ is actually quite low (fig 6.9).

6.5.3 DC Sensitivity

To characterize the extragalactic sources detectable using Milagro, the photon flux amplitude required for a detection is calculated for various source parameters. An object with a photon spectral index of 2.59 is selected as an example for steady-state emission This hypothetical source is placed at a redshift by adding attenuation using a spectrum with the form of Equation 6.4 and applying IR1a. The photon flux amplitude required for a detection at 5σ in a year is calculated using the assumed spectrum and varying the declination and redshift values.

The 5σ photon rate in the detector is determined using the measured background data rate at the declination of the source. To make a realistic calculation, the dead time in Milagro, $\sim 91\%$, is included in the exposure converting 1 detector year to 332 days of exposure. The measured background levels for 332 days of data are used to determine the event rates required for a 5 sigma excess at $\delta = 36°$,$26°$, $21°$,and $6°$. The necessary flux amplitude is calculated over a range of redshifts using several declinations (Figure 6.10) and over a range of declination using several redshifts (fig 6.9) to illustrate the effects of varying each parameter. The photon flux amplitude is normalized by that of the Crab Nebula measured by Milagro, where

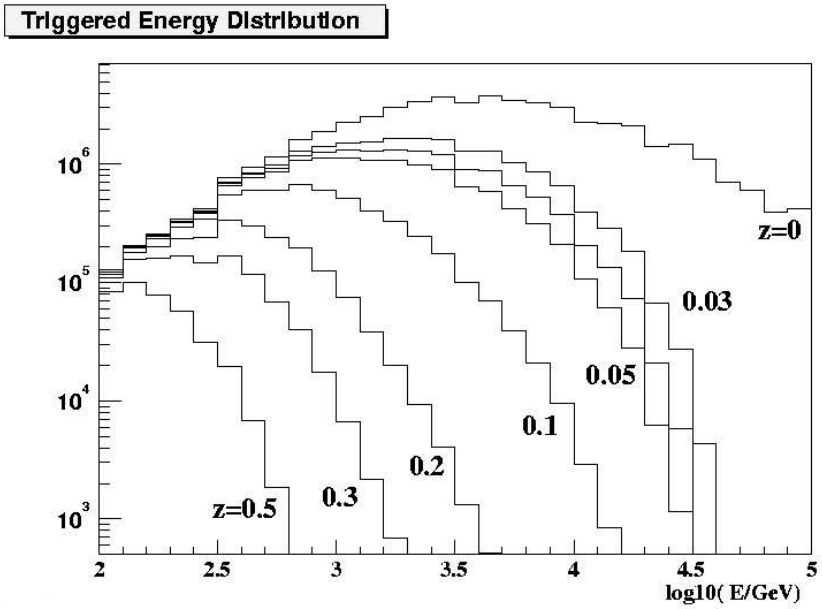

Figure 6.7: Dependence of the triggered energy distribution on redshift for a source with an $E^{-2.4}$ spectrum. Attenuation is calculated using IR1a.

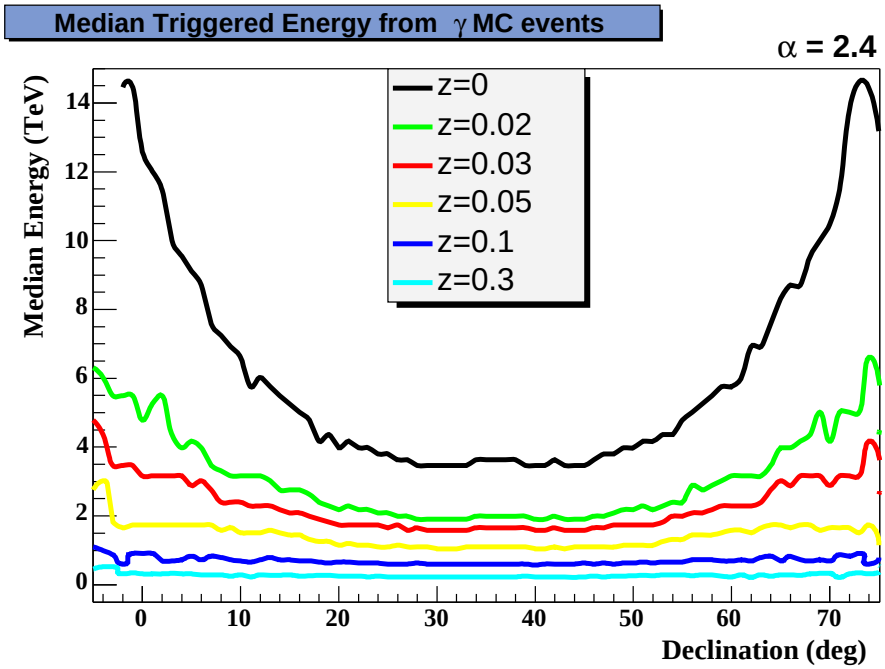

Figure 6.8: Median energy for $dN/dE \propto E^{-2.4}e^{-\tau(E,z)}$ using IR1a. The energy flattens in declination with redshift, but the source sensitivity (fig 6.9) shows that as redshift increases the sensitivity drops at declinations further from zenith where detected photons must have higher energies.

$I_0(Crab) = 1.8 \times 10^{-11}\ phot/cm^2\ s\ TeV$ when corrections specific to the declination are excluded. The plot of detectable flux variation with declination (Figure 6.9)

demonstrates the effect of redshift narrowing the field of view. The same sensitivity threshold at $\pm 30^\circ$ from overhead for $z = 0.02$ is at $\pm 15^\circ$ at $z = 0.10$ for a $5\sigma/\sqrt{yr}$ detection.

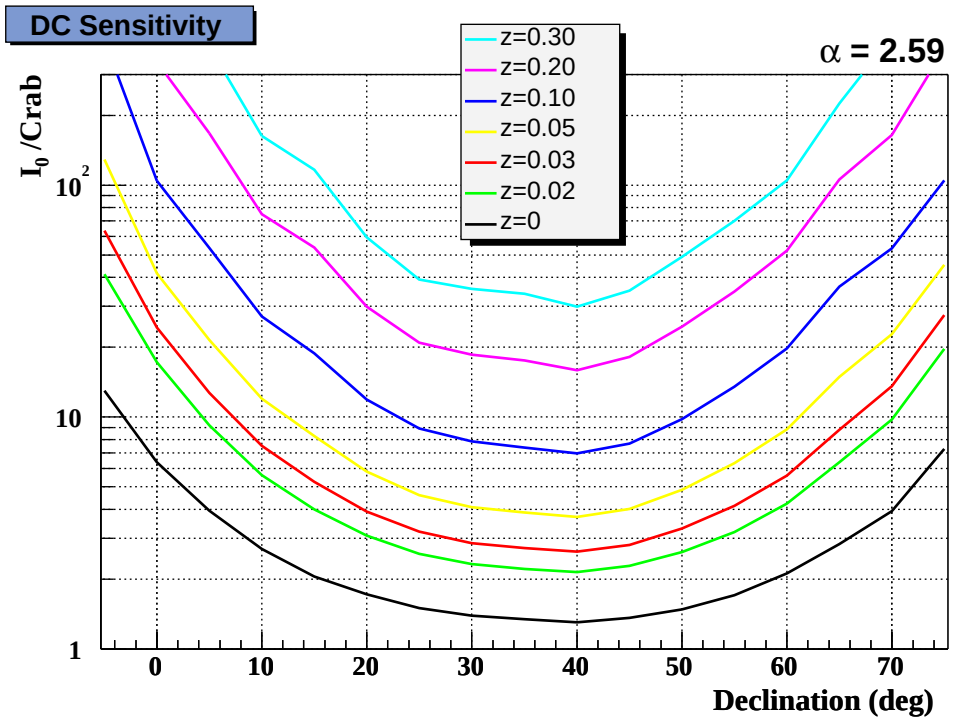

Figure 6.9: Photon flux amplitude, I_0, in Crab units required to get a $5\sigma/\sqrt{yr}$ excess for a source at a given redshift as a function of declination. 1 year = 332 days of exposure. The assumed spectrum is $dN/dE \propto E^{-2.59}e^{-\tau}$ with τ calculated using IR1a.

6.5.4 Exposure Dependence

The sensitivity to a source also depends on the duration of an observation. Sensitivity is judged by the significance of an excess. In the Gaussian approximation the significance is $Excess/\sqrt{Background}$. The excess for a source increases linearly in time as does the background. The significance grows as $\sqrt{time}$. Shorter exposures have reduced sensitivity compared to the 1 year example. (Excepting, of course, the very short exposures relevant to GRB emission, where the background becomes small and the sensitivity improves for shorter exposures.) For a 1 month exposure, an increase in event rate and, therefore, the photon flux amplitude by a factor of 3.5 is required to achieve a detection of the same significance as in a 1 year exposure. The sensitivity given for a particular exposure can be scaled to any other length of exposure (>2 hours) using this relation. If the gamma-ray horizon for Milagro is defined as the redshift where a source needs more than 10 times the Crab flux for a 5σ detection, then, for 1 year the horizon is at $z = 0.1$ and for 1 month it is at $z = 0.04$.

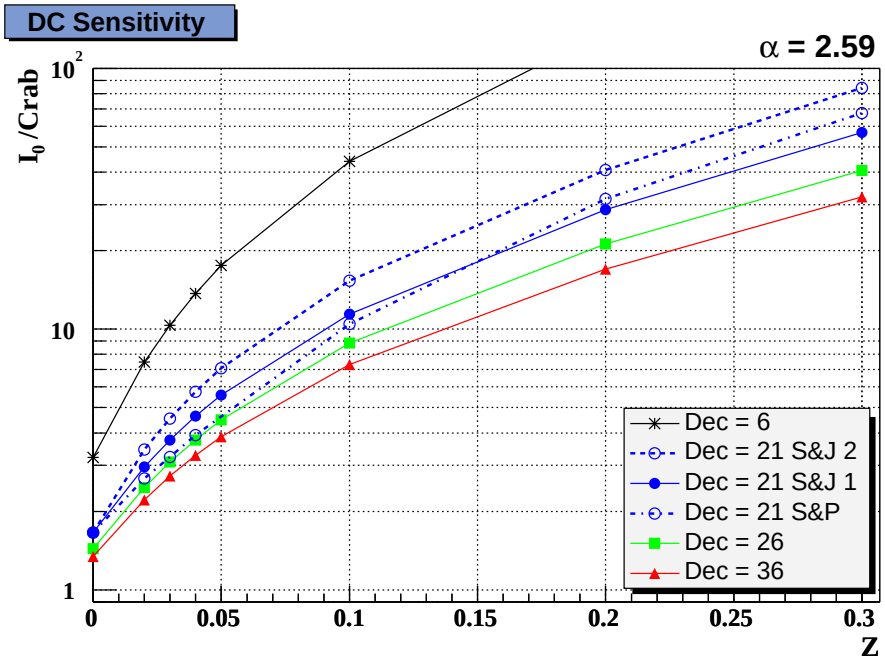

Figure 6.10: Photon flux amplitude, I_0, in Crab units required for a $5\sigma/\sqrt{yr}$ detection using $dN/dE = I_0(E/TeV)^{-2.59}e^{-\tau}$ with τ calculated using IR1a. The flux is shown for several declinations. At $\delta = 26°$, τ is calculated using IR1b and IR2 for comparison.

6.5.5 Flaring Sensitivity

The general trends of sensitivity relating to redshift remain the same for shorter timescale observations as for the steady state case. The level of flux amplitude required for a detection increases to compensate for reduced exposure. The flaring example is similar to the steady-state example with considerations for reduced exposure and observed blazar spectra included. A detection is defined as requiring 5σ in a detector month, ~27.3 days of exposure. The background is determined using measured background levels from data at a specified declination scaled to the time period of interest. A blazar in a flaring state may have a flatter spectrum than the steady state example according to spectral measurements by IACTs (Krennrich et al., 1999; Petry et al., 2002; Aharonian et al., 2002b, 2003a). A flatter spectra requires lesser values of I_0 to be detectable in Milagro. The results shown in Figure 6.11 are for a photon index of 2.2 taken from the measured time-averaged flaring state spectrum for Mrk 421 (Aharonian et al., 2002b). For comparison a steeper photon index and additional IR models are also applied.

Just as in the steady-state case the field of view narrows with redshift. The underlying power law makes less of a difference as the attenuation due to redshift increases. A detection of flaring on time scales of a few months limits the redshift horizon in Milagro to redshifts of 0.04 to 0.05.

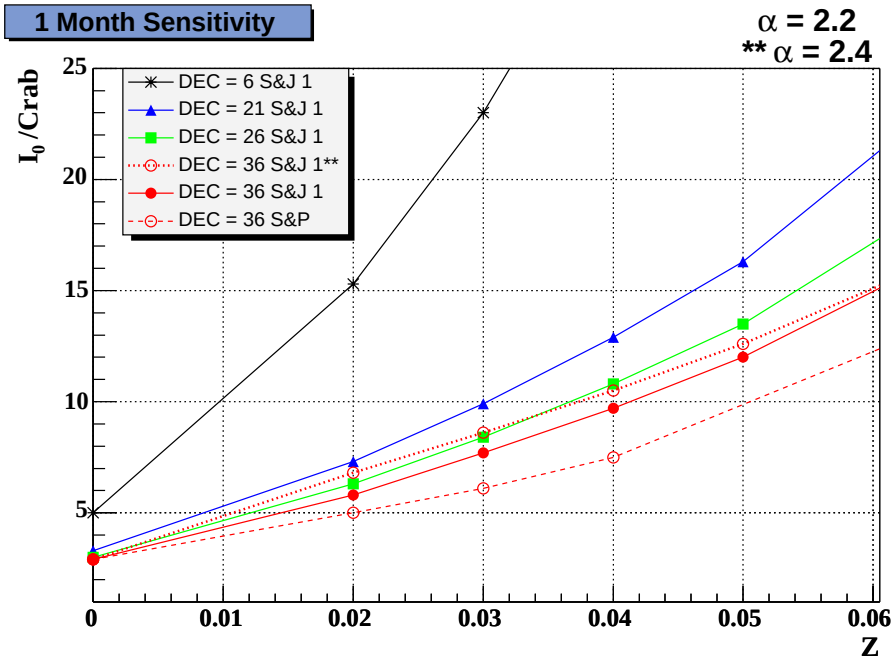

Figure 6.11: Photon flux amplitude, I_0, in Crab units required to get a $5\sigma/\sqrt{month}$ excess is calculated for a source at $\delta = 6°$, $21°$, $26°$ and $36°$ with $dN/dE = I_0(E/TeV)^{-2.2}e^{-\tau}$ where τ is calculated using IR1a. One month is defined as 27.3 days of exposure. At $36°$ results are shown for a $\alpha = 2.4$ and for τ calculated using IR2.

6.6 Summary

The sensitivity of Milagro to AGN cannot be described using a single parameter or plot. Spectral shape, which has two components in the formulations used here, and declination have interrelated effects on sensitivity. Because of the form of the energy response, one has to be taken in the context of the other. The median energy is important for describing Milagro's energy response and combining Milagro results with other measurements of flux predictions. Discussion of sensitivity requires a generalization that addresses all the relevant parameters. The parameter space for the flux calculation is greatly reduced in the case of specific sources. Sources with a measured redshift only lack a measured spectral index and the flux calculation is greatly simplified. Although the TeV spectra are unmeasured for the subjects of a search, calculations of flux limits in Milagro can be determined and used to constrain emission models and energy cutoff predictions.

Chapter 7

An All-Sky Search for Transients from Two Hours to Two Years

TeV astronomy remains a relatively new field of study. There have been very few comprehensive surveys of the sky at TeV energies. The question of what types of transient sources populate the universe at very high energies is largely unanswered. Observations of likely TeV sources have led to detections of transients. IACTs have discovered several AGN that achieve multi-TeV emission in flaring states. At very short durations, the Milagro prototype, Milagrito, produced evidence for TeV emission from GRB 970417a (Atkins et al., 2000a). These objects were all pre-selected as likely sources of TeV emission using information from other wavelengths. This type of targeted search is necessary for pointed instruments and useful for the discovery of additional objects within a known source class. It does not, however, provide the means to discover unpredicted sources. [1]

The large field of view and high duty cycle of Milagro provide observations of the Northern sky at TeV energies on a daily basis. The all-sky capability allows for non-targeted searches over a large range of times. The potential exists to find sources that are only be observable for a limited period of time and are not predicted to be TeV emitters. Milagro makes a unique contribution with real-time searches of data for undiscovered transient activity at TeV energies. Timely notification of possible detections is necessary to enable confirmation and follow-up observations by other instruments. Such observations can provide detailed light curve and spectral information for a detected transient, which may allow an identification to be made.

Fast notification is critical in the case of GRB activity, which lasts only a few seconds or minutes. Very short duration searches are run on Milagro data for activity on time scales from 250 μs to 40 s with a response time of 4 minutes for an alert. An intermediate duration search covers 40 s to 3 hr durations, which are relevant to GRB afterglow emission and possibly short, very bright AGN flares (Morales, 2002). The long time scale transient search monitors maps extending from two hours to the length of the real-time data set. The time durations covered by the long search are most relevant to AGN flaring activity. The three searches together cover the entire range of observation times available to Milagro and allow the earliest possible

[1] The recent discovery of a second unidentified, serendipitously detected TeV source suggests a strong possibility of additional TeV sources that may be obscured at lower frequencies.

knowledge of significant activity. In this chapter, analysis and results are presented for the long time scale transient search. Details of the shorter duration searches are available in Smith et al. (2001), Atkins et al. (2004a), and Morales (2002).

7.1 Search Durations

The long time scale transient search examines data from two-hour periods up to the summation of all data processed by the search, 2 yr. The two-hour duration is the shortest time for which a background estimate is generated by the standard point source analysis (Chapter 5). Longer maps are simply additions of consecutive two-hour maps of the signal events and background estimates. A single two hour map includes events from $\sim$1/3 of the northern sky. The sensitivity is much better in the central region of the map that is in view for the full two-hour period than the edges that enter and leave the field of view. The signal counts indicated in Figure 7.1 give some indication of the sensitivity variation over the region observed. The edges of the map are at large zenith angles and include substantially fewer events. This disparity in RA is removed in the longer maps that include observations of each portion of the sky as it passes overhead.

The next longest time scale is chosen to encompass a full source transit. A source at declination, $\delta = 36^\circ$ transits in 7.5 hours. A day-long map can contain the full overhead path for any source location depending on where the observation begins in RA. Any given 24 hour period will have a time boundary occurring during the transit of a set of locations in RA. To compensate for interrupted transits, two sets of day-long maps are made offset from each other by 12 hr. In this way, sensitivity to flaring activity during a single transit is not lost, and any location in RA has an uninterrupted transit included in a single map. Over the course of a sidereal day (23.93 hr) all locations in RA pass overhead, and the exposure is uniform in RA.

Real-time searches also examine maps of each week and month of data. These searches add consecutive day and week maps into week and month maps respectively. The maps for time scales longer than one day are not currently constructed to overlap in time. Sensitivity to a signal improves for overlapping maps, as discussed in the following chapter, but the philosophy of this search is that as a first attempt, a search coarsely binned in time is sufficient to detect a bright flare. In future updates, the search could be expanded to have overlapping coverage and additional time scales.

The longest maps examined are year-long maps and a map that encompass the entire real-time data set. These maps are generated using a slightly different analysis than that used in the real-time searches. The same reconstructed data is examined, but the analysis is updated to include recent improvements. This is necessary because Milagro has been under development during the time period of the full search and several changes have been made to the reconstruction analysis. In time periods longer than a few months, a second, updated analysis is typically better than that run online at the time the data was initially collected. This is due to improvements to the analysis routines and calibration corrections. The second analysis allows an examination of the data at an improved level of sensitivity and provides the most

up-to-date results for those time scales that do not require a fast response.

7.2 Search Procedure

The two-hour, day, week, and month searches run automatically. Scheduled scripts call the analysis routines and parse the results for possible detections. The two-hour search generates the signal maps and two-hour background estimates that are used to build the maps for all longer time scales. The search generates an oversampled $2.1^\circ/cos(\delta)$ RA $\times 2.1^\circ$ δ binned map of the sky in event excesses and a corresponding map of significance of the excesses (Figure 7.1) from the signal and background maps. The significance map is searched from $\delta = 0^\circ$ to $\delta = 80^\circ$ for locations with a significance above an alert threshold. The day-long maps are constructed by adding consecutive two-hour signal and background maps together and examining the resulting significance map. Week-long maps are the additions of day-long signal and background maps and month-long maps are the addition of week-long maps.

The standard analysis cuts discussed in Chapter 5 are used to generate the two-hour signal and background maps with the exception of the gamma-hadron separation cut used during the first two epochs of the real-time search. Initially, a multi-parameter model fit based on the parameters used to calculate X2 was used. This was later switched to X2>2.5 and is not consistent throughout the two-year period. The difference in sensitivity, however, is not large. For the two-hour time scale only, the alert locations are required to have an average zenith angle less than 45°. As noted in Chapter 6, Milagro has very little sensitivity at zenith angles beyond this value. The cut insures that alert locations have sufficient exposure to be interesting.

Once a possible detection is found, an e-mail is generated with the position and statistical details from the search. Depending on the probability that the detection is a fluctuation of the background, the alert may be sent only to the search manager, or for lower probabilities, to the Milagro internal alert list. If the probability is very low, a notice can be sent to the broader community. The results presented here have been compiled from log and database information kept for each map and alert.

The two-hour search is scheduled to run every three hours on all available data not already included in existing maps. The search builds all possible two-hour maps and buffers leftover events until more data is available. Some care must be taken to insure that no event is counted more than once. Data files are removed from the analysis area once they have been included in a map. Within this scheme, the longest an event is kept before being analyzed is five hours during normal operation.

The day-long search operates once a day. Shortly after 0 UT, the maps for the previous day and the previous day offset by 12 hours are built and searched for signals. Any alerts are available within 4 hours of the end of the standard day map or within 16 hours of the end of the offset day map. Similarly, the week maps are generated once a week and the month maps are generated in the first several days of the following month. The most recent maps and corresponding distributions of significance are posted to an internal website. After each repair of the detector, a

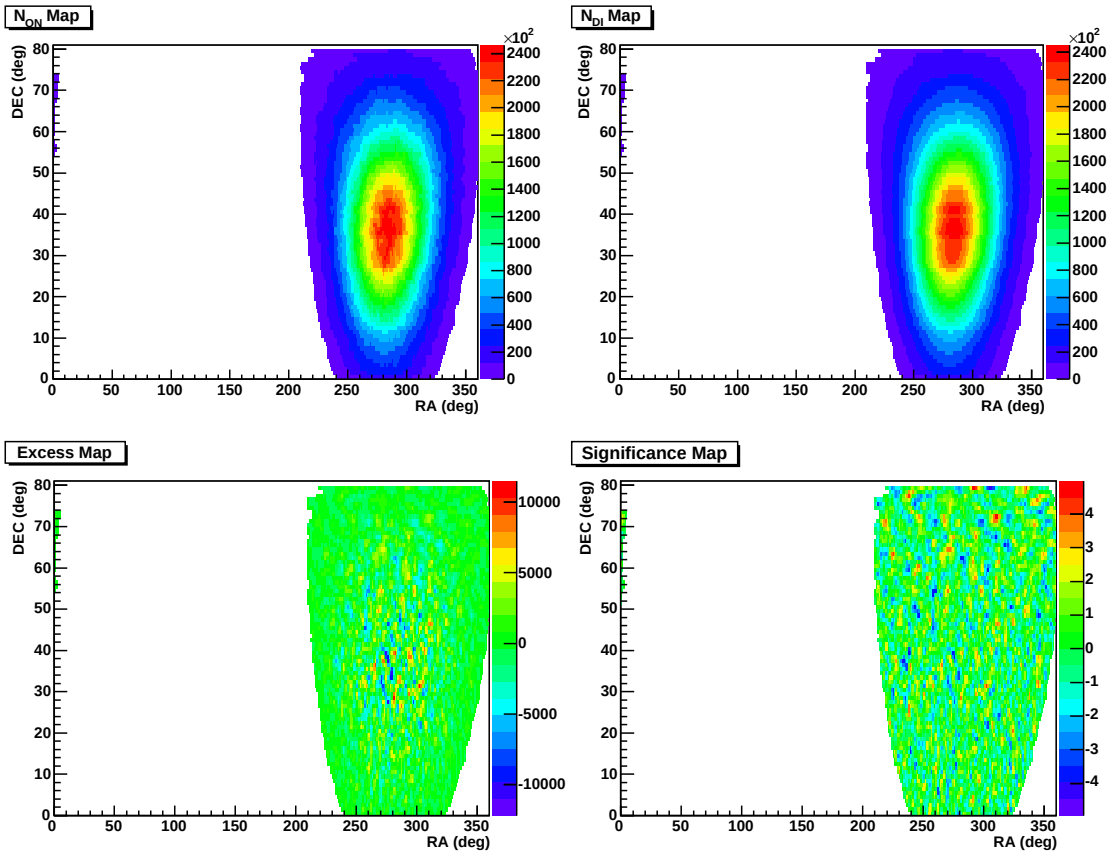

Figure 7.1: Sky maps of signal counts, N_{ON}, raw background, N_{DI}, excess, $N_{ON} - N_{DI}$, and significance of the excess, defined in Equation 7.3, for two hours of data.

longer map is kept and updated every week to track any changes in the signal from the Crab Nebula as a check of the analysis. The relatively small size of the maps (<13 MB) makes it possible to archive the analyzed sky maps for each time scale. The statistics for each map and the possible detections at probabilities $< 7.9 \times 10^{-7}$ ($> 4.8\sigma$) are recorded in a MySQL database. Using the database any alerts can be referenced or re-evaluated by analyzing the same data or examining the original maps. This also makes it possible to search for variations in the search and potential correlations of alerts with detector conditions.

7.3 Calculation of Significance

The observed signal counts in each bin are compared to the background estimation to determine whether a particular location and time is sufficiently interesting to justify notification. The statistical test of the signal counts is made assuming the null hypothesis. The excess (or deficit) counts are tested for consistency with a normally distributed background. Each bin in a map of the excess is given a probability for being a fluctuation of the background estimate. Locations observed for two hours or

more have enough background counts to allow the use of Gaussian statistics. The Gaussian distribution is

$$P(x|\mu) = \frac{1}{\sqrt{2\pi}\sigma} e^{-[\frac{(x-\mu)^2}{2\sigma^2}]}$$

where x is the measured event excess, μ is the mean, and σ is the standard deviation. The significance is defined as the number of standard deviations away from the mean the measurement occurs. The null hypothesis implies that the distribution of significance for all the bins in the map should be a Gaussian with a $\mu = 0$ and RMS $= 1$ in the absence of a signal.

The distribution of significance provides a check of the background estimation. Divergence from the background expectation indicates a signal, or a bias in the calculation of significance or of the background estimate. A gamma-ray signal appears as bins inconsistent with the expected distribution, as visible in Figure 7.2. There are two detected signals in the map of the data set examined in Chapter 8, the Crab Nebula and Mrk 421, but when removed, the distribution closely matches the normal distribution expected for measurements of the background. This indicates an absence of additional detectable signals and a consistency of the background estimation with expectations.

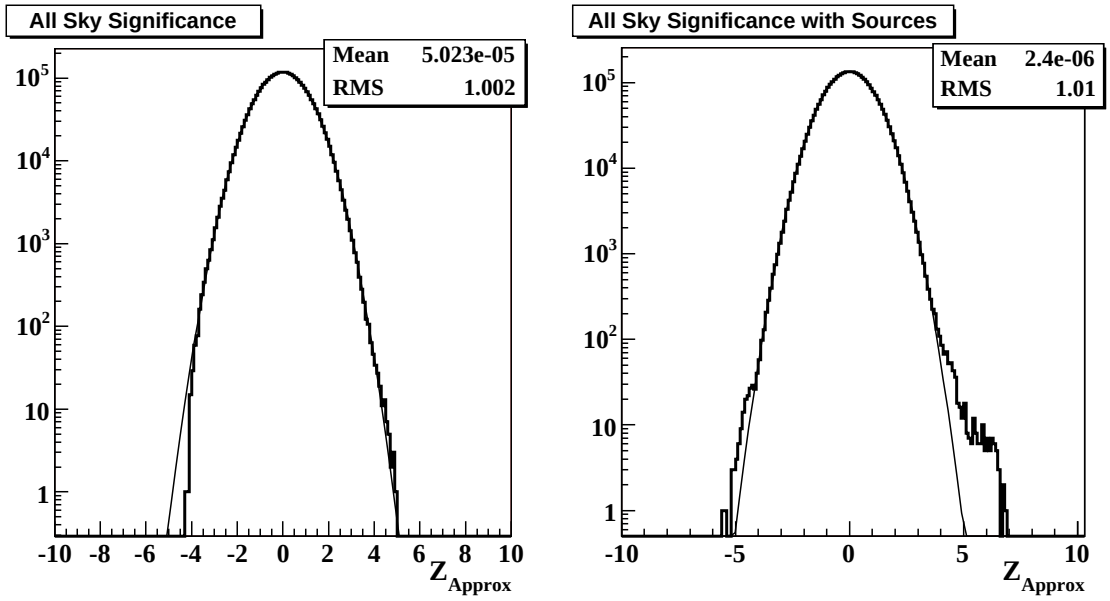

Figure 7.2: Distributions of the significance of the excess (or deficit) for each bin in a sky map. The Gaussian fit to each distribution is shown. The map on the left has source regions excluded. The map on the right includes bins with gamma-ray signals from the Crab Nebula and Mrk 421. These bins are inconsistent with the background hypothesis and diverge from the Gaussian shape at the high significance end.

A simple approximation for calculating the Gaussian significance is

$$\frac{N_{ON} - N_{OFF}}{\sqrt{N_{OFF}}}$$

where N_{ON} represents the signal counts and N_{OFF} represents the background counts. A more accurate calculation is provided by Li & Ma (1983). This method assumes that separate measurements are made of the signal level and background levels. In Milagro data, as discussed in Chapter 5, the signal and background are observed simultaneously. Some care is required to determine the ratio of time spent observing the source to time spent observing the background, which is a parameter in the Li & Ma (1983) calculation.

The ratio of time spent taking data on source, T_{ON}, to time off source, T_{OFF}, can be considered equivalently in spatial terms. A full two-hour background estimate encompasses a band of sky in declination with a width in RA of $w_{bkg} = 30°$. The width of a signal bin in RA, $w_{sig} = 2.1°/\cos\delta$, changes with declination to keep the bin area constant. Excluding w_{sig} from the width of the band used to estimate the background gives the ratio

$$\alpha_{LM} = \frac{T_{ON}}{T_{OFF}} = \frac{w_{sig}}{w_{bkg} - w_{sig}}. \tag{7.1}$$

The direct integration estimate includes the observation of the signal bin in the background estimate for that bin. To remove the effect of signal counts from the background estimate, the width of sky contributing the signal is removed from the width in which the background counts are collected. The ratio of widths indicates the fraction of signal counts in the total background. The background estimate in the bin of interest is expanded using the ratio to produce the total background counts used in the estimate,

$$\frac{w_{bkg}}{w_{sig}} N_{DI} = \frac{(1+\alpha)}{\alpha} N_{DI},$$

where N_{DI} represents the background counts given in a bin by direct integration. The signal counts are removed from the total background counts used in the estimate and the corrected total background number is rescaled to the background expected in the bin of interest.

$$N_{OFF} = (1 + \alpha_{LM}) N_{DI} - \alpha_{LM} N_{ON} \tag{7.2}$$

This is the background estimate appropriate for calculating the excess and the significance of the excess.

The significance can be obtained most accurately from Equation 17 of Li & Ma (1983). The values for the exposure ratio α_{LM} from Equation 7.1, and the corrected background estimate from Equation 7.2 are appropriate for this formulation. The Li and Ma formulation is a likelihood ratio and can become cumbersome for repeated calculations. For this reason, an approximation is used instead to calculate the significance of the excess in each bin of the search maps. The approximation modifies the simple Gaussian formula by including fluctuation level of the background in addition to the error in knowledge of the background.

$$Z_{approx} = \frac{N_{ON} - N_{DI}}{\sqrt{\alpha N_{DI} + N_{DI}}} \tag{7.3}$$

This approximation is within 4% of Equation 17 from Li & Ma (1983) for bins with $N_{DI} \geq 500$. It only causes large errors for two-hour maps and short day maps,

which have low population bins. For any full duration day map $N_{DI} \gg 500$, and the approximation is good.

7.4 Calculation of Annual Rates

The online all-sky search tests many places and times for a signal. This means that the probability that the excess in a bin is a background fluctuation must be adjusted to account for the number of independent searches conducted. To put the significance of an alert into perspective given the large number of searches, an estimate for the annual rate of alerts expected for a given probability threshold is calculated. The estimate allows alerts expected a few times a year or more to be distinguished from those expected much less frequently.

The number of independent searches, the trials factor, can be broken into searches in space and searches in time. The number of searches in time is well known. If none of the maps overlap in time, then the time trials factor is the number of maps. For all but the day search this is the case. The day search includes a factor of two in oversampling because the maps are offset by 12 hours.

The spatial bins in the sky maps are heavily oversampled. A $2.1^\circ/cos(\delta) \times 2.1^\circ$ bin is searched every $0.1^\circ \times 0.1^\circ$ of sky. The online maps are searched from 0° to 80° in δ meaning that $800 \times 3600 = 2.88 \times 10^6$ bins are searched in maps with durations longer than a sidereal day. The number of bins searched is less by about 1/4 for two-hour maps. The overlapping search bins are highly correlated and should not all be considered independent. Some smaller number better represents the spatial trials factor. The minimum number of spatial trials is the number of independent bins that can be fit on the sky. For maps longer than a sidereal day, 4600 non-overlapping bins can be fit into the search area. The actual trials factor falls between the minimum and maximum bounds.

The observed trials factor can be measured using the probabilities of generated alerts.

$$annual\ rate = N_{Trials} P,$$

where the annual rate is the number of alerts expected in a year due to fluctuations of the background with a probability of being background $< P$. For example, the two hour search generated 384 alerts with $P < 2.87 \times 10^{-7}$ ($> 5\sigma$) in 2.13 years. Assuming all of those are background fluctuations the expectation for alerts above this level in a single year is 180. That implies that $N_{Trials} = 6.3 \times 10^8$ when averaged over the entire period of data that has been searched.

The distinction between a time-averaged and map specific trials factor is only important for the two-hour search. Changes in the calibrations, analysis, or trigger conditions that change the number of events passing the analysis cuts alter the number of trials by expanding the number of independent spatial bins. The two-hour search includes a cut on the minimum number of background events in a bin in order for that bin to be included in the significance map. This cut causes the size of the visible sky to vary. The number of spatial trials should remain constant for maps longer than a sidereal day which include the full area of visible sky. Figure 7.3

demonstrates the relationship of the trials factor and the various time scales. The number of bins at $log10(P) = -1$ is noticeably different for the two hour search, but very similar for the others.

Taking N_{Trials} and removing the factor due to time trials, leaves an estimate of the independent spatial bins. For the two-hour search the number of maps examined in a year is ∼4000 and implies that the spatial trials factor is $\sim 1.6 \times 10^5$. When the same exercise is performed using the reported one-day alerts with the overlapping maps excluded, N_{Trials} is 1.93×10^8 assuming 365 day maps in a year. The spatial trials is, thus, 5.3×10^5. This is approximately consistent with the two-hour result. The two-hour search to the edges of the map sees about 1/4 to 1/3 of the sky. The spatial trials for a full map is expected to by ∼3-4 times greater.

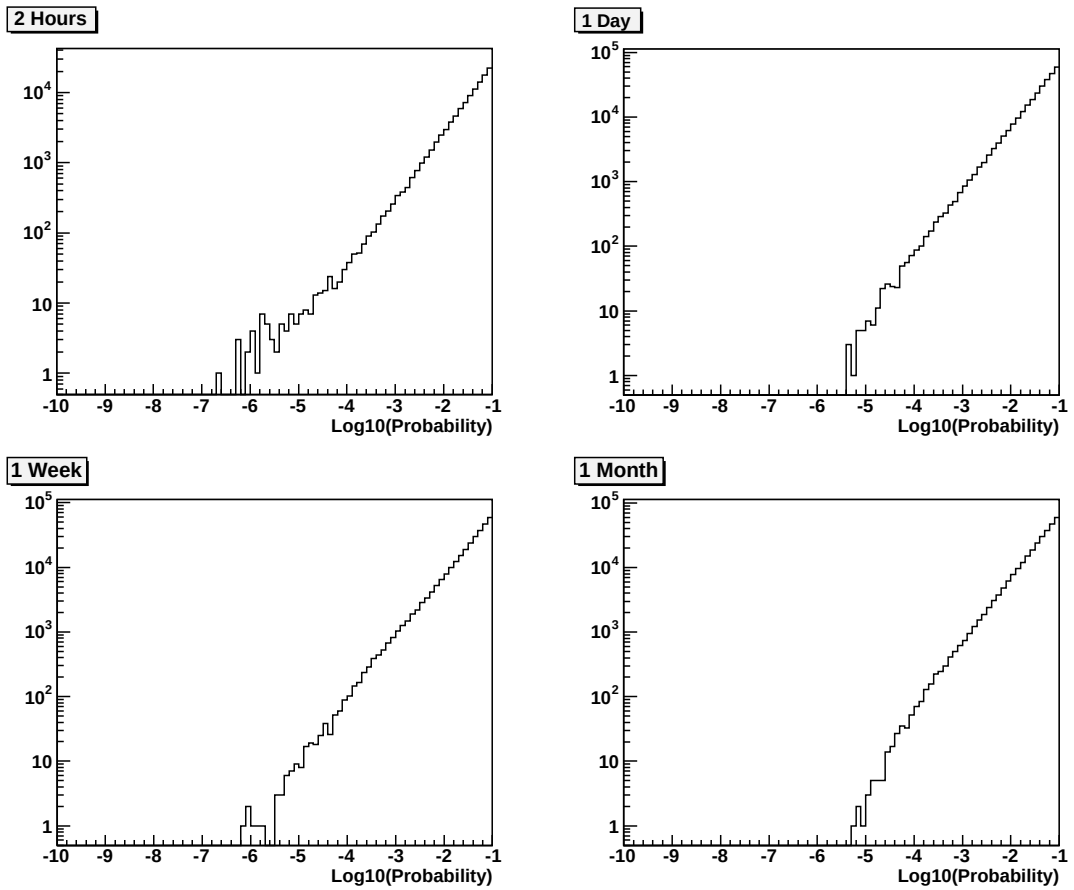

Figure 7.3: Distributions of the probability that the excess is due to a background fluctuation for each bin in maps made for 2 hours, 1 day, 1 week and 1 month. The height of the distribution for the 2 hour map is noticeably different from the others. This is due to the smaller area of sky observed and, therefore, smaller spatial trials factor in the two-hour map.

The annual rate estimates are used to set the notification thresholds for the search. Each search records and communicates alert locations with probabilities exceeding a threshold set to keep the rate of alerts reasonable. The threshold for sending a

Search Duration	Z_{Approx}	Probability	Rate (alerts/yr)
2 Hour	>5.75	$< 4.46 \times 10^{-9}$	27
1 Day	>5.5	$< 1.90 \times 10^{-8}$	27
1 Week	>5.0	$< 2.87 \times 10^{-7}$	19
1 Month	>4.8	$< 7.93 \times 10^{-7}$	1

Table 7.1: Notification thresholds for the two-hour to one-month sky searches. The thresholds are listed in Z_{approx} and the corresponding probability that the alert fits the background hypothesis. The actual rate for each threshold in the two-year alert sample is listed.

two-hour notice is set to keep the rate at a few per month. The threshold for the day search is set to a similar level. The week and month searches have thresholds set to send a few notices per year. The current thresholds are listed in Table 7.1. These have changed slightly over the two years that the search has run. The adjustments were made to bring the alert rates closer to the desired value. The alerts are recorded at a lower threshold to the database to allow studies of the statistics for each search. The two-hour search saves all alerts with $Z_{Approx} > 5$ ($P < 2.87 \times 10^{-7}$). The longer searches save all alerts with $Z_{Approx} > 4.8$ ($P < 7.93 \times 10^{-7}$). The one-day long search threshold is set somewhat higher in Z than may be expected to offset the effects of oversampling in time. The result is a reasonable notification rate with alerts sent about every other week.

7.5 Online Diagnostics

The online searches do not have the same level of data filtering as the AGN analysis (see Chapter 5 for details). To catch any severe irregularities in the data or the search routines several simple checks are made. Data should be continuous except where there is a break in the run number sequence. A new run number occurs at the change in day or when data acquisition is stopped and restarted. A gap in the sequence of subrun numbers indicates a loss of data. Either the subrun was not read or none of the events contained in the sub run passed the analysis cuts. The first situation indicates problems with network communications or data storage. The second could indicate a problem with the position of the GPS antenna or other miscellaneous problems that affect the reconstructed event information. If a gap in the subrun sequence is encountered, the search manager is notified. Problems of this nature are remedied quickly to keep the search up to date with the incoming data.

If the passing event rate in the two-hour search drops too low, there may be a problem with the online reconstruction or data storage. For example, high dead time, problems with the GPS antenna, and problems with transferring data all cause a lower than normal passing event rate in the search. The search manager is notified automatically of any irregularities in the rate, or discontinuities in the data that are not correlated to known stops in the data acquisition.

More subtle changes in the detector configuration or running conditions can cause longer term effects in the search. To check for systematics, a series of diagnostic plots are generated for the recorded alerts over large periods of time. The checks look for any strong correlations in time or location of the alerts that cannot be explained by known effects in the data. For example, a power outage may cause a significant portion of the muon layer PMTs to be inoperative during data taken shortly after power is restored. Such a change in the bottom layer causes a very different X2 distribution. A small number of alerts in the two-hour search are coincident with large-scale PMT outages. The longer searches are typically not affected because the change in the distribution is for a much smaller percentage of events in the map.

Occasionally, the trigger threshold is changed for a short period of time to allow a special data set to be taken. Changes in the event rate affect the trials factor in the two-hour maps and the sensitivity of the detector. The last several situations are documented in log book entries and records of DAQ parameters. It is additional unknown effects that may be discovered by monitoring the recorded alerts.

To check that the search does not have a spatial bias, maps in equatorial coordinates are made for the entire set of recorded alerts. The expectation is that this map should be uniform in RA and DEC. It is also noted that the examination of alert maps may indicate repeated activity in the same region of sky due to a real signal. The alert maps are divided into two-hour alerts and all other alerts since the trials for the two-hour maps are appreciably different and more susceptible to changes in the detector as discussed previously. The locations of two-hour alerts in the last two years are shown in Figure 7.4. The locations of alerts from the other searches are shown in Figure 7.5. Neither map shows a strong bias in location. To check for bias due to the background estimation, the distribution in RA is shown for both sets of alerts. To check for biases due to angle dependence in the trials factor, the distribution of alerts in DEC is shown. All the alerts selected for these distributions have a significance above a threshold (5σ for two-hour alerts, 4.8σ for all others) with significance calculated using the Li and Ma Equation 17 formulation (Li & Ma, 1983).

The distribution of alerts over time is examined to check for any seasonal dependence or any negative effects due to upgrades of the search software. No significant effects are found. Several of the more prominent locations are associated with abnormal data or detector conditions that caused several alerts at the same location in subsequent two-hour maps.

7.6 Results of Online Search

Results are presented for the real-time searches of data taken between 27 February 2002 and 16 April 2004 (MJD 52332-53111). The exposure for 779 days of data is 712.45 days, or 91.6%. The percentage of live time is slightly higher than that of the AGN analysis because the bad run and short map cuts are not applied to the real time analysis. The longer maps are constructed from archived data and have slightly different end points from the real-time searches. The Epoch I map includes

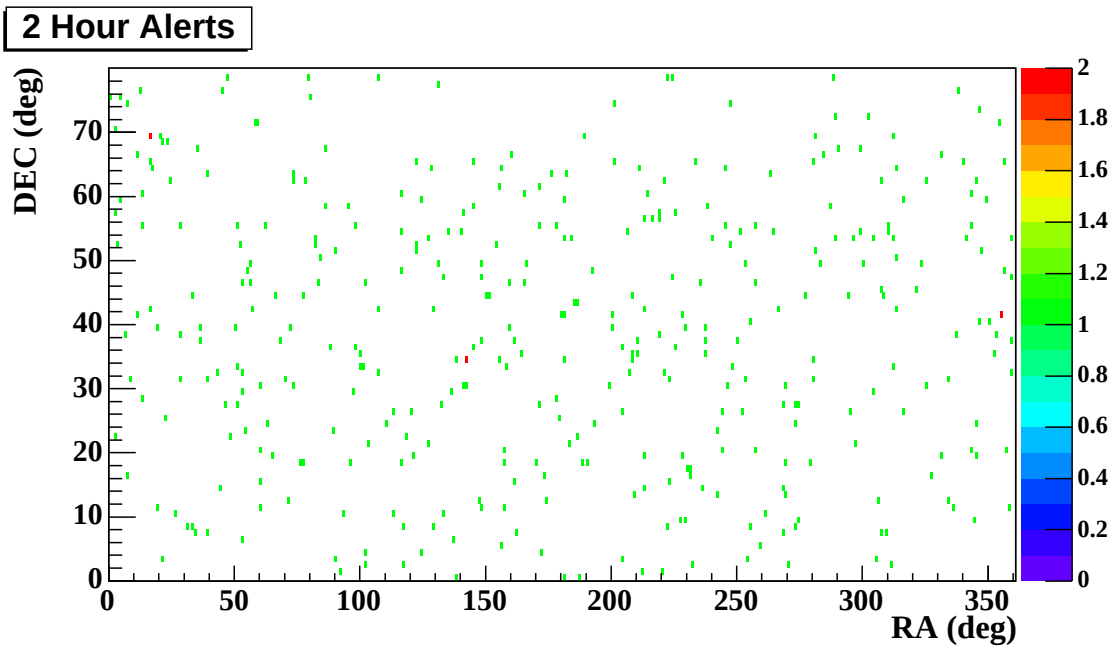

Figure 7.4: Locations of alerts from the 2 hour search with Z_{LM} >5 are shown in equatorial coordinates.

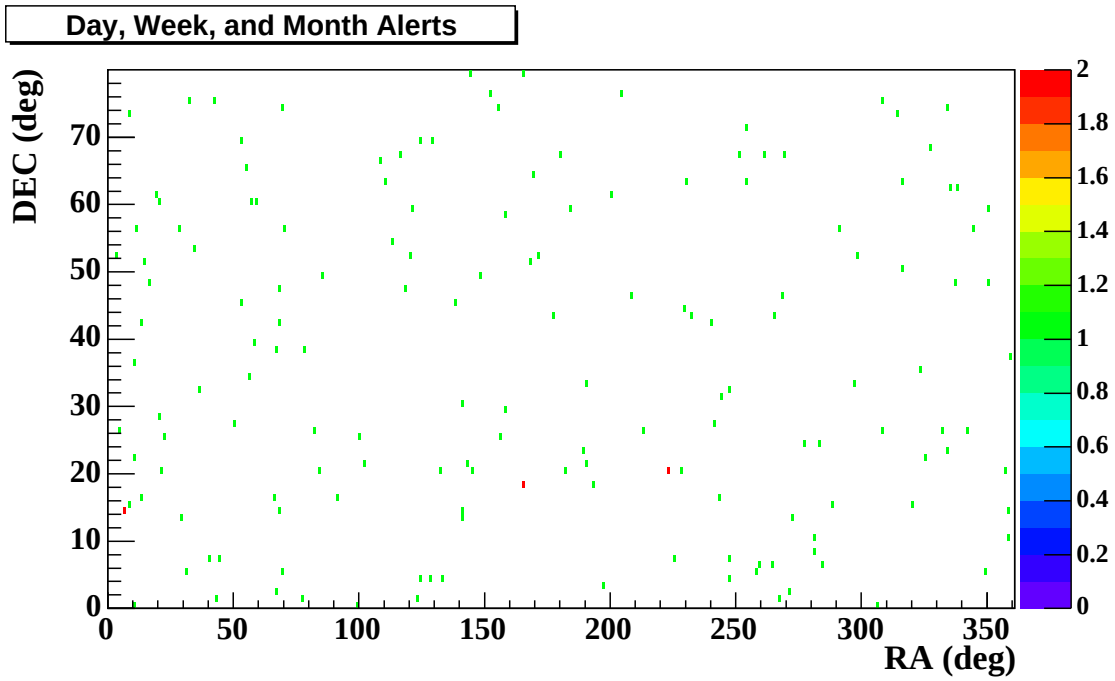

Figure 7.5: Locations of alerts from the day, week, and month searches above the threshold, Z_{LM} >4.8, are shown in equatorial coordinates.

some data before the real-time database was operational and begins on 6 February 2002. The epoch maps are constructed by the week from archived data making the end date for the most recent map 28 March 2004. This is earlier than the date of

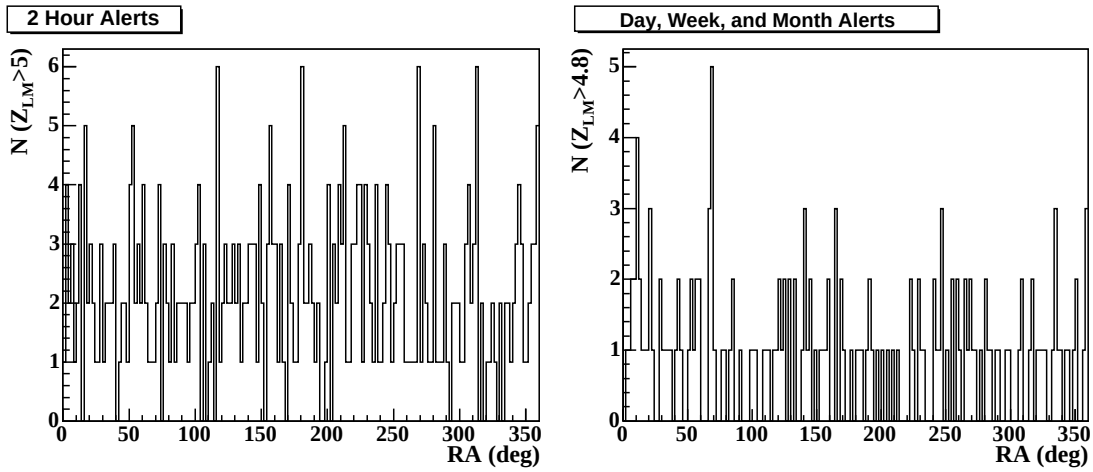

Figure 7.6: Distribution of alerts from searches in right ascension (RA).

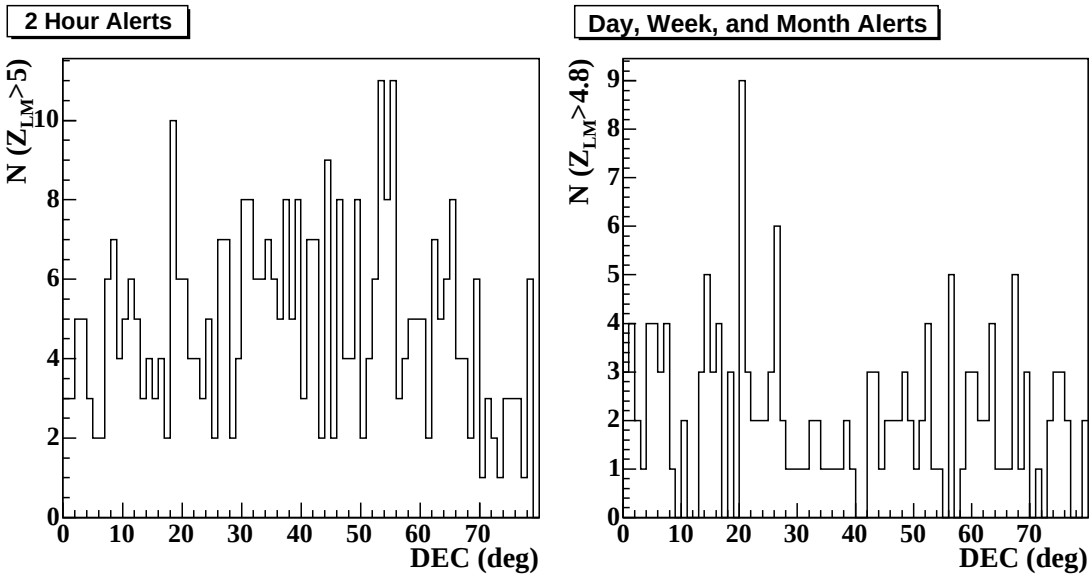

Figure 7.7: Distribution of alerts from searches in declination (DEC).

the most recently available database statistics from the real-time search. The most significant locations for each search are listed in Tables 7.3, 7.4, 7.5, 7.6, and 7.8 and summarized by Figures 7.11 and 7.12.

The primary goal of the search is to allow the earliest possible notification of transient activity. The search analysis has been updated over the two-year period discussed here, as have the reconstruction routines. For this reason, the results from the real time analysis for the shorter maps lack improvements that can be made by a current analysis of the same data. The transitory nature of this analysis suggests that all-sky limits should be left to a more current analysis of the data that includes the best methods and filters. Additionally, stable running of the searches was not reached until the Milagro detector had been operating for more than a year. It

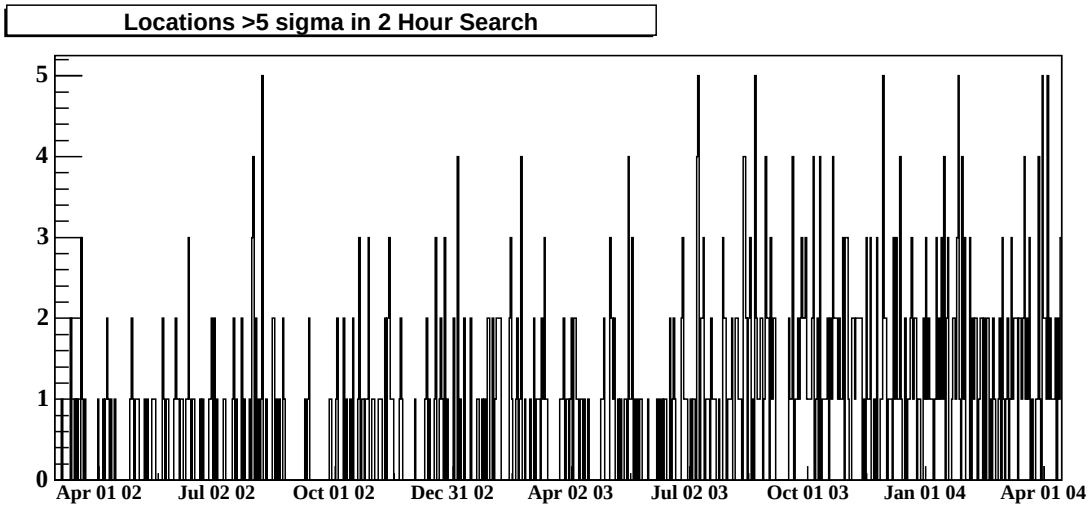

Figure 7.8: Time distribution of two-hour alerts with $Z_{LM} > 5$ from 27 February 2002 to 16 April 2004.

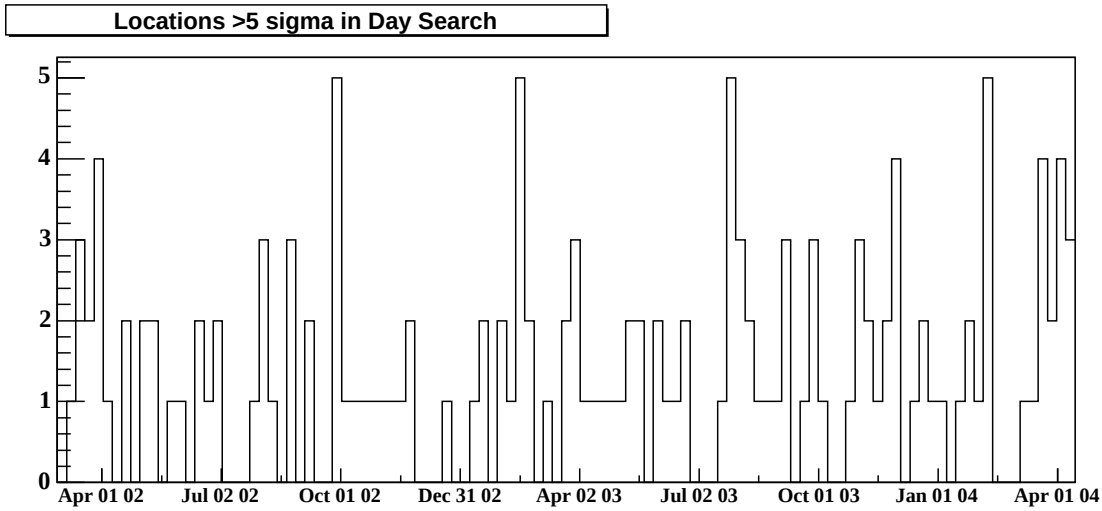

Figure 7.9: Time distribution of one-day alerts with $Z_{LM} > 4.8$ from 27 February 2002 to 16 April 2004.

should be noted that the data set presented here is not the full set of data available for analysis. See Atkins et al. (2004b) for the all-sky flux limits for the full data set.

Although this analysis is not appropriate for evaluating all-sky limits, something can be said about the fluxes corresponding to the alerts and the sensitivity level of the searches. A search specific flux limit is deduced for each time scale. The estimated flux corresponding to each alert generated enables a measurement of the effective sensitivity of the online searches. The results indicate the level of signal detectable in the various searches. The flux threshold is estimated from the observed alerts and, thus, includes the effects experimental trials. The trials factor raises the

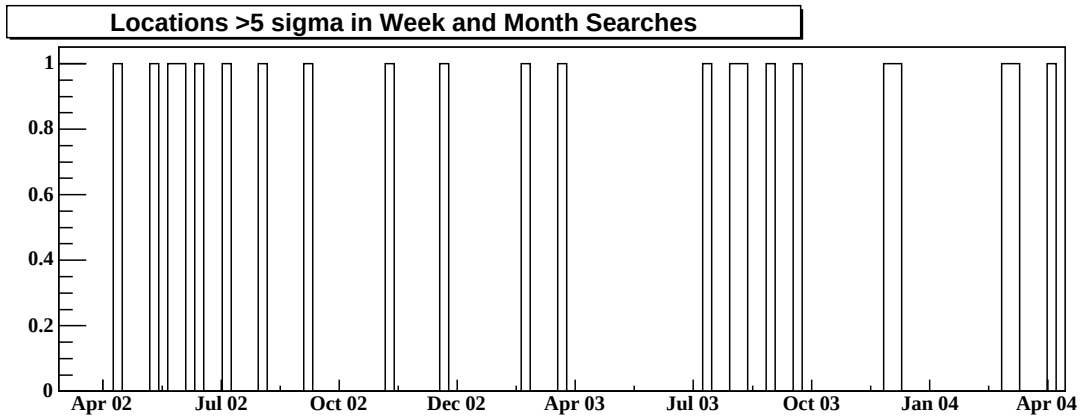

Figure 7.10: Time distributions of week and month alerts with $Z_{LM} > 5$ from 27 February 2002 to 16 April 2004.

flux amplitude necessary for a detection in relation to the point source sensitivities presented in Chapter 6. These search sensitivities are summarized in terms of the Crab flux at 4 TeV in Table 7.7. This is a very rough estimate and can only approximately represent all possible photon spectra and locations in the field of view. It is meant only to give the order of magnitude of the detectable threshold. The observed alerts above a threshold are also compared with the expectation from background fluctuations. The discrepancies are not large and reflect the uncertainty in the estimate of the trials factor.

Changes in the search require a second analysis of the reconstructed data for results covering the period of a year or more. Epochs of the online search are defined by the occurrence of the annual fall PMT repairs, which change the configuration of the detector and necessitate new timing and PE calibrations. See Table 7.2 for defined epochs. Periods between repairs have the same physical configuration and allow monitoring of any change in source sensitivity due to repairs or calibrations applied during that epoch. Within the data included here, mid-year changes in the detector pointing and gamma-hadron separation parameter make the addition of the maps generated online undesirable. A second analysis of archived data produces maps that can be added without a loss of point source sensitivity. The epoch maps shown here are generated using a second analysis of the data. When the original maps from the online search are combined, the Crab Nebula is still visible, but at a reduced significance. The transient source Mrk 421 is not as strongly affected due to flares falling in time periods in which the online maps are more compatible. This implies that the shorter maps are not as strongly affected. Table 7.10 lists the durations and approximate sensitivities of the epoch maps and the combined map containing all data taken during the operation of the real-time search up to 28 March 2004.

Epoch	UT Start	UT Stop	MJD Start	MJD Stop
Epoch I	2002-02-06	2002-09-15	52310	52532
Epoch II	2002-09-24	2003-09-07	52541	52889
Epoch III	2003-09-16	2004-03-28	52898	53092

Table 7.2: Online search epochs defined by the beginning of the search and PMT repairs.

Position		Time (UT)		Significance	Annual Rate
RA	DEC	Start	Stop	Z_{LM}	
304.7	29.7	2002-10-27 03:15	2002-10-27 05:17	6.036	0.5
141.8	30.3	2002-08-06 19:10	2002-08-06 21:14	5.920	1.0
24.6	62.7	2002-07-21 15:36	2002-07-21 17:40	5.900	1.2
71.5	12.8	2003-01-31 04:13	2003-01-31 06:13	5.892	1.2
219.3	56.3	2003-03-08 11:12	2003-03-08 13:14	5.854	1.5
310.2	54.2	2002-04-14 13:15	2002-04-14 15:17	5.846	1.6
19.6	11.8	2004-02-27 20:08	2004-02-27 22:11	5.845	1.6
180.5	41.7	2002-12-21 13:02	2002-12-21 15:02	5.809	2.0
281.0	69.2	2003-11-16 18:42	2003-11-16 20:43	5.794	2.2
355.5	41.8	2003-02-22 20:49	2003-02-22 22:50	5.775	2.5
245.2	64.1	2002-10-08 18:22	2002-10-08 20:23	5.773	2.5

Table 7.3: The most significant alerts from the two-hour search over 2.13 years. Z_{LM} is not corrected for the trials factor. The annual rate reflects the inclusion of trials.

Position		Time (UT)		Significance	Annual	I_0
RA	DEC	Start	Stop	Z_{LM}	Rate	10^{-10}
298.5	52.4	2002-08-07 01:23	2002-08-08 00:38	6.307	0.03	5.83
7.2	77.5	2002-06-24 12:27	2002-06-25 12:54	5.914	0.3	26.3
228.2	20.0	2002-04-09 01:41	2002-04-10 00:09	5.834	0.5	6.86
69.3	5.9	2002-10-02 01:34	2002-10-03 00:00	5.817	0.6	12.4
69.5	74.0	2004-03-16 00:23	2004-03-17 00:39	5.768	0.8	15.6
268.8	46.8	2002-03-22 00:55	2002-03-23 01:21	5.766	0.8	5.80
200.3	61.6	2004-01-27 01:23	2004-01-28 01:50	5.747	0.9	7.09
22.0	25.2	2004-03-23 13:33	2004-03-24 13:54	5.677	1.3	4.34
190.5	21.9	2002-03-30 12:14	2002-03-31 12:32	5.666	1.4	6.44
132.0	20.9	2003-07-30 13:28	2003-07-31 13:50	5.644	1.6	6.02

Table 7.4: The most significant alerts from the one-day search over 2.13 years.

Position		Time (UT)		Significance	Annual	I_0
RA	DEC	Start	Stop	Z_{LM}	Rate	10^{-10}
141.9	14.3	2002-11-10 00:22	2002-11-18 19:53	6.276	0.005	3.82
113.9	54.6	2004-03-07 00:42	2004-03-14 01:30	5.915	0.05	1.74
316.5	50.5	2002-09-04 21:40	2002-09-08 00:45	5.848	0.1	2.84
138.7	45.9	2003-12-07 00:53	2003-12-14 01:15	5.642	0.2	1.81
156.2	25.1	2002-04-14 01:02	2002-04-21 00:24	5.486	0.6	1.75
11.4	56.2	2004-04-04 00:22	2004-04-11 01:59	5.466	0.6	1.82
254.2	71.5	2002-12-22 01:12	2002-12-29 00:06	5.257	2.0	8.15
120.6	52.9	2003-08-31 01:39	2003-09-07 01:00	5.247	2.1	2.04
57.9	60.3	2003-07-13 01:38	2003-07-20 00:02	5.247	2.1	2.54
10.7	22.1	2003-02-23 00:51	2003-03-02 01:20	5.178	3.1	2.40

Table 7.5: The most significant alerts from the one-week search over 2.13 years.

Position		Time (UT)		Significance	Annual	I_0
RA	DEC	Start	Stop	Z_{LM}	Rate	10^{-10}
43.3	1.9	2004-02-29 00:37	2004-03-28 01:09	5.07	1.3	1.74
133.2	4.8	2002-06-02 00:56	2002-06-30 00:08	4.91	2.9	1.84

Table 7.6: The most significant alerts from the 1 month search over 2.13 years.

Search Duration	Threshold	Sensitivity	Observed	Expected
2 Hour	$>5.75\sigma$	$\gg$30 Crab	10$>5.77\sigma$	5.3
1 Day	$>5.50\sigma$	>30 Crab	10$>5.64\sigma$	5.8
1 Week	$>5.00\sigma$	>10 Crab	10$>5.17\sigma$	6.3
1 Month	$>4.80\sigma$	>5 Crab	2$>4.80\sigma$	6.2

Table 7.7: Summary of estimated sensitivities for each time scale. The threshold of the search in terms of significance is given, but the flux threshold varies over the field of view. A typical flux is given in Crab units using the collected alerts. The number of alerts above a selected significance is compared with the number of alerts expected from background fluctuations above that significance. The selected significance for the month search is limited to 4.8σ because information about alerts below this level were not saved.

Position		Significance	Flux I_0
RA	DEC	Z_{LM}	10^{-11} $phot/cm^2$ s TeV
Epoch I: 2002-02-06 to 2002-09-15			
230.9	27.0	5.07	3.3
35.5	14.6	4.63	4.0
304.6	28.9	4.60	2.9
253.5	59.2	4.40	3.5
152.4	59.8	4.25	3.5
251.0	48.1	4.18	2.4
75.9	4.0	4.11	7.3
327.5	22.2	4.10	2.9
309.6	49.8	4.09	2.5
207.0	16.3	4.08	3.6
319.5	43.8	4.07	2.4
141.5	10.3	4.05	4.7
256.1	76.6	4.03	12.9
Epoch II: 2002-09-24 to 2003-09-07			
273.4	74.8	4.68	7.7
299.8	28.4	4.57	2.2
335.4	17.8	4.37	2.4
304.0	14.3	4.34	3.0
139.5	46.7	4.20	1.9
261.7	14.7	4.20	2.5
43.7	41.7	4.12	1.8
56.0	1.0	4.07	6.2
255.3	2.1	4.04	5.3
Epoch III: 2003-09-16 to 2004-03-28			
183.90	1.40	4.36	9.2
122.00	35.30	4.25	2.4
67.30	28.10	4.16	2.5
57.20	78.30	4.13	16.2
124.20	57.10	4.13	2.9
79.50	24.60	4.09	2.5
153.90	59.30	4.06	3.0
164.40	69.90	4.03	5.4
274.90	20.10	4.00	2.8

Table 7.8: Locations with significance $Z_{Approx} > 4$, in 3 periods bounded by the beginning of the online search, annual detector repairs, and the present time. The first epoch is 7 months long; the second, 1 year; and the third, 6 months. The Crab Nebula and Mrk 421 locations have been excluded from the lists.

Position		Significance	Flux I_0
RA	DEC	Z_{LM}	10^{-11} $phot/cm^2$ s TeV
153.80	59.50	4.67	2.01
356.00	17.90	4.56	1.85
41.00	34.80	4.41	1.40
261.50	14.70	4.34	1.95
12.20	15.70	4.33	1.97
14.30	43.90	4.33	1.35
80.50	26.70	4.31	1.47
115.10	23.30	4.29	1.51
184.40	72.80	4.20	3.66
300.30	28.40	4.16	1.43
16.00	31.60	4.10	1.32
142.70	33.60	4.10	1.29
209.20	19.40	4.06	1.66
328.20	21.20	4.06	1.45
354.80	13.80	4.06	2.02
17.40	20.90	4.04	1.54
154.10	62.70	4.04	2.06

Table 7.9: Locations with significance $Z_{Approx} > 4$, in two years of data, MJD 52310-53092. The Crab Nebula and Mrk 421 are at the first and second most significant locations and have been excluded from this list.

Epoch	Duration	N>4σ	Sensitivity
Epoch I	222 days	13	~ 1.6 $Crab$
Epoch II	348 days	9	~ 1.0 $Crab$
Epoch III	208 days	9	~ 1.3 $Crab$
Combined	782 days	17	~ 0.8 $Crab$

Table 7.10: Approximate sensitivities for the search in each data epoch and the combined data set. The exposure is given for each period. The number of positions with significance exceeding 4σ is given with the approximate sensitivity of that threshold in Crab units.

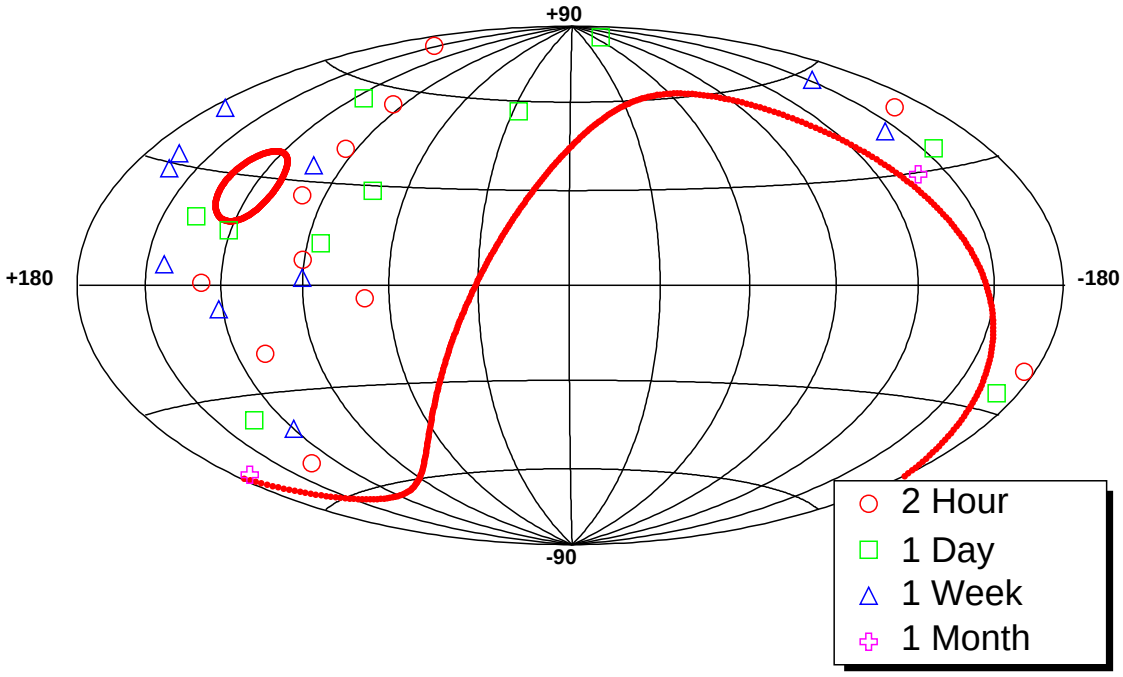

Figure 7.11: Locations in galactic coordinates of the most significant alerts between MJD 52332 and 53111. The boundaries of the search at DEC=0° and DEC=80° are marked by the red lines.

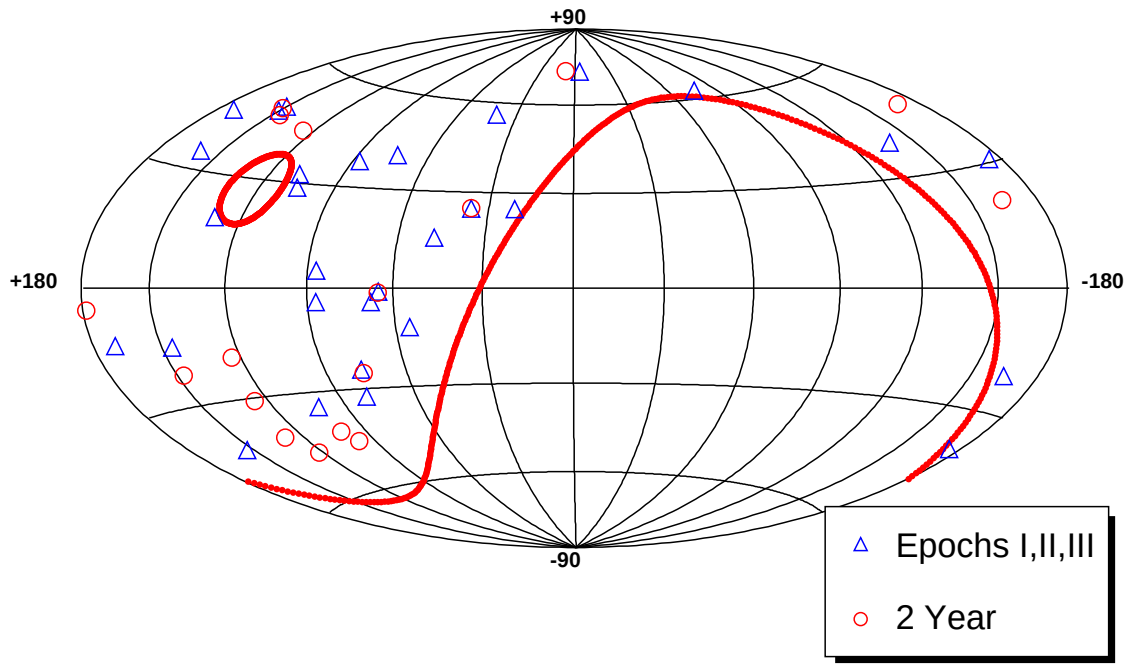

Figure 7.12: Locations in galactic coordinates of the most significant locations in the online search for Epoch I,II,and III and the entire 2.14 data set for MJD 52310 - 53092. The boundaries of the search at DEC=0° and DEC=80° are marked by the red lines.

Chapter 8

Results of Search for Candidate BL Lacs

The qualities that make Milagro a good instrument for all-sky searches also apply to monitoring specific sources for transient emission. The AGN Mrk 421 has been detected by Milagro at 4.1σ in the full data set and at higher significance during observations corresponding to flaring episodes. The large field of view and high duty cycle provide a wide range of time-integrated observations that can be optimized for sensitivity to different flare durations. Milagro conducts extensive short-term and long-term monitoring of the overhead sky. In addition to the all-sky monitoring, specific sources are targeted by more sensitive tests for transient behavior. Flaring from these sources may be present, but fall below the sensitivity of the online transient search. The archival data is used instead to apply a more refined analysis that is extended to include data taken before the online transient search began to run. The selected sample members are interesting because of their potential for TeV emission and existing theoretical modeling of their spectral energy distributions (SEDs).

The TeV candidates are 27 X-ray-selected BL Lacs chosen from a sample in Costamante & Ghisellini (2002). The candidates have predictions for the integral flux above 1 TeV expected from two spectral models given the available multiwavelength data. The sample is described in Chapter 2 (Table 2.2) and previous observations of these objects by other TeV instruments are summarized there. The appeal of this sample lies in the similarities between the selected BL Lacs and detected TeV sources. None of the candidate objects has a significant detection in this data set. The flux upper limits are set and compared to the predicted fluxes. The limits do not constrain any of the predictions of the SSC model. Additional flux predictions from the blazar parametrization of Fossati modified by Costamante (Fossati et al., 1998; Costamante & Ghisellini, 2002) are constrained for several objects. These predictions do not include the effects of attenuation of TeV photons on extragalactic background light (EBL), which could reduce the expected flux below levels to which Milagro is sensitive. To account for this effect, the Milagro flux limits are also calculated to include attenuation effects from the EBL.

A 2.7 year period of Milagro observations is divided into smaller, overlapping time bins to constrain flaring activity on multiple time scales. Only one of the selected BL Lacs has been detected by IACTs. Although many have been the subject of other observations, several do not have previously existing upper limits on the TeV flux. To provide upper limits that are useful for constraining emission models,

the limits for each candidate are presented for two assumed power-law spectra with and without including the effects of IR attenuation. These general limits are given in addition to the limits set using the predicted spectra from Costamante & Ghisellini (2002) Limits without attenuation are appropriate for comparison with model predictions that already include EBL attenuation effects. The inclusion of attenuation addresses the observed curvature in measured spectra of AGN detected at TeV energies (Samuelson et al., 1998; Krennrich et al., 1999; Aharonian et al., 1999, 2002b). The attenuated limits remove the estimated effects of extragalactic photon populations and are appropriate for comparison with emission models that do not include EBL attenuation. Other forms of attenuation are possible but unknown and will require further spectral measurements to be determined.

The TeV spectral shapes are unknown for the candidates with the exception of 1ES 1959+650 which has been detected in a flaring state by IACTs (Aharonian et al., 2003a; Holder et al., 2003). In the absence of a spectral measurement, the flux limits are calculated using two different spectral indexes in a power-law approximation. IACTs have measured AGN spectra and fit power laws with indexes ranging from ~ 2.0 to ~ 3.0. These indexes define a rough range for the spectra expected from different AGN or from the same AGN at different flux levels, i.e. the difference between the highest luminosity and lowest luminosity states observed by IACTS (see Aharonian et al. (2003a)). Setting upper limits for both indexes provides an idea of the upper and lower bound on the limit due to the unknown spectral shape. As discussed in Chapter 2, both Mrk 421 and 1ES 1959+650 have exhibited a hardening of the TeV spectrum (higher photon index) with increased luminosity. The correlation between flux level and spectrum observed in these BL Lacs suggests the bounds could also be interpreted as limits for the flaring and quiescent spectra.

8.1 Description of Data Set

The data set used for this analysis begins on 15 December 2000 and ends on 8 September 2003, or MJD 51893 - 52889. The bad run and short run cuts described in Chapter 5 exclude 1% of the available data. The data were analyzed using the standard two-hour direct integration analysis and all the cuts and corrections described in Chapter 5. The cuts include requirements on the number of photomultiplier tubes used to reconstruct the angle (nFit>20) and the gamma-hadron separation cut (X2>2.5). The combination of both cuts retains 5.8% of the 1.58×10^9 events in the data set. A short map cut is applied after the completion of the background analysis. All the two-hour background maps used to create the final observation maps must contain more than 2900 sec (0.8 hrs) of data. This cut removes 44.2 hours (0.2% of the total exposure) of the analyzed maps. The resulting exposure is 906.20 days within a period of 996 days for a 91% duty cycle. The all-sky significance map for this data is shown in Figure 8.1. The brightest locations are coincident with the Crab Nebula and Mrk 421.

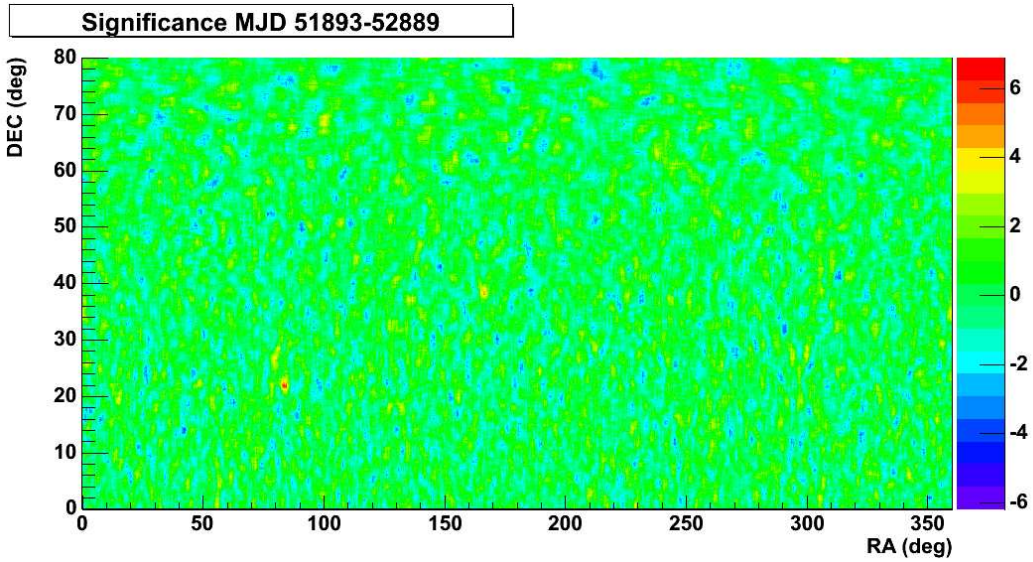

Figure 8.1: All-sky significance map for the full data set examined, MJD 51893 - 52889. The brightest locations are coincident with the Crab Nebula and Mrk 421.

8.1.1 Flux Limits for Steady State Emission

None of the 27 selected BL Lacs have a significant signal in the 906 day Milagro data set. The highest significance for any member of the sample is 2.2σ (0.3σ when the number of searches is taken into account). The flux upper limits for this time period set a limit on the time-integrated TeV emission from the BL Lacs for the entire 2.7 year extent of the search.

The upper limits are placed on the excess number of counts above the background level at the source position using the method of Helene (1983). The 95% confidence level upper limit on the event excess is used to derive the differential flux amplitude necessary to produce that excess in the Milagro detector according to simulations. The calculation requires an assumed photon spectrum at the top of the Earth's atmosphere. It also accounts for the exposure at source location over the time period of the observation. [1] See Chapter 5 for the details of the flux calculation.

The differential photon flux is given the general form

$$dN/dE = I_0(E/TeV)^{-\alpha}e^{-\tau(E,z)}$$

where α is the spectral index, I_0 is the flux amplitude, and τ is the optical depth for photons of energy E from a source at redshift z. The exponential factor is only included for upper limits that assume redshift dependent IR attenuation. Tables 8.1 and 8.2 give the flux amplitude corresponding to the 95% confidence level upper limit on the detected photon excess for each BL Lac. The photon indexes $\alpha = 2.0$ and 3.0 are used. Additionally, the limits are given with and without the inclusion of IR

[1] This is a more precise method than assuming an average daily effective area for the source location.

attenuation in the assumed spectrum. The optical depth, τ, due to IR attenuation is calculated using both the baseline model from de Jager & Stecker (2002) (IR1a) and the LCDM(Salpeter) model from Primack et al. (1999) as parameterized in Bullock (1999)(IR2).

The flux amplitude, I_0, is quoted at the median detected energy predicted in Milagro for the pertinent spectrum and source declination. The median energy is not given for the flux upper limits using IR2 because the model is only parameterized for a few values of redshift. Although the flux amplitude can be interpolated between the calculations for two redshift values, the median energy relationship is more complicated. The limits using IR2 are given to demonstrate the change in I_0 possible for different models the EBL spectrum. Milagro's broad energy response tends to dilute differences in the opacity predictions (Figure 2.5) from these models. The difference in the resulting limits is small compared to the difference between limits with and without any IR attenuation. The largest differences occur for the combination of $\alpha = 2$ and sources that pass further from zenith (the latitude of Milagro is 35.88°) like 1H 0323+022 and RGB 1136+676.

8.1.2 Flux Limits for Transient Emission

BL Lacs are known for variability in all wavelength bands. The BL Lacs detected at TeV energies have shown changes in flux occurring over tens of minutes up to months. To search for flaring activity from the candidate BL Lacs, the Milagro data is broken into consecutive time bins. They are chosen to maximize the significance of a signal by searching enough different time scales to allow one that coincides reasonably well with the duration of a possible flare. For periods less than ∼8 days the flux required for a detection by Milagro becomes unreasonably high considering detected and predicted TeV flaring activity in BL Lacs. There is not a strong motivation to search for transient behavior for time scales less than this when examining specific objects. Any highly significant activity would have been found by the online transient search. In the absence of detections in that search, 8 days provides a reasonable minimum time scale for setting limits.

The time scales are selected to maximize sensitivity to transient emission while keeping the statistical trials factor for the search low. Biller et al. (1994) determines that the optimal time scales to use in a transient search should be related by a factor of 3 or less. This search uses a factor of 2 ratio for the lengths of the time bins. Starting from 8 days the time scales increase by a factor of two up to 256 days. To insure that a time bin is centered on any flaring activity, an additional set of time bins offset by half the duration is searched for each time scale.

The time scale search evaluates the measured photon rate from the 27 BL Lac objects for all maps from each of the six time scales. The search of time scales produced no significant detections of flaring activity from any of the BL Lacs. The highest significance observed was 4.1σ before including statistical trials. The number of independent searches must be included to assess the probability that a signal is consistent with background fluctuations (see Chapter 7 for more discussion). This reduces the significance from 2.1×10^{-5} (4.1σ) to ∼0.05 ($\sim 1\sigma$) and is not a significant

Object	z	I_0 (E_{med}) $[\frac{10^{-11}}{cm^2 s TeV}]$	I_0 IR1a (E_{med})	I_0 IR2
1ES 0033+595	0.086	0.33 (11.8)	7.90 (1.2)	4.36
		1.59 (2.0)	6.51 (0.48)	6.02
1ES 0120+340	0.272	0.34 (7.6)	33.9 (0.32)	38.1
		0.96 (1.3)	8.83 (0.21)	10.2
RGB 0136+391	0.200	0.16 (7.6)	8.66 (0.40)	9.02
		0.46 (1.2)	2.87 (0.26)	3.21
RGB 0214+517	0.049	0.26 (9.1)	1.87 (1.91)	1.19
		0.98 (1.5)	2.23 (0.63)	2.06
3C 66A	0.444	0.33 (7.6)	111.00 (1.26)	128
		0.95 (1.9)	18.70 (0.16)	24.0
1ES 0229+200	0.139	0.49 (8.5)	18.70 (1.55)	13.8
		1.75 (0.6)	9.06 (0.35)	9.2
1H 0323+022	0.147	0.56 (18.6)	81.6 (0.65)	49.3
		4.6 (3.8)	48.30 (0.51)	48.3
1H 0414+009	0.287	0.52 (25.1)	564.00 (0.34)	634
		5.02 (3.9)	194.00 (0.29)	233
1ES 0647+250	0.200	0.16 (7.8)	10.2 (0.41)	10.5
		0.52 (1.3)	3.32 (0.26)	3.7
1ES 0806+524	0.138	0.25 (9.1)	9.86 (0.62)	7.2
		0.92 (1.5)	4.87 (0.35)	4.94
RGB 0812+026	0.200	0.37 (17.0)	122.00 (0.54)	108
		3.05 (3.4)	55.30 (0.40)	62.2
OJ 287	0.306	0.28 (8.5)	57.20 (0.30)	67.5
		1.01 (1.5)	14.30 (0.20)	16.9
1H 1013+498	0.200	0.24 (7.9)	17.4 (0.42)	17.7
		0.83 (1.5)	6.02 (0.28)	6.73

Table 8.1: The 95% c.l. upper limits on I_0, where $dN/dE = I_0(E/TeV)^{-\alpha}e^{-\tau(E,z)}$. The differential flux amplitude, I_0, is quoted at the median detected energy which depends on the assumed spectral shape and the source declination. For each AGN the first row gives limits for $\alpha = 2.0$ and the second for $\alpha = 3.0$. IR1a indicates the baseline evolution IR background model from de Jager & Stecker (2002) and IR2 indicates the semi-analytic model from Primack et al. (1999) as parameterized in Bullock (1999). The IR2 flux limits have been interpolated because the parameterization is course in redshift. The median energies for IR2 are not available for this reason.

detection. Tables 8.3-8.9 list the flux amplitude limits for the highest detected photon rate ($photons/day$) from each BL Lac for each time scale. Each limit sets a bound on the average flux from the source for the specified time scale over the 2.7 year extent of the data set. Some gaps exist in the observations due to repairs and other complications. This only effects coverage for time scales with lengths on the same

Object	z	I_0 (E_{med}) $[\frac{10^{-12}}{cm^2 sTeV}]$	I_0 IR1a (E_{med})	I_0 IR2
1ES 1028+511	0.361	0.15 (8.5)	49.60 (0.26)	56.6
		0.54 (1.5)	11.30 (0.19)	13.2
RGB 1117+202	0.139	0.29 (8.5)	11.20 (0.63)	8.24
		1.05 (1.5)	5.41 (0.35)	5.5
Mrk 180	0.045	0.33 (17.8)	4.48 (3.16)	2.2
		2.6 (3.1)	7.7 (0.76)	6.52
RGB 1136+676	0.135	0.44 (17.0)	51.50 (0.68)	27.8
		3.31 (3.4)	28.7 (0.43)	27.3
ON 325	0.237	0.37 (7.4)	28.60 (0.35)	30.5
		1.07 (1.3)	8.41 (0.23)	9.52
1H 1219+301	0.182	0.50 (7.4)	23.10 (0.46)	21.7
		1.46 (1.3)	8.38 (0.28)	9.09
RGB 1417+257	0.237	0.52 (7.6)	47.10 (0.35)	49.7
		1.65 (1.3)	13.70 (0.22)	15.5
1ES 1440+122	0.162	0.28 (11.2)	24.80 (0.56)	17.9
		1.4 (2.1)	11.30 (0.34)	11.5
1ES 1553+113	0.360	0.28 (11.2)	150.00 (0.23)	173
		1.35 (2.1)	36.20 (0.21)	42.6
RGB 1725+118	0.018	0.57 (11.2)	1.61 (5.50)	1.23
		2.84 (2.1)	4.35 (1.35)	4.05
I Zw 187	0.055	0.12 (8.3)	0.93 (1.74)	0.59
		0.41 (1.5)	0.98 (0.60)	0.91
1ES 1741+196	0.084	0.46 (8.5)	7.26 (1.10)	4.67
		1.67 (1.5)	5.49 (0.49)	5.28
1ES 1959+650	0.047	0.19 (12.9)	2.13 (3.24)	1.08
		1.21 (2.9)	3.6 (0.79)	3.03
BL Lacertae	0.069	0.27 (7.4)	2.44 (1.23)	1.64
		0.78 (1.3)	1.93 (0.49)	1.85

Table 8.2: 95% c.l. upper limits continued.

order as gaps in the data. Only the 8 day time scale is significantly affected. The flux from a time scale map encompassing a gap includes a correction for less exposure and accurately represents the limit for that time period. As mentioned before, the duty cycle is high at 91% and few extensive gaps in coverage exist. The reasons and date of long periods of down time are discussed in Chapter 3.

Because of the variety of changes possible in the spectrum and the strong dependence of the flux limits on a combination of power-law index, declination, and redshift, the flux limits are presented for only one assumed spectrum. Tables 8.10 and 8.13 give the factors that will convert the given limits to a different spectrum for several power-law indexes. The appropriate conversion factors for the declination and redshift of the BL Lacs can be found for the desired power-law index and applied

to the base results to find the flux limit for a different assumed spectrum.

8.1.3 Results for 1ES 1959+650

One of the TeV candidates has been detected by IACTs. In 2002 HEGRA and VERITAS detected flaring activity in 1ES 1959+650 (Aharonian et al., 2003a; Holder et al., 2003). The HEGRA collaboration has published fits to low and high state data using two forms for the energy spectrum, $dN/dE = I_0(E/TeV)^{-\alpha}$ and $dN/dE = I_0(E/TeV)^{-\alpha}e^{-E/E_c}$ (Aharonian et al., 2003a). Aharonian et al. (2003a) defines low state observations from 150 hours of data taken from 2000 to 2002 and high state observations from 6 nights (8.5 hrs) in May and July of 2002 when the integral flux above 2 TeV exceeded 1 Crab. Milagro did not detect 1ES 1959+650 during the flaring period. Table 8.14 gives the upper limits on the differential flux for the 906 day Milagro data set. The HEGRA spectral fits are used for the assumed spectrum, but these limits are not directly comparable to the HEGRA measured flux. The Milagro limits fall below the HEGRA limits because they bound the time-averaged flux for the entire data set. 1ES 1959 was not been detected by IACTS before the 2001/2002 activity and has not been reported as active more recently. The time average flux is expected to be below the HEGRA low state measurement. The HEGRA high state observations cover a 4 and 19 day period between 18 May and 18 July 2002. The limits from the time scale search are consistent with the HEGRA high state flux for time scales less than 128 days. The Milagro flux limits from the 64 day period in Table 8.14 are set for the map coinciding with the May-July 2002 flaring activity, MJD 52405-52469. It is interesting that the highest excesses observed in the 128 and 256 day searches both occur in the maps including the period of highest flaring activity.

The non-detection of 1ES 1959+650 is consistent with Milagro's sensitivity. According to the HEGRA observations, the integral flux above 2 TeV only exceeded 1 Crab for a few days. Even allowing the average flux to exceed 1 Crab for 8 days, a flux amplitude $I_0 \approx 10^{-9}\ phot/cm^2\ s\ TeV$ would be necessary for a detection.

8.2 Comparison of Flux Limits to Predicted Fluxes

8.2.1 Calculation of TeV Spectral Index

To compare Milagro observations directly to the predictions of Costamante & Ghisellini (2002), the same energy spectrum used to calculate the predicted fluxes must be used as the assumed spectrum in the flux limit calculation for Milagro data. Costamante & Ghisellini (2002) includes the broadband SED for each BL Lac and integrated fluxes above 300 GeV and 1 TeV. Before a comparison can be made, a form for the TeV energy spectrum must be chosen. The Fossati model is a parameterization using parabolic shapes for the peaks which provide no well-defined power-law index. As discussed in Chapter 2, the shape of the SSC model can approach a power law at high energies. Determining whether or not the power law can be calculated from the SSC model input parameters is, however, nontrivial.

Name	Scale	Start Time	End Time	Expos	On	Off	Excess	Excess UL	I_0
1ES 0033+595	8	2002-06-04 01:20	2002-06-12 01:20	7.9	14276	13888.2	334	597	22.2
	16	2002-06-04 01:20	2002-06-19 23:10	13.9	24672	24223.2	386	725	15.4
	32	2001-09-29 00:45	2001-10-31 00:43	31.5	70570	69797.0	665	1242	11.8
	64	2001-09-29 00:45	2001-12-02 00:48	62.3	135247	134242.3	865	1655	7.9
	128	2003-05-30 00:08	2003-09-07 14:31	93.0	164124	163119.1	865	1723	5.5
	256	2003-01-22 01:29	2003-09-07 14:31	212.2	367932	366839.7	940	2181	3.1
1ES 0120+340	8	2003-04-12 00:27	2003-04-20 01:40	7.8	33998	33560.3	401	754	14.0
	16	2003-04-04 00:37	2003-04-20 01:40	15.8	61785	61112.4	616	1098	10.1
	32	2002-01-03 00:26	2002-02-04 00:03	27.8	81742	81056.7	627	1176	6.1
	64	2001-08-28 01:45	2001-10-31 00:43	54.8	186415	185573.4	770	1589	4.3
	128	2002-09-24 21:19	2003-01-22 01:29	113.9	410491	409574.5	839	2046	2.6
	256	2002-09-24 21:19	2003-05-30 00:08	233.7	837714	836336.7	1261	2985	1.9
RGB 0136+391	8	2002-04-09 01:20	2002-04-16 21:51	7.7	32202	31731.7	428	778	14.0
	16	2002-03-08 01:36	2002-03-24 00:46	15.8	55366	54775.7	537	995	9.0
	32	2002-02-20 01:44	2002-03-24 00:46	31.0	103430	102469.1	874	1513	6.9
	64	2002-06-12 01:20	2002-08-15 01:40	59.5	204811	204039.6	702	1563	3.7
	128	2002-01-03 00:26	2002-05-11 01:07	120.5	419367	418125.3	1130	2368	2.8
	256	2002-01-03 00:26	2002-09-15 13:52	229.5	794473	793004.9	1336	3031	1.9
RGB 0214+517	8	2003-04-24 01:27	2003-05-01 23:55	7.6	25976	25546.1	381	710	17.2
	16	2003-04-20 01:40	2003-05-06 01:22	15.4	52658	51988.2	594	1068	12.8
	32	2002-12-05 01:05	2003-01-06 00:58	32.1	88029	87433.7	528	1116	6.4
	64	2003-01-22 01:29	2003-03-27 00:53	58.9	149808	149171.4	565	1323	4.2
	128	2003-01-22 01:29	2003-05-30 00:08	119.9	331726	330675.4	932	2068	3.2
	256	2002-09-24 21:19	2003-05-30 00:08	233.2	645591	644126.9	1299	2884	2.3

Table 8.3: 95% c.l. upper limits on differential flux amplitude, I_0, from each source for six time scales. The maximum excess rate is found to provide an absolute upper limit. The time scale duration is given in days. The exposure (Expos) is given in units of number of transits over Milagro (the length of a transit depends on the time spent at $\theta < 45$ for δ). The event excess over the expected background is given. The 95% c.l. upper limit on the excess is given as UL. I_0 is the differential flux amplitude obtained for the excess upper limit assuming $dN/dE = I_0(E/TeV)^{-2.5}$ in 10^{-11} $phot/cm^2$ s TeV.

Name	Scale	Start Time	End Time	Expos	On	Off	Excess	Excess UL	I_0
3C 66A	8	2002-09-24 21:19	2002-10-02 00:07	7.0	26378	25968.0	371	689	14.5
	16	2002-04-25 01:20	2002-05-11 01:07	14.0	52456	51725.1	661	1124	12.1
	32	2003-08-02 00:17	2003-09-03 01:40	31.2	107743	106756.9	892	1552	7.4
	64	2003-07-01 00:40	2003-09-03 01:40	60.7	209823	208768.1	954	1849	4.5
	128	2003-05-30 00:08	2003-09-07 14:31	93.3	328981	328115.3	783	1879	3.0
	256	2003-01-22 01:29	2003-09-07 14:31	213.4	761916	760343.9	1422	3100	2.1
1ES 0229+200	8	2002-04-17 00:34	2002-04-25 01:20	8.0	19371	19005.3	338	602	16.6
	16	2003-02-15 01:59	2003-03-02 10:59	13.0	27461	27096.6	337	647	11.0
	32	2002-03-24 00:46	2002-04-25 01:20	31.6	76795	76290.7	467	982	6.8
	64	2003-01-22 01:29	2003-03-27 00:53	59.2	121623	120935.3	636	1287	4.8
	128	2003-01-22 01:29	2003-05-30 00:08	120.7	272842	271890.4	881	1854	3.4
	256	2003-01-22 01:29	2003-09-07 14:31	214.5	476436	475167.6	1174	2461	2.5
1H 0323+022	8	2001-04-14 00:18	2001-04-22 00:14	8.0	4126	3926.9	185	306	47.1
	16	2001-05-24 06:34	2001-06-09 00:46	14.4	7657	7361.5	275	442	38.5
	32	2001-05-24 06:34	2001-06-25 00:07	30.1	17653	17230.4	393	647	26.8
	64	2001-05-24 06:34	2001-07-27 00:52	61.3	37979	37386.5	551	922	18.7
	128	2001-02-17 00:12	2001-06-25 00:07	119.6	54670	54260.2	381	812	8.5
	256	2000-12-15 22:42	2001-08-28 01:45	242.9	117447	117046.5	372	1008	5.2
1H 0414+009	8	2001-11-20 01:19	2001-11-28 01:30	7.0	4021	3845.5	163	281	59.7
	16	2002-02-04 00:03	2002-02-20 01:44	16.1	7642	7426.1	201	363	33.5
	32	2002-02-04 00:03	2002-03-08 01:36	32.2	15884	15482.3	374	614	28.3
	64	2002-02-04 00:03	2002-04-09 01:20	64.4	29993	29536.4	425	750	17.4
	128	2001-10-31 00:43	2002-03-08 01:36	123.2	63803	63261.2	504	973	11.8
	256	2001-08-28 01:45	2002-05-11 01:07	238.9	120608	120258.6	325	972	6.1

Table 8.4: 95% c.l. upper limits on differential flux from BL Lacs for six time scales continued.

Name	Scale	Start Time	End Time	Expos	On	Off	Excess	Excess UL	I_0
1ES 0647+250	8	2002-04-29 00:43	2002-05-07 00:30	7.1	21896	21563.29	333	613	15.1
	16	2000-12-15 22:42	2000-12-31 01:00	12.3	23742	23404.66	337	628	9.3
	32	2002-11-19 00:21	2002-12-21 00:44	28.6	79340	78886.66	453	979	6.3
	64	2001-04-22 01:02	2001-06-25 00:07	58.5	140543	140092.12	451	1150	3.6
	128	2002-11-19 00:21	2003-03-27 00:53	120.9	318109	317498.09	611	1666	2.5
	256	2002-09-24 21:19	2003-05-30 00:08	232.4	646637	645958.81	678	2195	1.7
1ES 0806+524	8	2002-04-21 01:49	2002-04-29 00:43	7.9	22536	22121.8	367	675	16.5
	16	2001-07-03 00:54	2001-07-19 00:16	15.2	45766	45226.3	478	912	11.7
	32	2001-06-25 00:07	2001-07-27 00:52	30.0	89162	88364.8	706	1318	8.5
	64	2001-06-25 00:07	2001-08-28 01:45	57.7	167222	166309.6	808	1629	5.5
	128	2001-06-25 00:07	2001-10-31 00:43	110.6	322657	321131.8	1351	2517	4.4
	256	2001-08-28 01:45	2002-05-11 01:07	236.3	645408	644470.2	830	2401	2.0
RGB 0812+026	8	2001-09-18 19:01	2001-09-25 00:49	5.9	4043	3909.5	124	241	45.5
	16	2001-08-04 01:47	2001-08-20 00:02	13.1	8608	8412.0	182	353	29.9
	32	2001-09-18 19:01	2001-10-15 01:37	25.2	17751	17452.7	277	525	23.2
	64	2001-06-25 00:07	2001-08-28 01:45	56.2	37911	37512.5	371	731	14.7
	128	2001-06-25 00:07	2001-10-31 00:43	108.3	73458	72866.6	550	1054	10.9
	256	2001-04-22 01:02	2002-01-03 00:26	225.7	143842	143436.7	377	1082	5.4
OJ 287	8	2001-05-04 01:41	2001-05-12 00:06	7.4	14170	13898.0	252	474	14.6
	16	2003-07-01 00:40	2003-07-17 00:27	14.7	32830	32365.1	430	773	11.7
	32	2000-12-15 22:42	2001-01-16 00:45	27.3	43870	43367.0	465	860	7.2
	64	2000-12-15 22:42	2001-02-17 00:12	58.0	88072	87126.6	875	1450	5.7
	128	2000-12-15 22:42	2001-04-22 00:14	120.0	182592	181669.5	854	1655	3.1
	256	2000-12-15 22:42	2001-08-28 01:45	236.2	435230	433962.5	1173	2405	2.3

Table 8.5: 95% c.l. upper limits on differential flux from BL Lacs for six time scales continued.

Name	Scale	Start Time	End Time	Expos	On	Off	Excess	Excess UL	I_0
1H 1013+498	8	2002-01-11 00:28	2002-01-18 17:35	7.5	20709	20179.3	473	777	17.4
	16	2002-01-03 00:26	2002-01-18 17:35	15.5	42693	42072.0	554	978	10.6
	32	2002-01-03 00:26	2002-02-04 00:03	31.3	84081	83275.2	719	1309	7.0
	64	2002-10-18 00:12	2002-12-21 00:44	53.6	161986	161305.8	607	1391	4.4
	128	2002-07-14 00:01	2002-11-19 00:21	95.7	278003	277154.1	758	1783	3.2
	256	2002-05-11 01:07	2003-01-22 01:29	212.8	623617	622208.5	1257	2801	2.2
1ES 1028+511	8	2001-11-28 01:30	2001-12-06 00:33	7.0	19378	18987.0	348	632	16.4
	16	2001-11-24 00:02	2001-12-09 10:54	13.1	36584	36078.7	449	837	11.4
	32	2001-04-06 00:37	2001-05-08 01:19	30.5	72313	71477.0	743	1303	7.5
	64	2001-03-21 01:49	2001-05-23 22:39	61.3	143320	142304.5	903	1675	4.8
	128	2002-03-08 01:36	2002-07-14 00:01	120.6	336320	335725.4	529	1659	2.4
	256	2002-01-03 00:26	2002-09-15 13:52	229.8	604197	603847.6	311	1862	1.4
RGB 1117+202	8	2001-04-30 01:36	2001-05-08 01:19	7.1	13359	13054.8	281	500	15.9
	16	2002-03-08 01:36	2002-03-24 00:46	16.1	34223	33805.5	386	733	10.1
	32	2001-08-12 00:52	2001-09-10 13:10	25.5	58047	57475.2	529	983	8.8
	64	2001-07-27 00:52	2001-09-29 00:45	48.3	111231	110598.7	585	1207	5.6
	128	2002-03-08 01:36	2002-07-14 00:01	121.3	267289	266560.3	674	1635	3.0
	256	2000-12-15 22:42	2001-08-28 01:45	235.1	434744	434074.6	620	1854	1.8
Mrk 180	8	2001-12-06 00:33	2001-12-14 01:18	6.3	7319	7056.5	208	418	56.4
	16	2003-04-20 01:40	2003-05-06 01:22	15.8	15577	15315.2	208	492	25.5
	32	2003-04-28 01:00	2003-05-30 00:08	31.1	29006	28629.8	299	691	18.3
	64	2002-04-09 01:20	2002-06-12 01:20	60.4	48394	47985.4	324	819	11.2
	128	2002-05-11 01:07	2002-09-15 13:52	107.3	78425	77920.4	401	1028	7.9
	256	2002-05-11 01:07	2003-01-22 01:29	212.2	158331	158079.3	200	1056	4.1

Table 8.6: 95% c.l. upper limits on differential flux from BL Lacs for six time scales continued.

Name	Scale	Start Time	End Time	Expos	On	Off	Excess	Excess UL	I_0
RGB 1136+676	8	2002-11-15 01:26	2002-11-23 00:21	5.0	4404	4181.7	181	340	38.7
	16	2002-11-11 00:48	2002-11-27 00:14	12.0	10438	10104.7	272	516	24.5
	32	2002-11-03 00:42	2002-12-05 01:05	22.5	19970	19485.0	396	739	19.2
	64	2001-12-02 00:48	2002-02-04 00:03	60.7	75141	74555.9	478	1086	10.2
	128	2003-01-22 01:29	2003-05-30 00:08	123.5	113916	112968.7	773	1560	7.2
	256	2002-09-24 21:19	2003-05-30 00:08	229.2	212503	211712.7	645	1643	4.1
ON 325	8	2001-04-22 01:02	2001-04-30 01:36	8.0	21420	21005.5	381	663	12.9
	16	2002-12-29 00:44	2003-01-14 01:26	14.3	48090	47607.9	443	858	9.4
	32	2002-12-21 00:44	2003-01-22 01:29	30.4	101038	100285.1	692	1298	6.7
	64	2001-12-02 00:48	2002-02-04 00:03	60.4	176147	175216.1	856	1653	4.2
	128	2001-04-22 01:02	2001-08-28 01:45	116.4	361821	360828.9	912	2040	2.7
	256	2001-04-22 01:02	2002-01-03 00:26	228.9	722728	721045.3	1546	3152	2.2
1H 1219+301	8	2002-03-24 00:46	2002-04-01 01:28	8.0	30753	30224.8	485	827	16.1
	16	2002-12-29 00:44	2003-01-14 01:26	14.4	48222	47611.3	561	985	10.8
	32	2001-11-16 01:51	2001-12-17 20:29	28.2	88647	87772.4	804	1383	7.7
	64	2003-02-23 00:13	2003-04-28 01:00	59.7	196936	195805.7	1039	1891	4.9
	128	2003-01-22 01:29	2003-05-30 00:08	122.8	422668	421057.1	1480	2727	3.4
	256	2001-04-22 01:02	2002-01-03 00:26	229.1	724477	722285.5	2014	3653	2.5
RGB 1417+257	8	2003-07-17 00:27	2003-07-25 01:35	8.2	23073	22452.7	572	877	18.2
	16	2003-07-09 00:27	2003-07-25 01:35	16.3	45253	44646.3	560	969	10.3
	32	2003-07-17 00:27	2003-08-18 00:06	31.9	87612	86930.0	629	1189	6.4
	64	2002-04-09 01:20	2002-06-12 01:20	60.1	174133	173426.4	652	1431	4.2
	128	2003-05-30 00:08	2003-09-07 14:31	94.9	266645	265820.3	761	1724	3.2
	256	2000-12-15 22:42	2001-08-28 01:45	236.2	530331	528820.2	1393	2765	2.1

Table 8.7: 95% c.l. upper limits on differential flux from BL Lacs for six time scales continued.

Name	Scale	Start Time	End Time	Expos	On	Off	Excess	Excess UL	I_0
1ES 1440+122	8	2001-01-08 01:29	2001-01-16 00:45	8.0	8034	7771.9	243	413	21.7
	16	2000-12-31 01:00	2001-01-16 00:45	14.8	14093	13775.3	295	518	15.0
	32	2003-07-17 00:27	2003-08-18 00:06	32.3	36634	36288.0	321	675	8.7
	64	2001-03-21 01:49	2001-05-23 22:39	60.0	66038	65734.9	281	758	5.3
	128	2000-12-15 22:42	2001-04-22 00:14	118.7	104660	104235.7	394	993	3.5
	256	2000-12-15 22:42	2001-08-28 01:45	237.3	259435	258888.8	507	1456	2.6
1ES 1553+113	8	2001-10-19 01:11	2001-10-27 00:42	7.6	10424	10171.5	234	425	24.9
	16	2002-01-19 01:25	2002-02-04 00:03	15.9	17518	17275.3	225	470	13.0
	32	2001-06-25 00:07	2001-07-27 00:52	30.3	40650	40316.8	309	682	10.0
	64	2001-06-25 00:07	2001-08-28 01:45	61.1	81111	80633.0	444	970	7.0
	128	2001-06-25 00:07	2001-10-31 00:43	116.4	155699	155071.0	583	1313	5.0
	256	2003-01-22 01:29	2003-09-07 14:31	216.6	231892	231966.3	-69	932	1.9
1H 1720+117	8	2001-11-04 01:28	2001-11-12 01:47	7.9	10887	10573.0	292	490	25.5
	16	2002-05-03 00:24	2002-05-19 00:55	15.9	18848	18543.3	283	538	14.0
	32	2001-06-25 00:07	2001-07-27 00:52	29.8	42560	42116.3	412	796	11.0
	64	2001-06-25 00:07	2001-08-28 01:45	60.5	84807	84188.2	575	1117	7.6
	128	2003-05-30 00:08	2003-09-07 14:31	93.6	107420	106749.2	623	1233	5.5
	256	2000-12-15 22:42	2001-08-28 01:45	238.4	260588	259453.0	1054	2009	3.5
I Zw 187	8	2003-01-18 01:26	2003-01-26 01:37	8.0	21681	21049.1	563	885	19.0
	16	2002-02-04 00:03	2002-02-20 01:44	15.1	36994	36585.6	364	744	8.4
	32	2002-05-11 01:07	2002-06-12 01:20	30.9	88429	87997.3	384	962	5.3
	64	2002-04-09 01:20	2002-06-12 01:20	61.5	181532	181165.9	326	1158	3.2
	128	2003-03-27 00:53	2003-08-02 00:17	118.8	351979	351844.6	120	1324	1.9
	256	2003-01-22 01:29	2003-09-07 14:31	214.3	607224	607486.3	-234	1455	1.2

Table 8.8: 95% c.l. upper limits on differential flux from BL Lacs for six time scales continued.

Name	Scale	Start Time	End Time	Expos	On	Off	Excess	Excess UL	I_0
1ES 1741+196	8	2002-11-15 01:26	2002-11-23 00:21	5.6	12405	12078.4	302	515	21.2
	16	2002-11-19 00:21	2002-12-05 01:05	14.2	31247	30876.4	343	673	11.0
	32	2001-11-16 01:51	2001-12-17 20:29	29.1	65118	64528.0	546	1026	8.2
	64	2002-08-15 01:40	2002-10-18 00:12	44.7	93783	93153.0	583	1155	6.0
	128	2001-04-22 01:02	2001-08-28 01:45	119.2	258032	257360.9	621	1565	3.0
	256	2000-12-15 22:42	2001-08-28 01:45	237.2	434774	433636.1	1053	2280	2.2
1ES 1959+650	8	2001-10-07 01:34	2001-10-15 01:37	8.1	14153	13800.0	294	565	32.3
	16	2003-04-20 01:40	2003-05-06 01:22	15.0	22387	21947.2	367	707	21.8
	32	2001-09-18 19:01	2001-10-15 01:37	26.3	44952	44326.7	521	1005	17.6
	64	2001-08-28 01:45	2001-10-31 00:43	55.5	92458	92095.9	302	932	7.7
	128	2002-05-11 01:07	2002-09-15 13:52	110.9	121094	120804.6	241	961	4.0
	256	2002-01-03 00:26	2002-09-15 13:52	231.3	280079	279916.6	135	1248	2.5
BL Lacertae	8	2002-11-23 00:21	2002-12-01 00:05	7.4	27807	27432.5	339	662	12.9
	16	2003-05-06 01:22	2003-05-22 00:53	15.8	65639	64990.5	587	1090	9.8
	32	2001-04-22 01:02	2001-05-23 22:39	30.1	87819	87100.1	651	1231	5.8
	64	2003-04-28 01:00	2003-07-01 00:40	57.5	224467	223276.1	1078	2010	5.1
	128	2003-01-22 01:29	2003-05-30 00:08	118.1	430311	429231.1	978	2232	2.7
	256	2003-01-22 01:29	2003-09-07 14:31	211.0	763424	762336.1	985	2652	1.8

Table 8.9: 95% c.l. upper limits on differential flux from BL Lacs for six time scales continued.

DEC	0	5	10	15	20	30	40	50	60	65	70
z=0	0.26	0.31	0.35	0.38	0.43	0.48	0.49	0.44	0.37	0.33	0.29
z=0.03	2.3	1.9	1.8	1.7	1.7	1.6	1.6	1.6	1.7	1.9	2.1
z=0.04	3.5	2.9	2.6	2.4	2.3	2.2	2.2	2.3	2.5	2.8	3.2
z=0.05	5.1	4.2	3.7	3.4	3.0	2.8	2.8	3.0	3.5	4.1	4.7
z=0.08	12.7	10.3	8.3	7.4	6.2	5.4	5.3	6.0	7.8	10.0	11.2
z=0.10	20.1	16.5	12.8	11.3	9.1	7.7	7.4	8.8	12.0	15.9	17.4
z=0.20	96.8	79.5	53.1	49.2	33.8	26.4	24.5	32.2	48.8	73.6	75.7
z=0.30	301	238	142	134	83.3	62.5	56.3	80.1	122	202	240

Table 8.10: Factors for scaling the flux upper limits calculated for $\alpha = 2.5$ and $z = 0$ to $\alpha = 2.0$ and specified redshift values. The factors are also dependent on declination. The factors are given in bins with variations less than $\sim$50% in flux over the bin.

DEC	0	5	10	15	20	30	40	50	60	65	70
z=0	0.47	0.52	0.56	0.59	0.63	0.67	0.68	0.64	0.58	0.53	0.50
z=0.03	3.0	2.5	2.3	2.1	2.0	1.9	1.9	2.0	2.2	2.4	2.8
z=0.04	4.5	3.7	3.2	2.9	2.6	2.4	2.4	2.6	3.0	3.5	4.0
z=0.05	6.2	5.1	4.3	3.9	3.4	3.1	3.0	3.3	4.0	4.9	5.6
z=0.08	13.7	11.1	8.8	7.8	6.3	5.4	5.2	6.1	8.2	10.7	11.9
z=0.10	20.6	16.8	12.8	11.4	8.8	7.3	7.0	8.5	11.9	16.2	17.4
z=0.20	85.5	69.2	45.5	42.3	28.4	22.0	20.2	27.1	41.3	63.0	66.5
z=0.30	249	191	113	106	64.8	48.2	43.2	62.3	95.2	158	198

Table 8.11: Factors for scaling flux upper limits calculated for $\alpha = 2.5$ and $z = 0$ to $\alpha = 2.2$ and specified redshift values.

DEC	0	5	10	15	20	30	40	50	60	65	70
z=0	1.8	1.7	1.5	1.5	1.4	1.3	1.3	1.4	1.5	1.6	1.7
z=0.03	5.4	4.4	3.6	3.2	2.6	2.3	2.2	2.6	3.3	4.2	4.7
z=0.04	6.9	5.5	4.4	3.9	3.2	2.7	2.6	3.1	4.1	5.3	5.9
z=0.05	8.5	6.8	5.3	4.7	3.7	3.1	2.9	3.6	4.9	6.5	7.2
z=0.08	14.2	11.3	8.3	7.5	5.5	4.4	4.1	5.2	7.6	10.7	11.7
z=0.10	18.8	14.9	10.6	9.6	6.8	5.4	5.0	6.5	9.6	13.8	15.1
z=0.20	54.9	41.2	26.0	24.2	15.2	11.4	10.3	14.5	22.5	35.1	42.3
z=0.30	135	90.0	52.9	48.8	28.5	20.7	18.2	27.3	42.4	69.0	106

Table 8.12: Factors for scaling flux upper limits calculated for $\alpha = 2.5$ and $z = 0$ to $\alpha = 2.8$ and specified redshift values.

Although this means there is some curvature in the predicted SEDs for both model types, a power-law approximation can be made using the predicted fluxes.

DEC	0	5	10	15	20	30	40	50	60	65	70
z=0	2.5	2.2	1.9	1.8	1.6	1.4	1.4	1.5	1.8	2.1	2.3
z=0.03	5.9	4.8	3.7	3.4	2.7	2.2	2.1	2.6	3.5	4.5	5.1
z=0.04	7.3	5.8	4.4	4.0	3.1	2.6	2.4	3.0	4.1	5.5	6.2
z=0.05	8.7	6.9	5.2	4.7	3.5	2.9	2.7	3.4	4.8	6.5	7.3
z=0.08	13.6	10.7	7.6	6.9	4.9	3.9	3.6	4.7	6.9	9.9	11.0
z=0.10	17.4	13.5	9.4	8.5	5.9	4.6	4.2	5.6	8.5	12.3	13.8
z=0.20	46.3	33.4	20.9	19.4	12.0	8.9	7.9	11.4	17.8	27.8	35.5
z=0.30	108	68.0	40.2	36.9	21.2	15.3	13.3	20.2	31.7	50.9	83.9

Table 8.13: Factors for scaling flux upper limits calculated for $\alpha = 2.5$ and $z = 0$ to $\alpha = 3.0$ and specified redshift values.

Flux State	α	E_c (TeV)	I_0 HEGRA	I_0 Mil 906 days	I_0 Mil 64 days
high	2.83	none	7.4±1.3±0.9	<1.1	<9.1
	1.83	4.2	5.6±0.9±0.7	<1.0	<8.9
low	3.18	none	0.78±0.15±1.0	<1.6	<12.8
	1.8	2.7	0.60±0.14±0.8	<1.7	<14.4

Table 8.14: Milagro flux limits, I_0 Mil, at the position of 1ES 1959+650 for the 906 day data set and the 64 day map coincident with 2002 flaring. The spectral shapes are from HEGRA fits to data taken during both high (> 1 $Crab$) and low (< 0.5 $Crab$) integral flux (> 2 TeV) states as defined in Aharonian et al. (2003a). The assumed spectrum is $dN/dE = I_0(E/TeV)^{-\alpha}e^{-E/Ec}$ where the photon index α, energy cutoff Ec, and measured I_0 are from Aharonian et al. (2003a). The flux amplitudes are given in 10^{-11} $phot/cm^2$ s TeV.

Solving for the power-law index that causes the differential spectrum to integrate to the predicted integral fluxes above 300 GeV and 1 TeV provides a reasonable approximation that allows a comparable flux to be calculated using Milagro data. Deviations of the power-law approximation from the fit to the SED are unimportant as long as the approximation represents the average behavior over the energies to which Milagro is sensitive. The difference between a slightly curved spectrum and a pure power law is not noticeable in the flux calculation. A break in the spectrum could cause problems, but all the TeV candidate SEDs peak below the energies accessible to Milagro. The shape of the SEDs, particularly for the Fossati model modified by Costamante, are fairly linear over a small energy range even near the peak region. For an example see the SED shown for Mrk 421 in Figure 2.6.

The SSC model SED predictions steepen sharply above a few hundred GeV. Most of the BL Lac sample are not predicted to have an appreciable flux above 1 TeV. The reason for this lies in reaching relativistic energies that require the Klein-Nishina cross section instead of the Thomson cross section as discussed in Chapter 2. Milagro is most sensitive near energies of a few TeV. This means most of the

SSC flux predictions are below flux levels detectable by Milagro. For these reasons the comparison is only made directly for SSC model predictions that extend above 1 TeV. Table 8.15 includes the spectral indexes determined for both SED fits that are used to calculate the fluxes from Milagro data for the comparison with predicted fluxes.

8.2.2 Results of Comparison with Predicted Fluxes

Once a TeV spectrum corresponding to the predicted SEDs has been determined, the flux amplitude limits can be calculated for each BL Lac. The predicted fluxes are given in integral form, but the differential flux is a better representation of Milagro observations. This is because Milagro does not have a sharp low energy cut off. Changes in the assumed spectrum cause more variation in the integral flux than the differential flux when it is quoted at the peak energy response. To make a direct comparison with the predictions, the integral fluxes from Costamante & Ghisellini (2002) are converted to the differential form using the power-law approximation already discussed. The differential flux amplitude is unfolded from the integral fluxes above 300 GeV and 1 TeV. The power-law approximation applies between those energies, which coincide with most of the energy region where Milagro has peak sensitivity. The approximation is only possible for predictions with a significant amount of flux above 1 TeV. For this reason the comparison is not made for most of the SSC model predictions. Table 8.15 lists the calculated flux limit for each predicted model spectrum and the predicted fluxes converted to differential form.

The flux limit is most affected by the declination of the source. The very high limits are for sources that transit far from zenith. Different photon indexes are a secondary effect that can be noticed in the limits for sources at similar declinations. Beyond the source parameters, the limit is then affected by the statistical significance of the observation. The most significant observation for the 906 day map is 2.2σ for RGB 1417+257. This causes a slightly higher limit than for a source not as statistically significant at the same declination and with the same spectrum. The expectation for the flux limits can be judged using Figures 8.2 and 8.3. The figures give sensitivity using the differential flux, I_0, necessary for a 3σ observation. The expectation for a source at a given redshift and declination is indicated for two spectral indexes. BL Lacs with a flux prediction near this level should be constrained or nearly constrained in this data set.

1ES 0033+595 at $\delta = 60°$ has a predicted flux of 6.03×10^{-12} $phot/cm^2$ s TeV for the modified Fossati model. The 3σ flux amplitude at $z = 0$ for $\alpha = 2.0$ is ~ 5. The predicted flux amplitude is constrained at 4.69 without IR attenuation included and is consistent with the expectation. At $z = 0.086$, $I_0 \sim 80$ for a 3σ observation. The ratio of the predicted flux to the detectable flux indicates how much additional exposure is necessary to constrain the prediction. The exposure time required to detect the predicted flux level at the 3σ level scales with the square of the flux ratio, $t_{detect} = (I_0(3\sigma)/I_{pred})^2 \times 906.2$ days. RGB 0214+517 is nearby at z=0.049 and at a more sensitive declination, $\delta = 51.7$. If the limit is redshift corrected, then $I_0 = 20.5$, which is near constraint of the modified Fossati prediction at 17.6. The 3σ flux is

Object	z	α	I_0 U.L.	I_0 U.L. with IR	Predicted I_0
1ES 0033+595$^{\star\#}$	0.086	2.16 / 2.50	4.69 / 8.82	81.2 / 79.9	6.03 / 0.649
1ES 0120+340	0.272	2.25 / –	5.11 / –	249 / –	0.81 / 0.790
RGB 0136+391	0.200	2.25 / 4.28	2.49 / 2.22	68.3 / 4.18	1.62 / 0.104
RGB 0214+517$^{\star\#}$	0.049	2.14 / 3.01	3.51 / 9.84	20.4 / 22.2	17.63 / 0.137
3C 66A	0.444	3.19 / –	9.75 / –	148 / –	0.24 / –
1ES 0229+200	0.139	2.23 / 4.62	7.54 / 6.86	167 / 10.0	2.79 / 0.174
1H 0323+022	0.147	2.25 / –	11.0 / –	743 / –	2.42 / 0.014
1H 0414+009	0.287	2.43 / –	16.9 / –	3660 / –	0.62 / 0.133
1ES 0647+250	0.200	2.29 / –	2.73 / –	77.2 / –	1.67 / 0.504
1ES 0806+524	0.138	2.31 / –	4.46 / –	84.3 / –	3.82 / –
RGB 0812+026	0.200	2.28 / –	7.77 / –	1010 / –	1.66 / 0.074
OJ 287	0.306	3.19 / –	10.7 / –	107 / –	0.73 / –
1H 1013+498	0.200	2.47 / –	5.34 / –	111 / –	0.32 / 0.336
1ES 1028+511	0.361	2.62 / –	3.99 / –	204 / –	1.05 / –
RGB 1117+202	0.139	2.15 / –	3.91 / –	104 / –	3.48 / 0.157
Mrk 180$^{\star\#}$	0.045	2.19 / –	5.56 / –	54.2 / –	24.91 / 0.050
RGB 1136+676	0.135	2.19 / –	7.19 / –	485 / –	2.70 / 0.183
ON 325	0.237	2.72 / –	9.34 / –	123 / –	0.37 / –
1H 1219+301	0.182	2.21 / –	7.17 / –	194 / –	1.96 / 0.336
RGB 1417+257	0.237	2.26 / –	8.23 / –	354 / –	1.09 / 0.455
1ES 1440+122	0.162	2.10 / 2.82	3.53 / 11.8	234 / 134	2.35 / 0.198
1ES 1553+113	0.360	2.91 / –	12.5 / –	415 / –	0.42 / 0.777
RGB 1725+118$^{\star\#}$	0.018	2.10 / 3.25	7.18 / 32.9	18.7 / 45.4	39.03 / 0.025
I Zw 187$^{\star\#}$	0.055	2.15 / –	1.59 / –	9.99 / –	15.39 / 0.145
1ES 1741+196$^{\star\#}$	0.084	2.17 / 3.80	6.47 / 15.2	73.3 / 25.9	10.61 / 0.319
1ES 1959+650$^{\dagger\star\#}$	0.047	2.17 / –	2.89 / –	25.2 / 30.1	21.99 / 0.051
BL Lacertae$^{\star\#}$	0.069	2.69 / –	6.66 / –	22.8 / 24.7	7.87 / 0.173

Table 8.15: Comparison of 95% c.l. upper limits on the differential flux with predicted fluxes from Costamante & Ghisellini (2002), which have been converted to a differential form. The assumed spectrum is $dN/dE = I_0(E/TeV)^{-\alpha}$, where I_0 is in $10^{-12}\ phot/cm^2\ s\ TeV$. The limits are given for spectral indexes determined for two fits of the SED. The first alpha is the estimated power-law index for the modified Fossati SED parameterization. The second is for the one-zone SSC model. Limits are also given with IR attenuation included using $dN/dE = I_0(E/TeV)^{-\alpha}e^{\tau(E,z)}$ where τ is calculated using IR1a.

† TeV detection by IACTs (Holder et al., 2003).

* Predicted flux constrained by Milagro limit.

$^{\#}$ Predicted flux constrained by IACT TeV limit (Costamante & Ghisellini, 2002; de la Calle Pérez et al., 2003; Horan et al., 2004).

~ 20, thus, the model can be constrained in a few months ($(20/17.6)^2 = 1.29$, 1160 days of exposure required.) The predicted 3σ I_0 can be scaled to change the desired significance level in the Gaussian regime. For example, the 5σ I_0 is approximately $(5/3)I_0$.

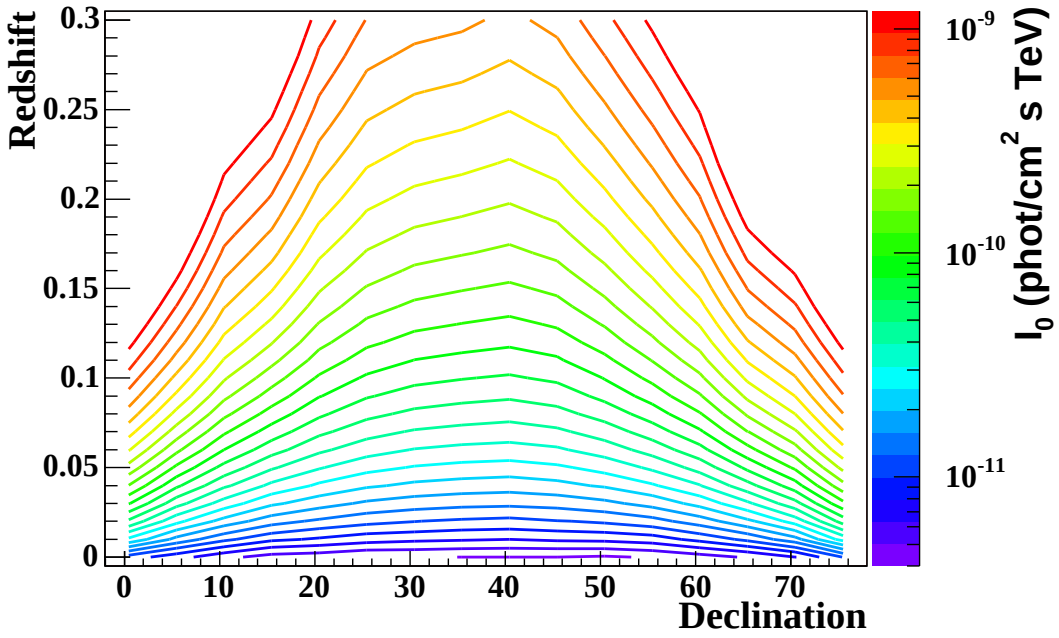

Figure 8.2: Differential flux amplitude, I_0 assuming $\alpha = 2.0$, necessary for a 3σ observation of a source at the given declination and redshift in 906 days. The redshift attenuation is obtained using IR1a.

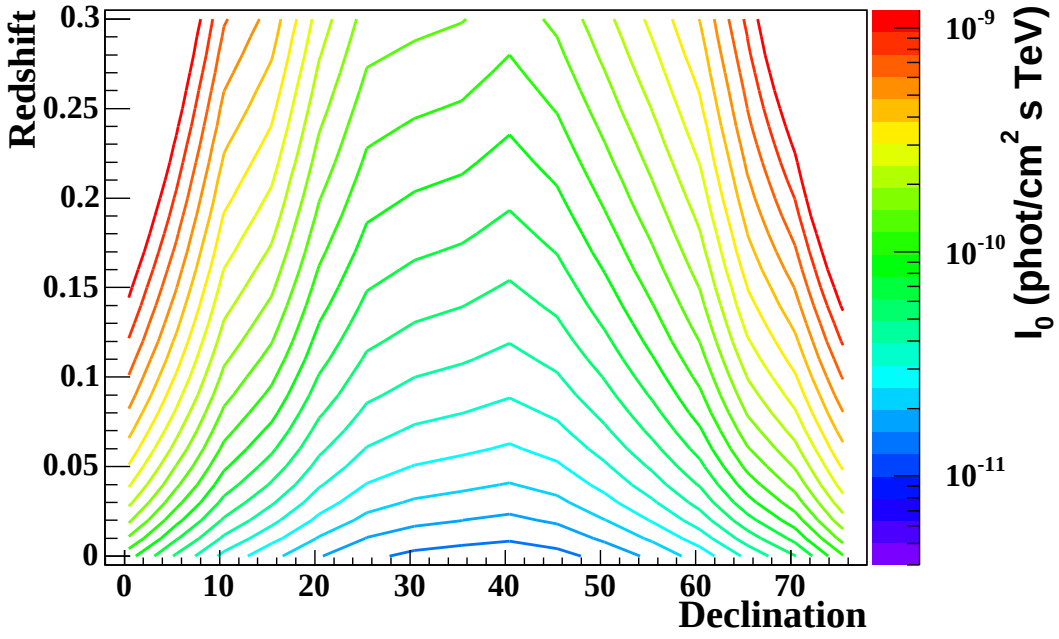

Figure 8.3: Same as Figure 8.2 with $\alpha = 3.0$

8.3 Discussion of Flux Upper Limits

None of the flux limits presented here constrain the SSC model predictions in Costamante & Ghisellini (2002). The SSC model applied is a simple one-zone homogeneous SSC model. It does not consider the effects on the SED of emission from multiple regions of the jet or from physical parameters that may vary throughout the jet. By definition, it does not include any contribution to the seed photon population for inverse-Compton scattering other than the synchrotron photons produced in the jet. Although the visibility of the high energy inverse-Compton photons requires that the density of IR photons external to the jet be low, there may be an additional contribution to the inverse-Compton emission from radiation external to the jet. It is not clear that simple SSC models accurately predict the highest energy emission from BL Lacs.

Table 8.15 notes the eight sources with Fossati style predictions that are constrained by the Milagro limits as well as those constrained by other TeV detectors. Two of the BL Lacs, 1ES 0806+524 and RGB 1117+202 are quite close to being constrained in the data set presented here and by estimation will be in another 6 months of data. None of the SSC model fluxes are at the level that can be expected to be constrained. The fluxes given are at most 0.7×10^{-12} which requires about 3.7 times the current exposure using the $\alpha = 3$ plot and ignoring IR attenuation.

The constraint of predicted fluxes can be interpreted two ways: loss due to IR attenuation of the source spectrum or an overly generous prediction by the Fossati parameterization, which is empirically based and does not include any cutoff effects at high energies. It is interesting to ask whether any of the objects are still constrained when attenuation effects are included in the spectrum. This has the effect raising the Milagro limits as described in Chapter 6 (see Figure 6.6). No changes are made to the differential flux amplitude calculated for the predicted fluxes. The differential formulation of the spectrum includes the effects of attenuation in the spectral shape only. The differential flux amplitude, I_0, remains unaltered. The predictions for I Zw 187 and RGB 1725+118 (Figures 8.4 and 8.5) are still constrained after the IR attenuation is included. The results for RGB 1725+118, however, should be considered with some skepticism because the redshift measurement is made using only one absorption line. The possible inaccuracy in the measured redshift makes the IR correction uncertain and could cause a substantial error in the calculated flux.

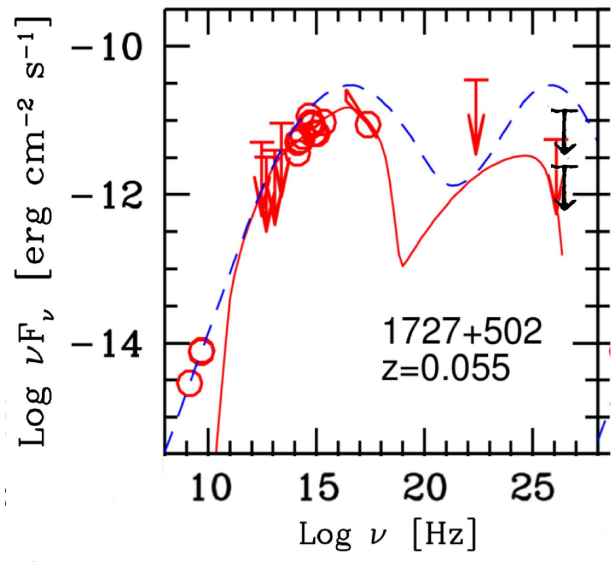

Figure 8.4: SED data and predicted SSC (solid) and Fossati (dashed) fits for I Zw 187 from Costamante & Ghisellini (2002). Upper limits in red for the second component are from Beppo Sax or IACT observations. The Milagro flux upper limits for an unabsorbed (lower) and absorbed (higher) spectrum are in black.

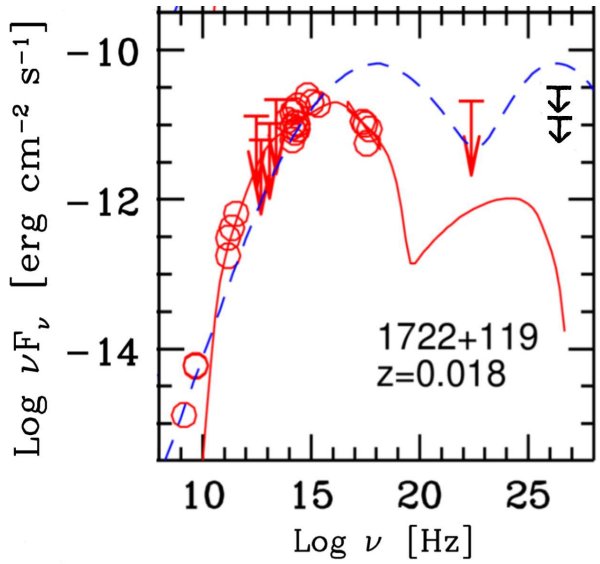

Figure 8.5: SED data and predicted SSC (solid) and Fossati (dashed) fits for RGB 1725+118 from Costamante & Ghisellini (2002). The Milagro flux upper limits for an unabsorbed (lower) and absorbed (higher) spectrum are in black.

Chapter 9

Discussion

TeV observations are well established with a source catalog of objects detected by multiple telescopes. The observational goals are beginning to shift from simple discovery to achieving more sensitive observations of the spectral and temporal characteristics that will constrain emission theories and connect to the physical state of the sources. The source catalog is still small and the classes of TeV emitters are still being found and defined. IACTs have only observed $\sim$5% of the sky in the 15 years following the first TeV detection. This coverage has been sporadic, only observing a few degrees of sky at a time. Consequently, little is known about the flaring behavior of AGN or about the types of additional transient sources that may exist at TeV energies.

This work takes two approaches to the search for TeV gamma-ray emitters by taking advantage of the wide field-of-view and daily observations available using the Milagro observatory. Searches covering the entire field-of-view as well as those directed at specific sources have been conducted. A real-time search of Milagro data continuously monitors the overhead sky for signals; thus, no assumptions about the types of objects that produce TeV emission are necessary. Searching a range of durations from 2 hours to 2 years removes any bias to a single time scale or prediction for transient behavior based on information in other wavebands. No additional significant signals were found for time periods from 8 days to 2 years that include detections of the Crab Nebula and Mrk 421.

The absence of detections prompts a closer examination of a few specific sources. X-ray selected BL Lacs have been studied because of their predicted level of emission at very high energies and the predominance of this source class in the current TeV catalog. The selected sample has fits of the SED with TeV flux predictions allowing some additional comment to be made on the objects in the absence of a detection. Although other observations have been made of some of the same objects, the time overlap is small. The combination of IACT observations with the observations presented here covers almost 10 years for some of the sample. Some sources with larger redshifts or at large zenith angles have been excluded, however, from any IACT observations, but are naturally included in the Milagro results.

The time integrations available from this study set a slightly different limit on flaring behavior than those from IACT observations. Though the sensitivity of Milagro to these sources requires more than the few hours of exposure typical for IACTs,

the longer exposures are readily available and bring the flux limits set by Milagro for the longer time scales into a comparable range with the IACT results. The IACT limits address the quiescent levels from these BL Lacs while the Milagro limits put a constraint on the time-averaged flux over the full period that they were observed.

Neither the IACT limits nor those presented here put any constraint on the SSC model predictions examined. The levels of emission for the multiwavelength data used for the fits probably best represents quiescent levels. In a flaring state, simultaneous observations in X-ray in particular may produce a different looking SED. The absence of constraints is not unexpected given the low fluxes predicted. The SSC model generally predicts less emission at very high energies than other leptonic models. It is not likely to be a completely accurate description without modifications that include additional target photon populations. The Fossati parametrization is observationally and not physically founded but has approximated the SEDs of the detected TeV emitters reasonably well. Constraints of the SED fits are consistent with a steepening of the very high energy portion of the SED due to the physical process in the jet and the absorption of photons on the EBL.

The observations by Milagro of this set of BL Lacs are the most complete available in the last 3 years. Some of the sources have no previous TeV limits because they are predicted to be too far away or too faint to merit observations by IACTs. Many of the BL Lacs in this sample have been observed by other TeV instruments but none with the exposure available using Milagro. The limits set by IACTs provide in some cases a more sensitive limit on the quiescent emission, but only the Milagro observations offer hard limits on the time-integrated flaring emission over the 2.7 year period and shorter time scales within that period. The flaring behavior of Mrk 421 is considered to be quite rare and these observations appear to confirm that. If any of these objects had flared with an average flux level twice that of the Crab Nebula, it would be detectable in $\sim$ 1.3 years (less at declinations closer to zenith). At the level of five times the Crab flux, a source would be detected in 10 months. Mrk 421 has been detected at $4\sigma/\sqrt{month}$ which implies a similar source would achieve a 5σ detection in $<$50 days. At the brightest Mrk 421 reached 4σ in $\sim$1 week implying a similar source could be detected in eleven days.

It is encouraging that campaigns focused on HBLs have led to several detections in TeV instruments. Despite the lack of additional detections in the observations presented here, the candidate objects still supply a favorable selection for future searches. Flaring activity in BL Lacs has been observed to appear and then disappear entirely over the years of observation by IACTs. A lack of detection in the 2.7 years of data examined in this work does not limit the emission possible from future activity. It does emphasize, however, the importance of long-term monitoring of BL Lacs. The infrequency of flaring episodes and the possibilities of extremely short duration flaring make a high frequency of observations desirable. To study the variation of the spectrum in detail, nearly continuous monitoring is necessary. This kind of comprehensive survey when conducted by a more sensitive large field-of-view instrument can provide the observations necessary to begin to model the temporal characteristics of BL Lac emission in addition to constraining the emission mechanism.

The exposure available to wide field-of-view instruments makes them a key component to the future development of TeV astronomy. As the TeV catalog grows, it will become increasingly wasteful to spend the limited time of IACTs on monitoring transients. Techniques that cover large fields and are sensitive to short-term behavior can be used to indicate where and when the high sensitivity narrow-field instruments are best applied. They may also be the only viable method of detecting the very short-term behavior of gamma-ray bursts.

TeV astronomy is the study of the extremes of already extreme objects. Active galaxies form a very small percentage of observed galaxies, and the blazars visible at very high energies form a smaller subset of those. As shown in this work, there has been nothing in the Northern Hemisphere as bright at TeV energies as Mrk 421 in the past two years. Despite the rarity of this behavior, the extremes of an object like Mrk 421 offer a wealth of information. The TeV observations alone constrain the size of the emission region and the bulk Lorentz factor of the jet. The combination of TeV observations with other wavebands, optical and X-ray in particular, constrain the emitting particle types and densities as well as the magnetic fields. Future measurements from even a few more sources will make a dramatic difference in our understanding of the underlying physical processes.

An important element of understanding the most unique behavior of TeV blazars may involve making the connection to the more "typical" extreme objects. It is not enough to simply define the differences. They must be understood within the broader population of active galaxies. The goal in the end is not a catalog collection of obscure galaxies but a fundamental understanding of why they are unique and of how those qualities relate to the physical environments near super-massive black holes, the formation of galaxies, and the development of the universe.

Appendix A

Timing Calibration Correction Details

A.1 Laser Ball Positions

The positions of the laser balls were surveyed in the same coordinates used for the pond PMTs. The coordinates are measured relative to a central point in the detecter. The survey positions of the PMTs and laser balls are inputs in the fit for time offsets discussed in Chapter 4. The original survey is presented in Table A.1.

Several of the laser balls have become detached from their grid positions and been attached again during repair operations. In the November 2001 laser calibration data the change in a laser ball position is noticeable enough to require a correction before the time offsets can be calculated. No other obvious deviations in position have been noticed in the calibration data. It may be that all the laser balls were firmly affixed during previous calibrations. The 2002 and 2003 repairs included checking laser ball positions to insure that they were all firmly attached for the following calibration. The adjusted laser ball survey used for the November 2001 calibration is given in Table A.2. Laser ball 18 is given a new position in this survey determined by a minimization of calculated fiber length differences in the data.

A.2 TStart Corrections

Tables A.3 and A.4 list the corrections made to the recorded TStart times for each calibration run. The correction value is subtracted from TStart values for the indicated laser ball during the specified time period. After applying the correction, the slewing and time offset corrections are fit. In some cases, the times could not be corrected and are excluded from the calibration analysis. When an end time is not specified the correction is made for all subsequent data from the indicated laser ball.

Laser Ball	X	Y	Z	Laser Ball	X	Y	Z
1	3524.4	-1973.1	668.4	16	1497.1	1152.8	667.4
2	1397.5	-3079.8	665.4	17	462.9	684.7	669.4
3	-828.6	-3946.7	667.4	18	-1025.0	658.0	669.4
4	2781.1	-1680.0	669.4	19	-1856.1	-362.8	666.4
5	1753.4	-2149.6	669.4	20	1036.6	2185.9	668.4
6	466.5	-2736.4	669.4	21	-2.5	1716.9	669.4
7	-571.6	-3196.5	667.4	22	-1291.1	1135.6	669.4
8	2315.7	-648.6	669.4	23	-2325.2	667.3	669.4
9	1280.0	-1115.2	667.4	24	577.8	3218.3	667.4
10	-9.8	-1696.9	667.4	25	-462.1	2751.7	669.4
11	-1042.1	-2167.4	669.4	26	-1748.8	2169.4	667.4
12	1849.4	379.8	665.4	27	-2785.8	1700.8	666.4
13	813.5	-86.4	669.4	28	849.1	3962.5	665.4
14	-475.5	-667.6	665.4	29	-1494.1	3061.5	665.4
15	-1508.4	-1137.2	669.4	30	-3527.4	1989.1	667.4

Table A.1: Survey positions of laser balls in the coordinate system of pond PMTs.

Laser Ball	X	Y	Z	Laser Ball	X	Y	Z
1	3524.4	-1973.1	668.4	16	1497.1	1152.8	667.4
2	1397.5	-3079.8	665.4	17	462.9	684.7	669.4
3	-828.6	-3946.7	667.4	18	-1091.8	591.2	602.6
4	2781.1	-1680.0	669.4	19	-1856.1	-362.8	666.4
5	1753.4	-2149.6	669.4	20	1036.6	2185.9	668.4
6	466.5	-2736.4	669.4	21	-2.5	1716.9	669.4
7	-571.6	-3196.5	667.4	22	-1291.1	1135.6	669.4
8	2315.7	-648.6	669.4	23	-2325.2	667.3	669.4
9	1280.0	-1115.2	667.4	24	577.8	3218.3	667.4
10	-9.8	-1696.9	667.4	25	-462.1	2751.7	669.4
11	-1042.1	-2167.4	669.4	26	-1748.8	2169.4	667.4
12	1849.4	379.8	665.4	27	-2785.8	1700.8	666.4
13	813.5	-86.4	669.4	28	849.1	3962.5	665.4
14	-475.5	-667.6	665.4	29	-1494.1	3061.5	665.4
15	-1508.4	-1137.2	669.4	30	-3527.4	1989.1	667.4

Table A.2: Survey positions of laser balls for data taken in November 2001 in the coordinate system of pond PMTs.

Laser Ball	Start		Stop		Correction
	TJD	UT (s)	TJD	UT (s)	(counts)
2	2241	72900	2241	73390	10
10	2227	76210.40	-	-	8
24	2242	77100	2242	77310	-8
27	2243	9190	2243	9290	exclude

Table A.3: TStart corrections to be applied to laser data taken in November 2001. TJD is defined here as MJD - 60,000.

Laser Ball	Start		Stop		Correction
	TJD	UT (s)	TJD	UT (s)	(counts)
6	1876	76530	1876	80945	-10
7	1877	67550	1877	68677	+6
7	1877	68636.5	1877	68677	exclude
11	1882	84600	1883	1487.24	-8

Table A.4: TStart corrections to be applied to laser data taken in November 2000.

Bibliography

Aharonian, F., et al. 2002a, A&A, 393, L37

—. 2002b, A&A, 393, 89

—. 2003a, A&A, 406, L9

—. 2003b, A&A, 403, 523

Aharonian, F. A. 2000, New Astronomy, 5, 377

Aharonian, F. A., et al. 1999, A&A, 349, 11

—. 2000a, A&A, 353, 847

—. 2000b, ApJ, 539, 317

Alexandreas, D., et al. 1993, NIM, A328, 570

Alexandreas, D. E., et al. 1992, NIM, A311, 350

Atkins, R., et al. 2000a, ApJ, 533, L119

—. 2000b, NIM, A449, 478

—. 2003, ApJ, 595, 803

—. 2004a, ApJ, 604, L25

—. 2004b, In Press astro-ph/0403097

Benbow, W. 2002, PhD thesis, University of California, Santa Cruz

Biller, S., et al. 1994, ApJ, 423, 714

Blaufuss, E., Noyes, D., Hays, E., McEnery, J., Smith, A. J., & Sullivan, G. 2002, Milagro Collaboration Internal Memo

Borione, A., et al. 1994, NIM, A346, 329

Buckley, J. 2001, in Proc. Gamma 2001, Baltimore, MD, 9999

Bullock, J. S. 1999, Ph.D. Thesis

Cesarsky, C. J., & Montmerle, T. 1983, Space Science Reviews, 36, 173

Chadwick, P. M., Lyons, K., McComb, T. J. L., Orford, K. J., Osborne, J. L., Rayner, S. M., Shaw, S. E., & Turver, K. E. 1999, ApJ, 521, 547

Chen, A., Reyes, L. C., & Ritz, S. 2004, ApJ, in press astro-ph/0402152

Costamante, L., & Ghisellini, G. 2002, A&A, 384, 56

Coyne, D., & Schneider, M. 2002, Milagro Collaboration Internal Memo

de Jager, O. C., & Stecker, F. W. 2002, ApJ, 566, 738

de la Calle Pérez, I., et al. 2003, ApJ, 599, 909

Dermer, C. D., Schlickeiser, R., & Mastichiadis, A. 1992, A&A, 256, L27

DeYoung, T. 2003, Milagro Collaboration Internal Memo

Fleysher, L. 2003, PhD thesis, New York University

Fleysher, L., Fleysher, R., & Nemethy, P. 1997a, Milagro Collaboration Internal Memo

Fleysher, L., Fleysher, R., Nemethy, P., & Leonor, I. 1997b, Milagro Collaboration Internal Memo

Fossati, G., Maraschi, L., Celotti, A., Comastri, A., & Ghisellini, G. 1998, MNRAS, 299, 433

Gaidos, J. A., et al. 1996, Nature, 383, 319

Ghisellini, G., & Madau, P. 1996, MNRAS, 280, 67

Ghisellini, G., Maraschi, L., & Dondi, L. 1996, A&A Supplement, 120, C503

Ghisellini, G., Padovani, P., Celotti, A., & Maraschi, L. 1993, ApJ, 407, 65

Gould, R. J., & Schréder, G. P. 1967, Physical Review, 155, 1408

Harding, A. K., & Zhang, B. 2001, ApJ, 548, L37

Hartman, R. C., et al. 1999, ApJs, 123, 79

Helene, O. 1983, NIM, 212, 319

Hillas, A. M., et al. 1998, ApJ, 503, 744

Holder, J., et al. 2003, ApJ, 583, L9

Horan, D., & Weekes, T. C. 2004, New Astronomy Review, 48, 527

Horan, D., et al. 2002, ApJ, 571, 753

—. 2004, ApJ, 603, 51

Jannuzi, B. T., Smith, P. S., & Elston, R. 1994, ApJ, 428, 130

Kerrick, A. D., et al. 1995, ApJ, 452, 588

Klebesadel, R. W., Strong, I. B., & Olson, R. A. 1973, ApJ, 182, L85

Konopelko, A., Mastichiadis, A., Kirk, J., de Jager, O. C., & Stecker, F. W. 2003, ApJ, 597, 851

Krawczynski, H., et al. 2004, ApJ, 601, 151

Krennrich, F., et al. 1999, ApJ, 511, 149

—. 2001, ApJ, 560, L45

Laurent-Muehleisen, S. A., Kollgaard, R. I., Feigelson, E. D., Brinkmann, W., & Siebert, J. 1999, ApJ, 525, 127

Li, T. P., & Ma, Y. Q. 1983, ApJ, 272, 317

Mücke, A., & Protheroe, R. J. 2001, Astroparticle Physics, 15, 121

Malkan, M. A., & Stecker, F. W. 2001, ApJ, 555, 641

Mannheim, K. 1993, A&A, 269, 67

Maraschi, L., Ghisellini, G., & Celotti, A. 1992, ApJ, 397, L5

Marscher, A. P., & Gear, W. K. 1985, ApJ, 298, 114

Morales, M. 2002, PhD thesis, University of California, Santa Cruz

Padovani, P., & Giommi, P. 1995, ApJ, 444, 567

Petry, D., et al. 2002, ApJ, 580, 104

Primack, J. R., Bullock, J. S., Somerville, R. S., & MacMinn, D. 1999, Astroparticle Physics, 11, 93

Punch, M., et al. 1992, Nature, 358, 477

Quinn, J., et al. 1996, ApJ, 456, L83

Rebillot, et al. 2003, in Proc. 28th Annual Cosmic Ray Conference, Tsukuba, Japan, 2599

Roberts, M. D., et al. 1998, A&A, 337, 25

—. 1999, A&A, 343, 691

Samuelson, F. W., et al. 1998, ApJ, 501, L17

Sikora, M., Begelman, M. C., & Rees, M. J. 1994, ApJ, 421, 153

Smith, A. J., et al. 2001, 27th ICRC

Stecker, F. W. 1999, Astroparticle Physics, 11, 83

Sullivan, G. 2001, in 27th International Cosmic Ray Conference, Hamburg, Germany

Sullivan, G., & Smith, A. J. 2000, Milagro Collaboration Internal Memo

Swanenburg, B. N., et al. 1981, ApJ, 243, L69

Tavecchio, F., Maraschi, L., & Ghisellini, G. 1998, ApJ, 509, 608

Urry, C. M., & Padovani, P. 1995, Publications of the Astronomical Society of the Pacific, 107, 803

Vassiliev, V. V. 2000, Astroparticle Physics, 12, 217

Weekes, T. C., et al. 1989, ApJ, 342, 379